A FINITE ELEMENT MODEL FOR POROVISCOELASTIC HYDRODYNAMIC LUBRICATION

A Dissertation
Presented to
The Academic Faculty

by

Patrick A. Smyth

In Partial Fulfillment
of the Requirements for the Degree
Doctor of Philosophy in the
Woodruff School of Mechanical Engineering

Georgia Institute of Technology
May 2017

A FINITE ELEMENT MODEL FOR POROVISCOELASTIC HYDRODYNAMIC LUBRICATION

Approved by:

Dr. Itzhak Green, Advisor
Woodruff School of Mechanical
Engineering
Georgia Institute of Technology

Dr. Scott Bair
Woodruff School of Mechanical
Engineering
Georgia Institute of Technology

Dr. Robert L. Jackson
Department of Mechanical
Engineering
Auburn University

Dr. Jeffrey Streator
Woodruff School of Mechanical
Engineering
Georgia Institute of Technology

Dr. Michael Varenberg
Woodruff School of Mechanical
Engineering
Georgia Institute of Technology

Date Approved: January 13th 2017

ACKNOWLEDGEMENTS

I would like to acknowledge the support and guidance of Dr. Itzhak Green, who has served as a mentor to me during my time at Georgia Tech. His guidance and knowledge is exceptional, and I am thankful to have had the opportunity to pick his brain for five years. Dr. Green has always been available and willing to help, and I certainly appreciate his methods of managing graduate students.

I would also like to thank my reading committee: Dr. Scott Bair, Dr. Robert Jackson, Dr. Jeffery Streator, and Dr. Michael Varenberg for taking the time to serve on my committee. Dr. Jackson deserves special recognition for plucking me from the classrooms of Auburn University and developing my skills as a researcher and engineer. I certainly owe a great deal to him, and would not have followed the path I did without his guidance.

I have met many great friends during this phase of my life. I want to thank Phil Varney, Matthew Perrella, Peter Yeh, and Eric Smith for their academic and non-academic friendship. If you judge a man by the company he keeps, I am doing pretty well for myself.

Finally, I would like to thank my family for their love and support. My parents taught me the value of hard work and education. They made many sacrifices for my brother and me, and I cannot thank them enough. I want to thank my brother for always setting the bar high and giving me something to shoot for. His academic curiosity is unrivaled. My wife, Leigh Anna, deserves the final acknowledgment. Simply put, she is the reason these long days and long nights have been worth it.

TABLE OF CONTENTS

LIST OF TABLES

LIST OF FIGURES

NOMENCLATURE

a	Film inlet to outlet ratio (h_i/h_o).
A	Porous area in contact (solid and fluid).
A_j	Grűnwald-Letnikov coefficient.
$B(\omega)$	Dynamic damping.
$C(t)$	Compliance modulus.
$d(t)$	Bearing displacement.
$D(t)$	Displacement.
E	Elastic modulus.
$E(t)$	Viscoelastic relaxation modulus.
$\dot{E}(t)$	Time derivative of relaxation modulus.
E_∞	Rubbery (equilibrium) modulus.
E_n	Viscoelastic spring term.
$E'(\omega)$	Storage modulus.
$E''(\omega)$	Loss modulus.
$E^*(\omega)$	Complex modulus.
$E_\alpha(t)$	Mittag-Leffler function.
$erfc$	Complementary error function.
$F(t)$	Force.
F_i	Force in individual soil grain.
$\mathcal{F}$	Fourier domain.
G_{ij}	Shear modulus.
g_i	Viscoelastic constant used by ABAQUS.
H	Porous pad height.
H'	Biot poroelastic constant.
h	Fluid film thickness.

h_i	Inlet fluid film thickness.
h_o	Outlet fluid film thickness.
H_1	Effective film thickness.
i	Imaginary unit.
$J(t)$	Viscoelastic creep modulus.
$\dot{J}(t)$	Time derivative of creep modulus.
$K(t)$	Stiffness modulus.
$K'(\omega)$	Storage modulus.
$K''(\omega)$	Loss modulus.
$K^*(\omega)$	Complex modulus.
K_{ij}	Bulk modulus.
k	Permeability.
K	Hydraulic conductivity.
k_i	Viscoelastic constant used by ABAQUS.
$\mathcal{L}$	Laplace domain.
L	PVE pad length.
M	Biot poroelastic constant.
p	Pore pressure.
P	Fluid film pressure.
P_m	Mean fluid film pressure.
R'	Biot poroelastic constant.
s	Laplace variable.
S	Distributed load of the solid grains.
S_σ	Sum weighted history of stress.
S_ϵ	Sum weighted history of strain.
t	Time.
Δt	Time increment.

u, v, w	Fluid velocity in x,y,z-directions, respectfully.
u', v', w'	Filter velocity in x,y,z-directions, respectfully.
U_1	Bearing velocity in x-direction.
U_x	Filter velocity in x-direction.
V_1	Bearing velocity in y-direction.
V_y	Filter velocity in y-direction.
W	Bearing load.
ΔW	Incremental change to bearing load.

Greek symbols.

α	Fractional derivative constant.
α_B	Beavers-Joseph slip coefficient.
α_{Biot}	Biot poroelastic constant.
β_n	Complementary error function model material constant.
δ_{ij}	Kronecker delta.
Δ	PVE pad deformation.
$\epsilon(t)$	Strain.
η	Viscoelastic time constant.
$\dot{\epsilon}(t)$	Time derivative of strain.
γ_n	Ratio of moduli in viscoelastic model.
Γ	Gamma function.
λ_n	Prony viscoelastic constant.
μ	Lubricant viscosity.
μ_n	Complementary error function model material constant.
ν	Poisson's ratio.
ρ	Fluid density.

$\sigma(t)$	Stress.
$\sigma_{VE}(t)$	Viscoelastic stress in solid grains.
$\sigma'(t)$	Effective stress.
ω	Frequency (rad/s).
τ	Viscoelastic time constant.
ξ	Porous film thickness modifier.
ζ	Poroelastic fluid strain.

SUMMARY

Triboelements are ubiquitous in modern society. They exist in countless applications from locomotion (both human and mechanical) to magnetic recording. Billions of dollars are lost from tribological inefficiencies per year, and at the same time, the state-of-the-art is pushing triboelements toward greater capabilities such as load support and longevity. A potential advancement comes from including a poroviscoelastic material in triboelements. It is hypothesized that poroviscoelasticity can improve triboelement dynamic properties such as loss and wear resistance without sacrificing significant load support. A poroviscoelastic material has multiple features that make it interesting for study: porous structure for lubricant storage, a built-in dissipation mechanism, and adaptive storage and loss characteristics. The current poroviscoelastic models are traditionally based on a Zener-type material structure; however, a novel model for viscoelasticity will be introduced. This model is based on fractional calculus that simplifies the description of viscoelasticity while retaining model robustness. The fractional calculus poroviscoelastic model will be implemented in ABAQUS, a commercially available finite element analysis (FEA) software. ABAQUS allows for external interfacing, and broad application, of the poroviscoelastic model. These applications are numerous and include: mechanical seals, biomechanical joint replacements, flexible rotordynamic bearings, and biomimetic dampers, among others. To establish the aforementioned principles, the proposed constitutive material model will be coupled with a hydrodynamic bearing. This work will serve as the theoretical foundation for the study of poroviscoelastic hydrodynamic lubrication and its applications.

CHAPTER I

INTRODUCTION

As the state-of-the-art pushes triboelements toward greater capabilities and longevity, the need for evolving triboelement technology exists. The following work explores a novel coupling of phenomena inspired by biomimetics. A poroviscoelastic substrate, coupled to a fluid film load is modeled and compared to its rigid counterpart. It is hypothesized that poroviscoelasticity can improve triboelement properties such as damping and wear resistance, and have utility in certain applications where flexibility is desired (e.g. biomechanical joint replacements, flexible rotordynamic bearings, and mechanical seals). This study provides the framework for the analysis of flexible, porous viscoelastic materials and hydrodynamic lubrication.

Biomimetics is emerging as an avenue for new tribological technology. A material of particular interest is articular cartilage. This load bearing material is a phenomenal facilitator of motion and has low friction and high wear resistance [1,2]. Cartilage is a flexible, porous collagen (solid) matrix permeated with synovial fluid. It is desired to mimic this mechanism for application in mechanical systems.

Porous bearings are already commonplace in engineering applications. These sintered, or self-lubricating, bearings consist of a metal matrix impregnated with a lubricant. The interface of the journal and the bearing surface is virtually rigid, and the bearings operate in the mixed lubrication regime. However, if the bearing surface is made compliant, then deformation occurs in the bearing substrate, potentially leading to operation in the full film regime. The mechanism by which deformation occurs can be modeled in a number of ways (e.g. elastic, viscoelastic, elastic-plastic, etc.). Poroviscoelasticity (PVE) is one such constitutive model for a flexible, porous

material. Certain engineered materials, like polyurethane foams and hydrogel scaffolds, display poroviscoelastic character. It is desired to explore PVE materials in applications such as bearings and dampers.

The objective of the current work is to couple a fully saturated poroviscoelastic bearing material with a hydrodynamic (HDL) fluid load. The fluid mechanics of thin-films are well-defined for conventional, rigid, triboelements by the Reynolds equation. However, the traditional Reynolds equation assumes no-slip conditions occurring between rigid plates. With a porous and flexible interface, the boundary conditions of the Reynolds equation are modified to allow vertical flow in and out of the substrate material, as well as effective slip in the horizontal direction. The implications of the coupled HDL/PVE problem are studied as they relate to triboelement performance.

Poroviscoelastic materials have two time-dependent mechanisms, giving rich frequency domain characteristics (i.e stiffness and damping). The properties of stiffness and damping are assessed relative to an steady-state. This work is fundamental to understanding the transient behavior of a coupled HDL/PVE triboelement.

1.1 Applications for Research

There are health, infrastructure, and industrial applications for the proposed research. One such application is artificial joint technology, where an estimated 27 million people suffer from osteoarthritis in the United States alone [3]. The estimated cost of this disease is $128 billion annually [4]. Another example is in infrastructure protection, where poroviscoelastic bearings and dampers could be used to mitigate fatigue or one-off events (e.g. seismic activity). Such elements could be introduced retroactively in existing designs to improve longevity [5]. Other research targets include rotordynamic system property modification. These concepts are discussed in the following sections.

1.1.1 Biomechanics

The genesis for the current work comes from the study of articular cartilage. In previous research, it is shown that articular cartilage displays viscoelastic behavior [1, 2]. This behavior is only phenomenological; however, the viscoelastic models undeniably capture cartilage behavior in stress-relaxation. To separate the solid and fluid phases of a biphasic material like cartilage, an additional mechanism is required. Poroviscoelasticity allows for that mechanism, and is often used in cartilage modeling [6, 7]. Cartilage mechanics is an active area of research in the biomechanics community. In part, this is due to the prevalence of osteoarthritis and a need for better mitigation or joint replacement technologies. Patients suffering the minor effects of osteoarthritis experience discomfort when moving, and those suffering severe cases often require joint replacement or invasive surgery. Unfortunately, joint replacements are prohibitively expensive for many, and require significant recovery and rehabilitation periods. The poroviscoelastic model has the potential to serve as a robust, but succinct, model for evaluating healthy or damaged cartilage.

1.1.2 Biomimetic Dampers

The flexible, biphasic mechanism of cartilage could be introduced in biomimetic applications. Poroviscoelastic materials could have application in dampers for bridges and structures, where conventional bearings are subject to loadings that cause surface contact and wear. In particular, transportation bridge failure [8] is a particular area of interest for biomimetic dampers, which includes both impulse and vibration dampers. Transportation alone is an over 400 billion dollar annual expense in the US [9], and mitigation strategies have the potential to prevent some failures in infrastructure.

The proposed modeling approach allows for poroviscoelasticity to be included in large-scale system modeling. This gives structural designers a more accurate assessment of the value of biomimetic dampers. The fractional calculus poroviscoelastic

model simplifies certain modeling aspects of such an analysis. The use of fractional calculus maintains modeling robustness, and viscoelastic behavior is captured over many frequency decades. Therefore, many practical applications for biomimetic materials can be explored.

1.1.3 Flexible Bearing Supports

The performance of many vibratory and rotordynamic components can be improved by modifying the system's stiffness and damping characteristics [2, 10–12]. This is often done with tuned materials. Poroviscoelasticity is a probable material option for such dynamic systems, as the stiffness and damping properties are frequency dependent. This is in contrast to traditional dynamic systems, where the stiffness and damping coefficients are invariant. Poroviscoelasticity allows for tuning of the stiffness and damping characteristics of rotordynamic systems. Such material tuning could prevent failure of rotating systems as they operate at, or pass through, critical speeds. The traditional application point for such a material is in the supporting bearings [2, 13], where porovisoelasticity could be introduced. This may prevent catastrophic and fatigue failures.

1.1.4 Fluid Loaded Soils

One of the dominant reasons for developing poroelastic and then poroviscoelastic theory is for soil mechanics [14–17]. The current work considers fluid loads on poroviscoelastic materials. This is analogous to a saturated soil under a lake, or a reservoir contained by a dam. Also, the current work can be modified to determine the impingement of drilling fluid into porous soil during drilling operations, or to study the impact of resource extraction from a reservoir. Such work is of particular importance in the current regulatory environment [18–20].

1.2 Problem Statement

The proposed work simulates the coupled interactions of two complex systems, namely a poroviscoelastic material and a hydrodynamically lubricated bearing. ABAQUS, a commercially available finite element software, is used as a platform to model a poroviscoelastic material that interfaces with a hydrodynamically lubricated (HDL) bearing. The poroviscoelastic and HDL components are coupled; therefore, each component influences the behavior of the other component. The system's total response is likewise dependent on each component and their interactions. The coupled system is iteratively simulated to access performance.

A novel model for porovisoelasticity is given herein, based on fractional calculus. This model is reduced to a specific case when the fractional derivative is equal to $1/2$. The reduced model is known as the complementary error function fractional model, or CERF. Numerical techniques to simulate CERF viscoelasticity are discussed in relation to FEA software packages.

A porous, hydrodynamic lubrication model is developed that allows for fluid flow at the permeable boundary. This is based on the Beavers-Joseph slip condition. The HDL problem is simulated using a finite difference/finite volume approach, and it interacts with ABAQUS as a time-dependent loading condition. This model will be developed in Fortran and Python to comply with ABAQUS. Guidelines for the numeric routines will be available for analysis of the aforementioned applications, and others that share similar characteristics.

1.3 Scope

The scope of this work is to provide an analysis tool for coupled poroviscoelasticity and HDL problems. The physics of each component of the system are derived in general terms such that broad applicability is possible; however, the goal of the proposed work is not to explore every application discussed. Rather, the work provides a

toolbox so that the aforementioned applications, and others, can be studied. A thrust bearing with a poroviscoelastic pad will be simulated to validate the approach, while the framework for more complicated bearings and mechanical seals is established. In addition, skeleton code listings are provided for use in additional studies and applications.

The specific goals of this work are: 1) to develop a fractional calculus representation of poroviscoelasticity, 2) to develop a numerical scheme that can simulate fractional calculus viscoelasticity in the time domain, 3) to determine the feasibility of a poroviscoelastic material as a bearing substrate in a hydrodynamic lubrication application, and 4) to develop a set of analysis tools to evaluate the coupled poroviscoelastic/hydrodynamic lubrication system.

The proposed work is novel in three major areas: 1) the use of fractional calculus in poroviscoelasticity, 2) the development of a reduced fractional model by use of the CERF, and 3) the coupling of poroviscoelasticity with a rotating triboelement (through HDL). The coupled system has a diverse range of applications that correspond to the current state-of-the-art research. The proposed work addresses concepts such as numerical approximation of fractional derivatives and coupling disparate phenomena. The goal is to develop a robust model that can be applied to a large number of engineering problems. Such a tool is proposed to advance the understanding of complex material and triboelement interactions.

CHAPTER II

LITERATURE SURVEY

The following is a survey of the literature relevant to the topic of poroviscoelasticity and hydrodynamic lubrication. These subjects encompass two or more fields that are relatively unrelated; therefore, efforts are made to synthesize the literature in a manner that builds towards the final goal of coupling poroviscoelasticity and hydrodynamic lubrication. The chapters that follow provide in-depth discussion of the individual mechanisms, including constitutive relations and numerical treatment.

2.1 *Poroelasticity*

Poroelastic theory is historically used in the field of soil mechanics [21]. The principle use for poroelastic theory is to determine deformation and settling between man-made structures and the earth. A famous example of this soil contraction is the *Tower of Pisa*, which is partially constructed on a creek bed. Over time, the weight of the tower caused consolidation that resulted in the tower leaning. Consolidation is the contraction of soil caused by fluid exodus from a porous medium.

In 1923, Terzaghi [22] provided the constitutive foundation for the consolidation mechanism, launching the field of modern soil mechanics. Rendulic [23] extended Terzaghi's 1D consolidation model to three dimensions in 1936, but Biot [24, 25] is credited with developing the theory of linear poroelasticity. Biot's poroelastic theory considers the same consolidation mechanism as proposed by Terzaghi, but Biot's theory is generalizable beyond soil mechanics. At its core, poroelasticity describes biphasic (or triphasic) materials, and many solid-fluid interactions are governed by its mathematical relations. These include biomechanics [26–30], soil mechanics [21, 31], and even oncology [32]. The generality of linear poroelasticity is due in part to

its robust formulation, which is based on linear elasticity, Navier-Stokes equations, and Darcy's law for flow through a porous medium. Poroelasticity depends on four material parameters: two well-known elastic properties, and two properties related to the porosity and fluid in the medium.

Poroelasticity has a temporal component due to fluid influx or exodus (governed by Darcy's law). This flow manifests as a dissipation when the porous matrix is compressed. Permeability of the porous matrix and the effective pressure gradient on the matrix govern the rate of dissipation. It should be noted that dissipation refers to the exodus of fluid, and not to a thermodynamic process. In that respect, poroelasticity does not have an internal dissipation mechanism and the process of deformation is thermodynamically reversible.

At its roots, poroelasticity is a simple model; however, a number of modifications to the linear theory are used for more complex materials. Biot [14–17, 33–39] added transverse isotropy, anisotropy, and viscoelasticity (discussed later) to poroelastic theory. Additional mechanisms are considered with non-linear phenomena such as finite strains [40,41] and varying porosity [42]. These properties are particularly useful in tissue mechanics, where large deformations are common [43,44]. The current work targets linear poroviscoelasticity, which is the coupling of linear poroelasticity and viscoelasticity. Biot [14–16] introduces poroviscoelasticity in broad terms, which will be discussed after viscoelasticity is vetted in the following section.

2.2 *Viscoelasticity*

Unlike the poroelastic theory discussed previously, viscoelasticity does contain a mechanism for dissipating energy. Viscous heating is the predominant mechanism for this loss, although viscoelastic theory can incorporate many internal losses. The characteristic behavior of viscoelasticity is hysteresis, like that shown in Fig. 1. In essence, a viscoelastic material cannot return the same energy that was required to perform
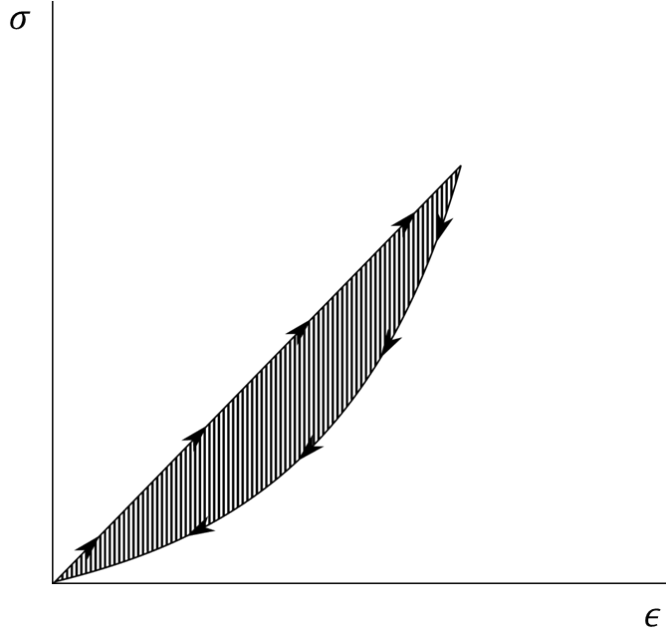
Figure 1: Loading/unloading cycle for a linear viscoelastic material

an action. This distinguishes viscoelastic behavior from poroelastic behavior, and indicates that the two materials be combined without overlapping mechanisms.

The temporal dissipation of viscoelasticity appears in many biological materials [1, 45–47]. The hallmark of this dissipation is a rich frequency dependent behavior. This behavior can be used in earthquake dynamics [5], rotordynamics [10, 11, 13, 48], and many other applications. If correctly harnessed, this frequency dependent dynamic stiffness and damping may also be desired for tribological applications. Much of the current work centers around this concept.

A number of formulations exist to constitutively describe viscoelasticity. A few of these models are discussed herein and are classified by type: integer order or fractional. Both types of viscoelasticity are permissible in a thermodynamic sense, and both models enjoy certain advantages. The constitutive relations for a number of configurations are provided herein, and the choice of model is usually made with respect to fit. Fractional calculus viscoelasticity is still an area of active research [2, 49–

57], and the current work addresses techniques for expediently simulating fractional models in the time-domain. This remains a large challenge, and one that may hinder further progress for fractional calculus viscoelasticity.

Viscoelastic materials contain simultaneous elastic and dissipative mechanisms. These mechanisms are analogous to springs and dashpots, respectively. The combination of springs and dashpots gives a strong time and frequency domain response. Many real materials are viscoelastic, and their use is often intentional for tunable dissipation purposes. In the current study, the viscoelastic mechanism is developed in the solid skeleton of the porous matrix. The viscoelastic action, combined with the porous action, makes for a unique coupled system. To couple the porous matrix and viscoelastic theory, poroviscoelasticity is introduced.

2.3 Poroviscoelasticity

The development of poroviscoelasticity is the synthesis of poroelasticity and viscoelasticity. Biot [14] pioneered the approach by utilizing the correspondence principle, which allows for straightforward conversion from elastic to viscoelastic behavior. Biot's 1954 paper described a very broad way to include viscoelasticity into poromechanics, specifically soil mechanics. Later refinements from Biot and others [15–17] allowed for the viscoelasticity to be included in targeted areas, such as the solid components (e.g. the shear and bulk properties). In doing so, the poroviscoelastic model was given a straightforward framework in that the viscoelasticity is contained in the "traditional" material response, not in the porosity. Therefore, the elastic portions from poroelasticity are replaced with viscoelastic components in poroviscoelasticity. Four material parameters are required to define a poroviscoelastic response: two time-dependent relaxation moduli corresponding to their elastic counterparts (e.g. bulk and shear relaxation moduli), and two properties related to porosity and the fluid component (retained from poroelasticity).

Proper formulation of the viscoelastic component is critical in poroviscoelasticity. The most common models used are the Kelvin-Voigt model and the standard linear solid model (SLS). Both models contain springs and dashpots, but the location of these elements is altered between the two models. Setton et al. [58], Wilson et al. [6,7] and Liu and Ovaert [59] use a SLS poroviscoelastic formulation for articular cartilage, and Abousleiman et al. [60], uses the Kelvin-Voigt model for soil mechanics. Both models are capable of describing creep and stress-relaxation, and both are robust models for poroviscoelasticity. An infinite number of spring-dashpot hierarchies exist as viscoelastic models, but the Kelvin-Voigt and standard linear solid are the most widely used in poroviscoelasticity [42].

The porous and viscoelastic components of poroviscoelasticity give two unique mechanisms for dissipative effects. The synthesis of these phenomena are found in natural systems, where they operate very effectively. For instance, articular cartilage is a poroviscoelastic material. When healthy, cartilage is a durable, load facilitating material that lasts for many decades and millions of cycles. Cartilage also adapts as the body changes (weight, gait, etc.). A component of this is biological, but the structure and composition of cartilage is also designed in a favorable manner. Therefore, it is desired to understand the physics of poroviscoelasticity for use in biological and traditional systems. A natural use for poroviscoelastic materials is envisioned in tribological applications, which is discussed in the following section.

2.4 Hydrodynamic Lubrication

To this point, the literature survey has focused only on the porous pad. The goal of the current study is to couple the porous pad to a tribological system; therefore, a discussion of hydrodynamic lubrication is relevant.

The study of thin lubricant films, and their ability to sustain loads, is over a century old [61]. The well-known Reynolds equation, which is a reduction of the

Navier-Stokes equations combined with conservation of mass, is ubiquitous in tribology. However, less research has focused on the Reynolds equation interfacing with a porous boundary. Works that do interface hydrodynamic lubrication and porous pads include Wu [62], who considered the squeeze-film effects in a porous disk, Prakash and Vij [63], who looked at porous journal bearing operation, and Etsion and Michael [64], who considered a porous mechanical face seal. These works maintained a rigid profile in the porous pad. Bujurke et al. [29,30,65,66] and Elsharkawy et al. [12,67] are some of the first to incorporate a flexible boundary at the fluid film/porous pad interface. These works provide the foundation for the current study, where the additional component of viscoelasticity is introduced. The critical aspect of porous hydrodynamic lubrication is that a boundary condition of the Reynolds equation is modified to allow fluid diffusion across the porous interface. This is discussed in further detail in Chapter 5.

2.5   Summary

The literature surveyed in this chapter establishes a theoretical foundation for the work performed herein. At its essence, the goal of the current work is to combine well-established theories and models in a novel way. At the time of writing, there is almost no body of work established in the fields of fractional calculus porovisoelasticity, or coupled poroviscoelasticity and hydrodynamic lubrication. The current work aims to develop these fields, and provide implementable information for the numerical and finite element aspects of the coupled processes. The constitutive and numerical details of poroviscoelasticity and hydrodynamic lubrication are addressed in their respective chapters.

CHAPTER III

POROVISCOELASTIC MODEL

The concepts introduced in Chapter 2 are now explored in-depth. The constitutive framework of poroviscoelasticity is built by developing viscoelasticity, poroelasticity, and then combining the two. The poroviscoelastic formulation is discussed relative to a finite element approach, and then provided within the framework required by ABAQUS. From there, a hydrodynamic load is coupled to the poroviscoelastic pad, and the resulting system is simulated in time.

3.1   *Viscoelastic Background*

Viscoelasticity is a material type that describes many common engineering materials like polymers, elastomers, and many alloys. The hallmark of these viscoelastic materials is a time-dependent behavior caused by considerable energy dissipation (hysteresis). The dissipation of energy manifests as heat, sound, and/or rearrangement of molecular structure, and occurs temporally. This means that the stress/strain relationships are time (and conversely, frequency) dependent. The stress/strain relationship for a viscoelastic material is traditionally defined by one of two mechanisms: creep or stress relaxation. Both mechanisms describe the relationship between stress and strain, depending on the choice of independent variable. For instance, if a fixed force (stress) is applied to a viscoelastic material, creep will occur as time progresses. Conversely, if a fixed displacement (strain) is applied, stress relaxation occurs. Both creep and stress relaxation are shown in Fig. 2 for a uniaxial experiment. The time-dependent viscoelastic behavior is clear. This is in contrast to an elastic material, which is time-invariant. The time history must be accounted for when modeling viscoelastic materials.
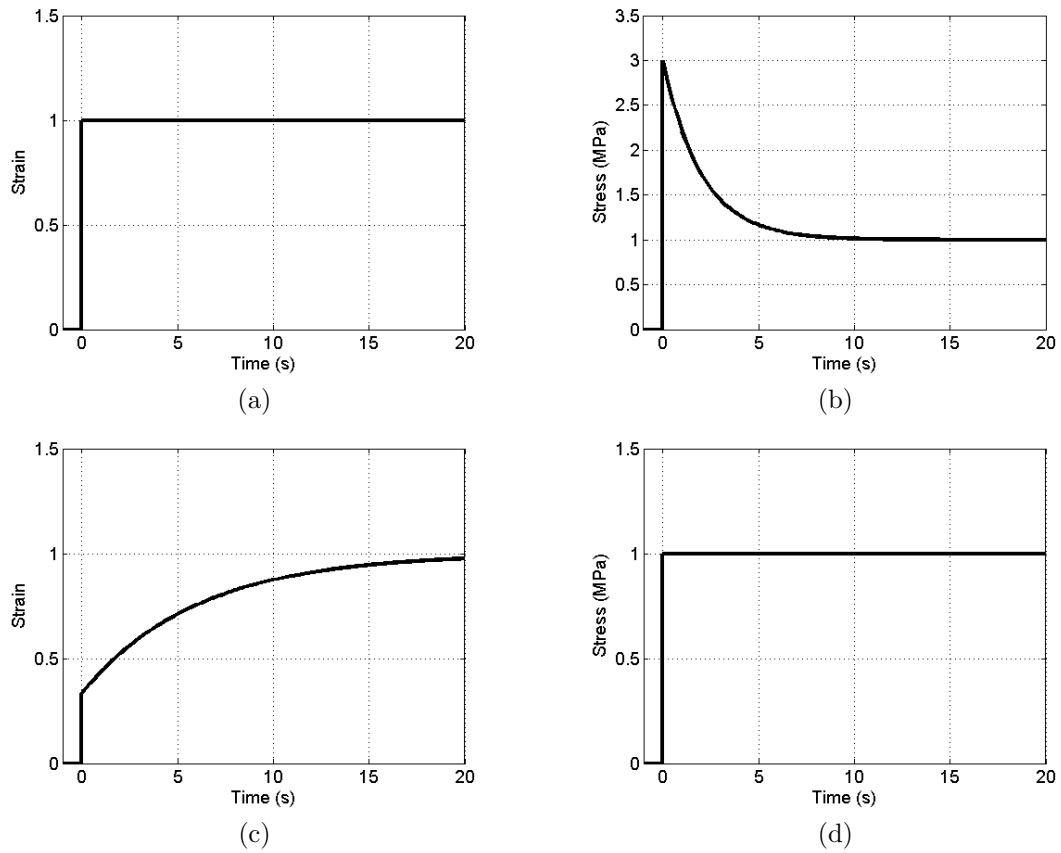
Figure 2: Viscoelastic material behavior during stress-relaxation and creep (a) strain during stress-relaxation; (b) stress during stress-relaxation; (c) strain during creep; (d) stress during creep

As discussed herein, viscoelasticity is constitutively defined by a relaxation modulus or a creep modulus. These mechanisms correspond to the behavior exhibited in Figs. 2b and 2c, respectively. This designation is based on the independent variable (strain or stress). The relaxation modulus is often used because finite element studies are displacement driven, and the goal of the current work is to be compatible with finite element analysis. In either formulation, the temporal energy dissipation of a viscoelastic material corresponds to simultaneous elastic and dissipative mechanisms. These elastic and dissipative mechanisms are clearly viewed in the frequency domain, where the elastic component corresponds to a real part, and the dissipative component to an imaginary part. For a relaxation modulus, these parts are known as the storage and loss moduli, as shown in Fig. 3. These moduli are primarily considered in the frequency domain, giving a clear picture of the simultaneous mechanisms of a viscoelastic material.

Two additional definitions are classic in viscoelasticity: the glassy and rubbery moduli. These definitions are based on two common viscoelastic materials. For example, glass displays viscoelastic behavior: at room temperature, glass acts like a brittle material, and will fracture if brought to failure accordingly. However, at high temperatures, glass acts like rubber when acted upon. The glassy modulus occurs about time $t = 0$, which corresponds to the highest frequencies or lowest temperatures, as shown in Fig. 3. The rubbery modulus is at the opposite end of the spectrum from the glassy modulus. At large time-scales (low frequencies), or high temperatures, a viscoelastic material acts like a rubber. While the rubbery modulus can be zero, most viscoelastic materials have a non-zero rubbery modulus. For behavior between the glassy and rubbery modulus, the material is in a transition region, seen in Fig. 3. Notably, higher energy dissipation (indicated by the loss modulus) occurs in the transition region.

Proper formulation of the viscoelastic constitutive model is critical. Many common
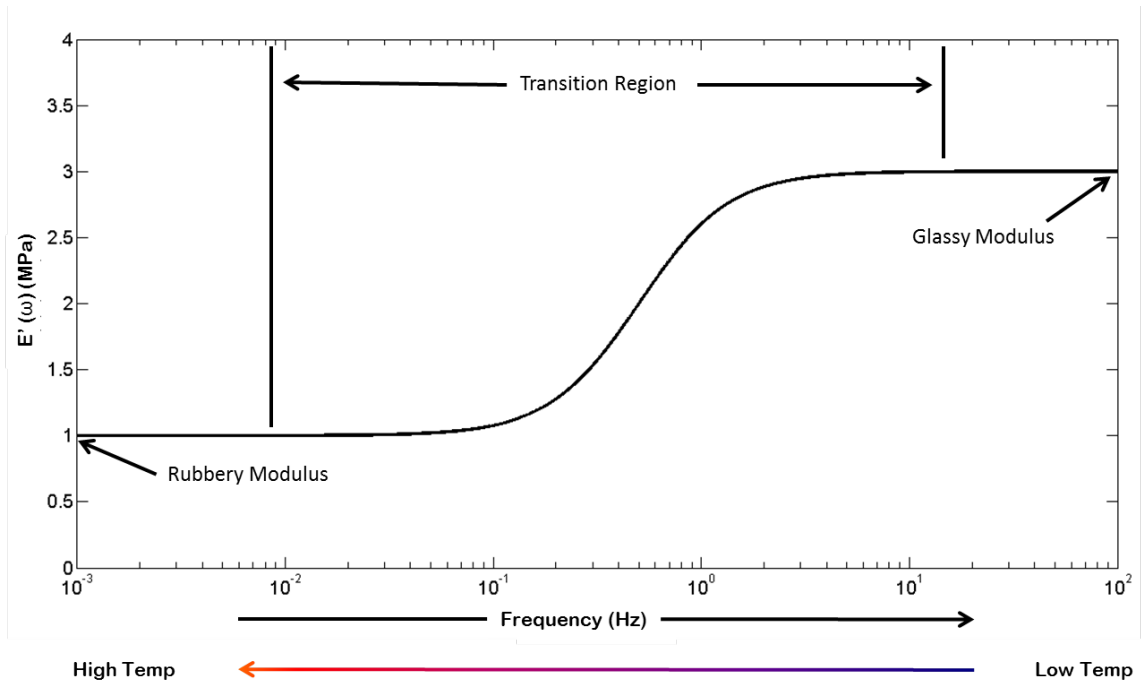
(a) Storage moduli of sample viscoelastic material (semi-log scale)
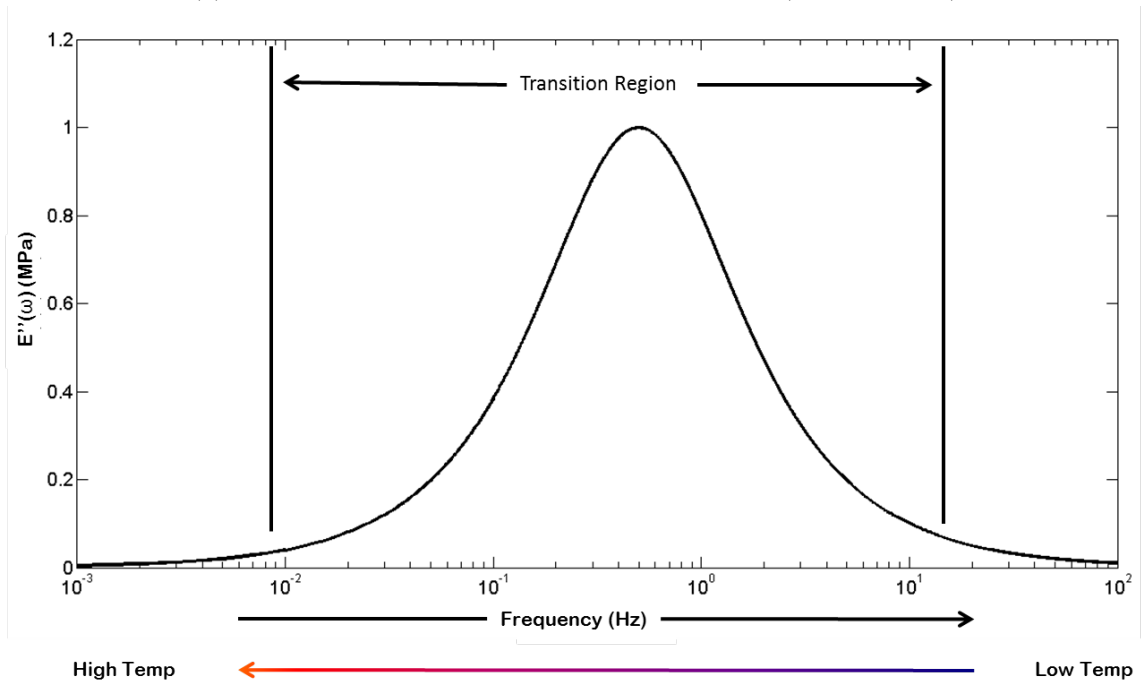
(b) Loss moduli of sample viscoelastic material (semi-log scale)

Figure 3: Storage and loss moduli of sample viscoelastic material

models like the Kelvin-Voigt model and the standard linear solid model (SLS) are used to describe viscoelasticity. Both models are capable of describing creep and stress-relaxation, and both have mechanical analogues. However, any number of formulations can be envisioned, as long as they are thermodynamically permissible, as discussed in the following section.

3.2 Viscoelastic Constitutive Equations

Previously, viscoelasticity was described heuristically as a time-dependent material phenomena. In practice, a mathematical formulation must be constructed. The following work provides a model of viscoelasticity, and explores efficient algorithms to simulate viscoelastic behavior in practical applications.

Gurtin and Sternberg [68] propose a convolution type definition of linear viscoelasticity. The uniaxial model relates stress, strain and a relaxation modulus using Boltzmann's superposition principle:

$$\sigma\left(t\right) = \epsilon\left(0\right) E\left(t\right) + \int_0^t \dot{\epsilon}\left(\tau\right) E\left(t - \tau\right) \, \mathrm{d}\tau. \tag{1}$$

where $\sigma\left(t\right)$ is the stress, $\epsilon\left(t\right)$ is the strain, and the relaxation modulus is denoted by $E\left(t\right)$. Typically, $\sigma(t)$ and $\epsilon(t)$ are either set or measured during experimentation, while $E\left(t\right)$ is obtained from a fixed strain input $\epsilon = \epsilon_{step}$, such that $E(t) = \sigma(t)/\epsilon_{step}$. The parameters of stress, strain, and relaxation modulus in Eq. 1 are time-dependent. Boltzmann's superposition principle simply states that each increment makes an independent contribution to the total response. Therefore, the entire history is represented by the convolution integral. The superposition principle also describes the linear response of stress and strain. To relate strain and stress, the creep modulus $J(t)$ is used:

$$\epsilon\left(t\right) = \sigma\left(0\right) J\left(t\right) + \int_0^t \dot{\sigma}\left(\tau\right) J\left(t - \tau\right) \, \mathrm{d}\tau. \tag{2}$$

Both formulations (Eqs. 1 and 2) describe viscoelastic behavior, and the choice of

independent variable dictates which moduli (relaxation or creep) is used. A theoretical relationship exists between the creep and the relaxation moduli; however, many constitutive formulations of $E(t)$ and $J(t)$ do not directly translate (a noteworthy exception is the Zener viscoelastic material model). It is common to choose one formulation based on the type of problem encountered. For displacement driven simulations, the relaxation modulus is used. When both formulations are necessary, numerical interconversion techniques are used to convert stress relaxation to creep, and *vice versa*.

The uniaxial expressions in Eqs. 1 and 2 illustrate the linear relationship between strain and stress; however, they are not general to a three-dimensional material description. The full material description for a viscoelastic material is analogous to a three dimensional linear elastic material, except the convolution operation persists in the viscoelastic model. To further illustrate this concept, the elastic-viscoelastic correspondence principle is introduced.

The elastic-viscoelastic correspondence principle is mathematically simple, but phenomenologically important. The viscoelastic models (Eqs. 1 and 2) are transferred to the Laplace domain:

$$\sigma\left(s\right) = sE\left(s\right)\epsilon\left(s\right), \tag{3}$$

$$\epsilon\left(s\right) = sJ\left(s\right)\sigma\left(s\right). \tag{4}$$

The viscoelastic terms ($sE\left(s\right)$, $sJ\left(s\right)$) act like linear terms (similar to Hooke's Law) in the Laplace domain. The traditional elastic elements, E and J, have simply been replaced with viscoelastic elements. This is a powerful formulation because no condition has been placed on the relaxation and creep moduli, except that they must be thermodynamically permissible. A variety of such models can theoretically be used. Therefore, one modulus, either creep or relaxation, describes the complete uniaxial transient properties of a viscoelastic material.

The relationship between creep and relaxation is apparent in the Laplace domain:

$$s^2 J(s) E(s) = 1. \tag{5}$$

Certain formulations of the relaxation and creep moduli are conveniently related by Eq. 5. This is further discussed in Chapter 4.

The relationship between the Laplace and frequency domains allows for a straight-forward transformation of the relaxation modulus to the frequency domain. The analytical forms of the Laplace and Fourier domains show the relationship between Laplace variable s and frequency variable $i\omega$:

$$\mathcal{L}\{g(t)\} = G(s) = \int_0^\infty g(t)e^{-st}\,\mathrm{d}t. \tag{6}$$

$$\mathcal{F}\{g(t)\} = G(\omega) = \int_{-\infty}^\infty g(t)e^{-i\omega t}\,\mathrm{d}t. \tag{7}$$

When the system is causal ($g(t) = 0, \forall\, t < 0$), the s can be replaced with $i\omega$, where i is defined as $\sqrt{-1}$ and ω is the frequency in rad/s. Hence, applying $s \to i\omega$, Eq. 3 becomes:

$$\sigma(\omega) = (i\omega) E(\omega) \epsilon(\omega) \triangleq E^*(\omega)\epsilon(\omega) \tag{8}$$

where:

$$E^* = (i\omega) E(\omega) \tag{9}$$

E^* is the complex modulus, which has two components- a real and an imaginary:

$$E^*(\omega) = E'(\omega) + iE''(\omega) \tag{10}$$

The real component (E') is the aforementioned storage modulus, while the imaginary component (E'') is the loss modulus. The storage and loss moduli are represented in Figs. 3a and 3b, respectively. The power of the correspondence principle is clear: one constitutive formulation determines the amount of modulus retained (stored) or lost (loss) as a function of frequency. These properties are particularly important in a dynamic analysis, as they are analogous to the properties of stiffness and damping.

19

3.3   Models with a Mechanical Analogue

The constitutive formulation presented in the previous section depends on the accurate formulation of the relaxation or creep modulus. The traditional way to determine the relaxation modulus, $E(t)$, or the creep modulus, $J(t)$, is to use spring and dashpot hierarchies. Spring and dashpot models have both elastic and dissipative mechanisms simultaneously [39, 68–70]. These dissipative mechanisms are rate dependent, like a viscoelastic material. Multiple arrangements of springs and dashpots are commonly used: Maxwell, Kelvin-Voigt, and any number of combinations of the two. Spring and dashpot arrangements are traditionally robust in their description of viscoelastic materials; however, they can require many terms (degrees of freedom) to accurately describe viscoelastic behavior. Complex models are prohibitive in regards to simulation time, extrapolation to a wide range of subjects, and cohesion between model and material behavior.

One popular mechanical model for viscoelasticity is the Prony series. Shown in Fig. 4a, the Prony series accurately describes creep and stress relaxation mechanisms. The Prony series model is composed of a free spring and an infinite series of Maxwell elements in parallel. Each Maxwell element is an individual spring and dashpot in series. The Prony series captures a wide spectrum of behavior- at high frequencies (or short times) the dashpots "lock," and become rigid. Here, only the springs contribute to the mechanical response. At low frequencies (long time periods), the individual Maxwell elements have no contribution to the overall load support (the dashpots in the Maxwell elements transmit a negligible force). Therefore, the only load support comes from the free spring, E_0. For stress relaxation, the functional form of the Prony series combines multiple exponentially decaying functions:

$$E(t) = E_0 + \sum_{n=1}^{\infty} E_n e^{-\lambda_n t}, \tag{11}$$

where λ is related to the spring and damper constants by $\lambda_n = E_n/\eta_n$. The infinite
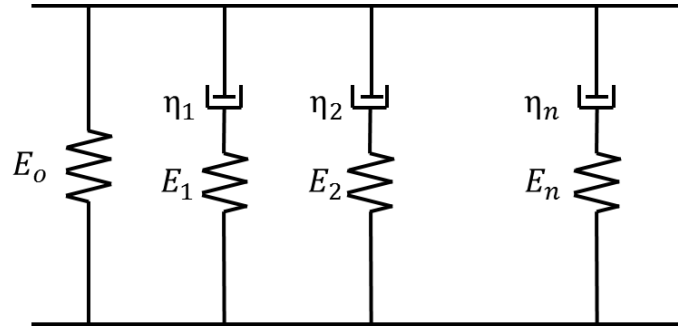
(a) Prony series
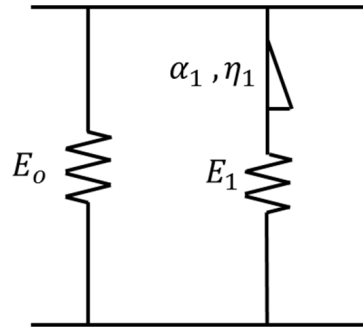
(b) Fractional model

Figure 4: Mechanical interpretation of Prony series and fractional calculus phenomenological models

sum in Eq. 11 allows for different decades of relaxation. Although the Prony series is a robust model, it may require a large number of Maxwell elements to fully capture material behavior. If a large number of terms are required, then the subsequent eigenvalue problem is expanded. In practice, this is computationally expensive and can make extrapolation more difficult. For simplicity, a Zener material is often utilized, where $n = 1$ in the Prony series.

3.4 Fractional Calculus Viscoelastic Model

Fractional calculus is a departure from the familiar integer-order calculus. The utility of fractional calculus is that it provides unlimited flexibility in the description of physical phenomena. However, there is additional mathematic complexity that is assumed with fractional calculus. For example, consider the function:

$$y = t^2. \tag{12}$$

The derivative is computed as:

$$\frac{dy}{dt} = 2t. \tag{13}$$

The fractional derivative is given as:

$$\frac{d^\alpha y}{dt^\alpha} = \frac{\Gamma(3)}{\Gamma(3-\alpha)} t^{2-\alpha}, \tag{14}$$

where Γ in the gamma function: $\Gamma(t) = (t-1)!$. Equation 14 displays a hybrid behavior between integer derivatives. This is shown in Fig. 5, where the fractional derivative is bound by the integer derivatives $\alpha = 0$ and $\alpha = 1$. For any fraction between zero and one, a hybrid behavior is found. The example shows the applicability of fractional calculus for physical behavior that does not conform to an integer-order calculus representation. Viscoelastic materials often display such characteristics [50–55, 71–73].

Many times, fractional calculus is used to describe viscoelasticity because it reduces modeling complexity (i.e the number of unique elements needed to model a viscoelastic material) [50–55, 71–73]. Fractional elements, or "spring-pots," yield a
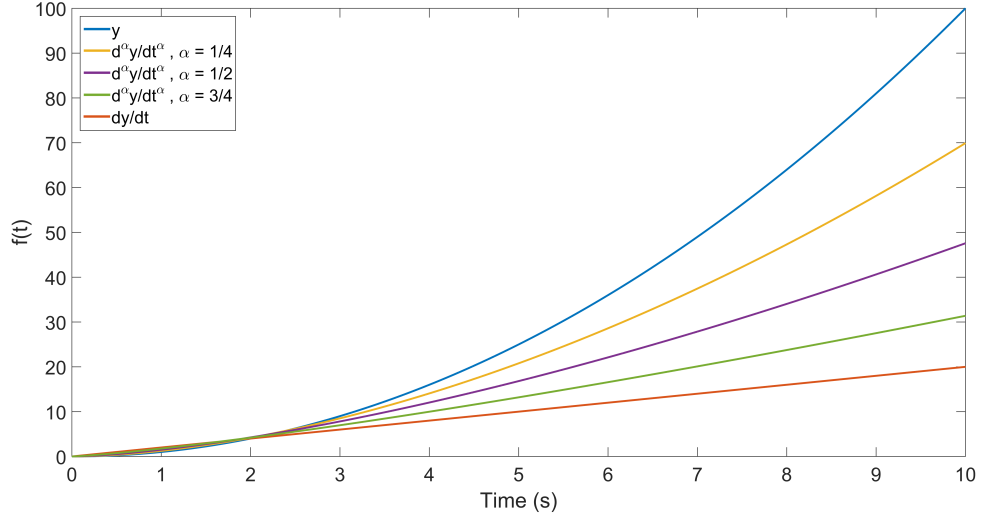
Figure 5: Example of fractional derivatives relative to integer-order derivatives

hybrid material response between a spring and a dashpot. In fact, fractional elements are often represented by complicated spring-dashpot hierarchies [74–76]. An example of one such hierarchy, or ladder model, is shown in Fig. 6.

While fractional calculus is a departure from conventional integer-order calculus, the mathematics are actually simplified [77] because the fractional formulation for viscoelasticity requires fewer elements [2]. This is advantageous compared to the standard viscoelastic models [57,78]. The compactness of the fractional model leads to many viscoelastic applications from biomimetics to geophysics to molecular dynamics [49, 50, 79]. Discussed herein, the challenge is to simulate fractional calculus models numerically.

Shown in Fig. 4b, fractional calculus replaces the damper in the Prony series with a "spring-pot." Mathematically, the spring-pot describes a hybrid spring and dashpot behavior:

$$\sigma_P = \eta \frac{d^\alpha \epsilon_p}{dt^\alpha}. \tag{15}$$

The spring-pot is regulated by the parameter α, which interpolates between spring and dashpot behavior, giving the fractional model more flexibility than the Prony

23
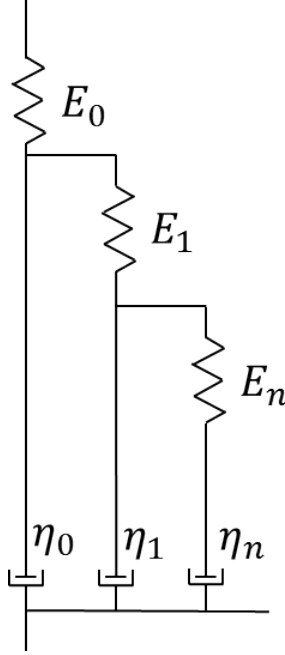
Figure 6: Example of fractional elements relative to integer-order elements

model:

$$E(t) = E_0 + \sum_{n=1}^{\infty} E_n E_\alpha \left(-\frac{E_n}{\eta_n} t^{\alpha_n} \right), \qquad (16)$$

where E_α is the Mittag-Leffler function [80]:

$$E_\alpha(z) = \sum_{k=0}^{\infty} \frac{z^k}{\Gamma(\alpha k + 1)}. \qquad (17)$$

Typically, the flexibility of the fractional model means that fewer elements are needed to fully characterize relaxation behavior. The fractional model has clear utility in modeling applications. However, due to the Mittag-Leffler function, the fractional model is challenging to implement in the time-domain without modification (although numerical routines are available from Podlubny [56] that allow for evaluation of the Mittag-Leffler function). A unique case of the fractional calculus model, when $\alpha = 1/2$, yields an unambiguous time-domain representation. This is known as the complementary error function fractional calculus model (CERF) [69]:

$$E(t) = E_0 + \sum_{n=1}^{\infty} E_n e^{\left(\mu_n{}^2 t \right)} erfc \left(\mu_n \sqrt{t} \right), \qquad (18)$$

where E_n and μ_n are material properties and $\mu_n = E_n/\eta_n$. In Eq. 18, the complementary error function ($erfc$) decays at a faster rate than the exponential increases, giving a relaxation behavior. The CERF model is thermodynamically permissible in general [81], and incorporates the flexibility of fractional calculus and the simplicity of integer order derivative models. Previous work [2] shows the CERF model's utility in modeling viscoelastic behavior.

The complementary error function can be computed by most engineering software packages; however, the function can be reduced with an expansion given by Abramowitz and Stegun [82]:

$$erfc(t) = (a_1 y + a_2 y^2 + a_3 y^3 + a_4 y^4 + a_5 y^5)e^{-t^2} \tag{19}$$

$$y = \frac{1}{1 + pt} \tag{20}$$

where p = 0.3275911, a1 = 0.254829592, a2 = −0.284496736, a3 = 1.421413741, a4 = −1.453152027, a5 = 1.061405429. The maximum error of this expansion is $1.5 \cdot 10^{-7}$. Substituting the expansion into Eq. 18 results in a polynomial expression for the relaxation modulus:

$$E(t) = E_0 + \sum_{n=1}^{\infty} E_n(a_1 x + a_2 x^2 + a_3 x^3 + a_4 x^4 + a_5 x^5) \tag{21}$$

where

$$x = \frac{1}{1 + p\left(\mu_n \sqrt{t}\right)}. \tag{22}$$

With Eq. 21, the time-domain relaxation modulus is straightforward. The CERF model has the advantages of the fractional model, with a clear time-domain analogue. In the frequency domain, the CERF model has the following storage and loss moduli:

$$E'(\omega) = E_0 + \sum_{n=1}^{\infty} \frac{E_n \left[\left(\frac{\sqrt{2\omega}}{2}\right)\mu_n + \omega\right]}{\mu_n^2 + \mu_n\sqrt{2\omega} + \omega} \tag{23}$$

$$E''(\omega) = \sum_{n=1}^{\infty} \frac{E_n \left(\frac{\sqrt{2\omega}}{2}\right)\mu_n}{\mu_n^2 + \mu_n\sqrt{2\omega} + \omega}. \tag{24}$$

The storage modulus contains the free term E_0 and as ω approaches infinity $(\omega \to \infty)$, the storage modulus becomes the sum of all of the "spring constants." The loss modulus approaches zero as ω approaches zero $(\omega \to 0)$ and infinity $(\omega \to \infty)$. In the transition region, the loss modulus provides effective positive damping.

Both the Prony series and CERF models are monotonically decreasing in the time-domain, and thermodynamically permissible in general [69]. However, the one-term fractional model is perfectly smooth over the entire frequency domain, which is an advantage it has over the higher-term Prony models. The storage and loss moduli are shown for the fractional fit in Fig. 7. As expected, the storage and loss moduli show the rubbery, transition, and glassy regions of viscoelastic behavior. The seemingly additional mathematical complexity of the fractional model is tolerated because fewer fractional elements are typically required to characterize viscoelasticity, as compared to the Prony model. More elements can be used with the CERF model; however, it is typically not necessary and mitigates an advantage of using fractional calculus. A compact viscoelastic model is desired for implementation in numerical packages. The CERF model is well-suited for this application.

The utility of the CERF model is apparent in the frequency domain, where a one-element function is used to model relaxation. This yields a completely smooth function, which is indicative of the actual material behavior. A one-element model is advantageous for future dynamic analysis and modeling as well. Therefore, it is proposed that the one-element CERF model is a better suited model for viscoelasticity
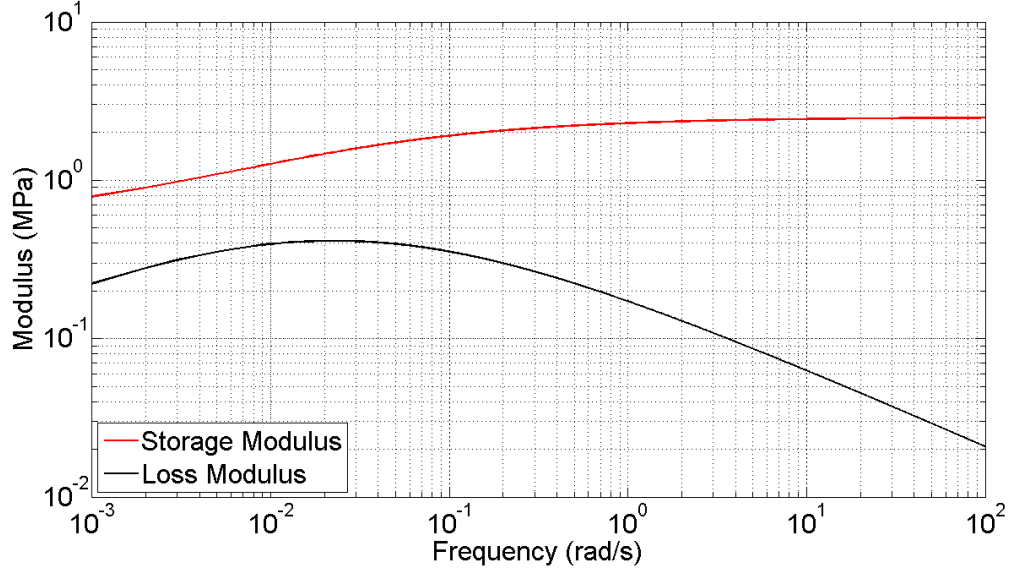
Figure 7: Representative storage and loss moduli of a one-term fractional model

than the traditional mechanical models. The challenge remains to simulate fractional calculus in finite element studies. Numerical routines exist for the Prony series, and the objective of the current work is to develop similar routines for the CERF model.

3.5   Poroelasticity

Poroelasticity is a general constitutive behavior that describes a triphasic material. The roots of poroelasticity are derived from soil mechanics; therefore, the typical description of poroelasticity includes a porous matrix of solid soil particles, permeating fluids, and trapped air in the porous matrix. Equilibrium and continuity equations govern each phase of the poroelastic material, as well as the overall behavior. In fully saturated soils, poroelasticity is biphasic, consisting of solid soil particles and a permeating fluid. The typical mechanics of poroelasticity (incompressible fluid and homogeneous pore structure) are such that Darcy's law is used instead of Navier-Stokes to describe linear momentum in the fluid phase [24,25,31,83]. The constitutive framework for poroelasticity is attributed to Biot [24, 25, 31]. Biot's poroelasticity is given in many equivalent forms [21]; however, the material response is characterized

by four variables: stress (σ_{ij}), strain (ϵ_{ij}), pore pressure (p), and incremental fluid content (ζ). In poromechanics, stress (σ_{ij}) refers to *total stress*, which is the combination of solid and fluid stresses. Strain retains the same definition as it does for an elastic solid [31,84]. Pore pressure (p) is the fluid pressure in the porous subspace, and the incremental fluid content (ζ) describes the increment of fluid entering or leaving a control volume. A set of constitutive equations is required to characterize the solid and fluid interactions. The dependent and independent variables are determined by the analysis type.

3.5.1 Poroelastic Constitutive Equations

The poroelastic constitutive equations are defined by four material properties. These are loosely grouped by poroelastic solid and fluid properties (two material parameters per phase). A number of material properties are available [31, 37]; however, a representative grouping is chosen for illustration. Herein, the drained bulk (K_{ij}) and drained shear modulus (G_{ij}) are used to describe the solid properties, and the Biot moduli H' and R' are used for the fluid properties. Equations 25 and 26 relate strain and stress in a poroelastic medium (using Einstein's notation):

$$\epsilon_{ij} = \frac{\sigma_{ij}}{2G_{ij}} - \left(\frac{1}{6G_{ij}} - \frac{1}{9K_{ij}} \right) \delta_{ij}\sigma_{kk} + \frac{1}{3H'}\delta_{ij}p, \tag{25}$$

$$\zeta = \frac{\sigma_{kk}}{3H'} + \frac{p}{R'}. \tag{26}$$

The linear relationship between strains (ϵ_{ij}, ζ) and stresses (σ_{ij}, p) is apparent, and if the pore pressure is negated, Eq. 25 degenerates to the linear elastic relationship (Hooke's law). Poroelasticity is a compact theory that describes many biphasic materials like soil [14, 15, 17, 21, 25, 31, 33–37, 39, 42], articular cartilage [29, 65], and bone [26, 28]. Effective dissipation occurs by fluid exodus in the porous matrix; however, poroelasticity is a thermodynamically reversible process. If internal dissipation is observed, an additional mechanism is required. This is the impetus for poroviscoelastic theory.

3.6   Poroviscoelasticity

Poroviscoelasticity requires the merger of poroelasticity and viscoelasticity. The afore-mentioned models of poroelasticity and viscoelasticity are combined via the elastic-viscoelastic correspondence principle. Essentially, the correspondence principle allows for a simple substitution of terms to convert an elastic material to a viscoelastic material. The following section describes the procedure used to develop the poroviscoelastic constitutive model.

3.7   Poroviscoelastic Constitutive Equations

Biot was the first to extend the poroelastic theory to poroviscoelasticity by use of the correspondence principle [14]. Biot used operational calculus to replace the elastic coefficients (e.g. G) from poroelasticity with viscoelastic operators [39]. The operators are based on a spectrum of Maxwell-type relaxation elements, which correspond to internal dissipation mechanisms. Each of the four poroelastic terms has a corresponding operator. Biot's formulation is derived from spring and dashpot models, and uses Onsager's theorem and the thermodynamics of irreversible processes. The operator formulation accounts for a relaxation spectrum that results from a finite number or continuous distribution of individual relaxation mechanisms, e.g. physical-chemical interfacial effects. Biot describes these interactions as "hidden coordinates" and accounts for them with a relaxation spectrum that can appear in any of the four material constants. While this approach allows for a wide range of viscoelastic behavior to exist in a material, the use of spring and dashpot models is not required (although it is popular).

In poroviscoelasticity, the viscoelastic action is traditionally applied to the solid material properties only (e.g. G and K) [6, 7, 85, 86]. Whereas poroelastic theory requires the definition of two properties associated with the permeating fluid and two elastic properties (such as bulk and shear modulus), poroviscoelastic theory requires

definition of two fluid properties and two time-dependent material properties. These time-dependent moduli can be given in terms of creep or relaxation. A key consideration is to properly model the viscoelastic component of poroviscoelasticity. A novel approach to poroviscoelastic theory is presented in the next section.

3.8   Development of CERF Poroviscoelastic Model

The poroelastic model given in Eqs. 25 and 26 is rearranged so that stress is in terms of strain (adapted from [25]):

$$\sigma_{ij} = 2G\epsilon_{ij} + \left(K - \frac{2G}{3} \right) \epsilon_{kk}\delta_{ij} - \frac{K}{H'}\delta_{ij}p, \tag{27}$$

$$\zeta = \frac{K}{H'}\epsilon_{kk} + p\left(\frac{1}{R'} - \frac{K}{H'^2} \right). \tag{28}$$

Equation 27 is the form more commonly required for finite element analysis, specifically in ABAQUS. The following two substitutions simplify the poroelastic description:

$$\alpha_{biot} = \frac{K}{H'}, \tag{29}$$

$$\frac{1}{M} = \frac{1}{R'} - \frac{K}{H'^2}. \tag{30}$$

Biot's poroelastic formulation then takes the following form:

$$\sigma_{ij} = 2G\epsilon_{ij} + \left(K - \frac{2G}{3} \right) \epsilon_{kk}\delta_{ij} - \alpha_{biot}\delta_{ij}p, \tag{31}$$

$$\zeta = \alpha_{biot}\epsilon_{kk} + p\left(\frac{1}{M} \right). \tag{32}$$

Using Gurtin and Sternberg's [68] definition of viscoelasticity, Biot's poroelastic model is transformed to a poroviscoelastic model via the correspondence principle. Note that viscoelasticity is introduced in the two solid parameters, G and K, and the dependence on time is made explicit:

$$\sigma_{ij}(t) = 2\left(G * \dot{\epsilon}_{ij} \right)(t) + \left[\left(K * \dot{\epsilon}_{kk} \right)(t) - \frac{2}{3}\left(G * \dot{\epsilon}_{kk} \right)(t) \right]\delta_{ij} - \left[\alpha_{biot}p(t) \right]\delta_{ij}, \tag{33}$$

$$\zeta(t) = \alpha_{biot}\epsilon_{kk}(t) + \left(\frac{1}{M}\right)p(t), \tag{34}$$

where $(*)$ denotes convolution. Assuming causality, the convolution integrals are expressed as:

$$(G * \dot{\epsilon}_{ij})(t) = \int_0^t \dot{\epsilon}_{ij}(\tau)\,G(t - \tau)\,\mathrm{d}\tau, \tag{35}$$

$$(K * \dot{\epsilon}_{kk})(t) = \int_0^t \dot{\epsilon}_{kk}(\tau)\,K(t - \tau)\,\mathrm{d}\tau, \tag{36}$$

$$(G * \dot{\epsilon}_{kk})(t) = \int_0^t \dot{\epsilon}_{kk}(\tau)\,G(t - \tau)\,\mathrm{d}\tau, \tag{37}$$

The remaining step is to define the viscoelastic bulk and shear moduli. This is done with the fractional calculus representation given in Eq. 18 for $n = 1$ (the CERF counterpart to a Zener/Prony model):

$$G(t) = G_0 + G_1 e^{\left(\mu^2 t\right)} erfc\,(\mu\sqrt{t}), \tag{38}$$

$$K(t) = K_0 + K_1 e^{\left(\beta^2 t\right)} erfc\,(\beta\sqrt{t}), \tag{39}$$

Here, $K(t)$ and $G(t)$ have simply been substituted for the relaxation modulus $E(t)$ used previously. At this point, the CERF poroviscoelastic model is defined and can be incorporated into the coupled analysis. Eight total material parameters are required for the constitutive poroviscoelastic equations- three for each viscoelastic term (e.g. G_0, G_1, μ), and two fluid parameters (α_{biot}, M). These parameters are material and application dependent, and will be explored in the analysis of coupled PVE/HDL problems.

3.9   Effective Stress

The analysis of poromechanics is often centered around the concept of effective stress. Terzaghi [22] stated that for fully saturated soils, the total stress (σ) is carried by the soil and the pore water pressure. In saturated soils, the pore pressure and stress in the solid act in tandem to support a load. Figure 8 illustrates this principle. The
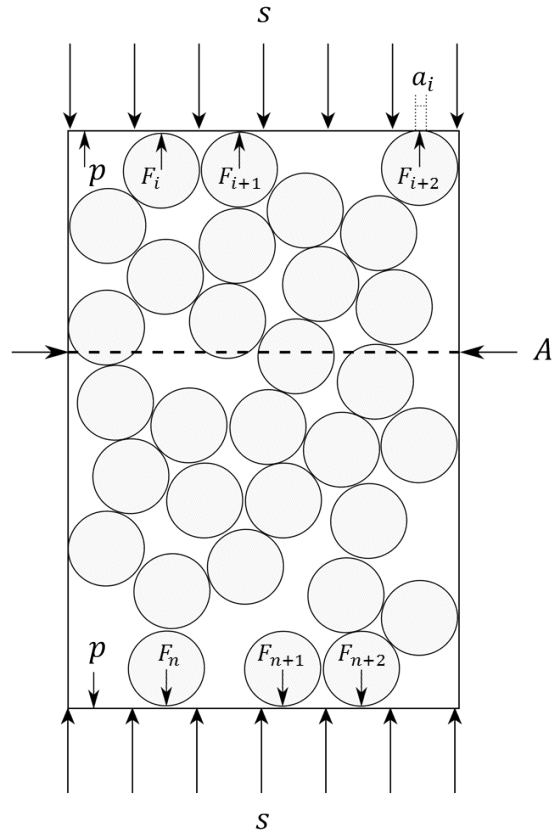
Figure 8: Force balance on representative elementary volume (modified from [83])

contacting solid grains have an *effective* stress of:

$$s' = \frac{\sum F_i}{A}. \tag{40}$$

Although s' does not represent the exact contact stress, it carries the distributed load borne by the solid grains. The pore water pressure fills the remaining (non-contacting) portion of the porous body. Therefore, a force balance performed at the porous interface yields:

$$sA = s'A + p \left[A - \sum_{i=1}^{n} a_i \right]. \tag{41}$$

The contact area is assumed to be small relative to the total area [83]; therefore, the effective stress principle becomes:

$$A \approx A - \sum_{i=1}^{n} a_i, \tag{42}$$

$$sA = s'A + pA. \tag{43}$$

or:

$$s = s' + p. \tag{44}$$

Using the convention of ABAQUS [87], compressive stresses are negative ($s = -\sigma$, $s' = -\sigma'$) and pressures (also acting in compression) are positive. Therefore, the effective stress principle is:

$$\sigma = \sigma' - p. \tag{45}$$

The effective stress principle is a significant simplification in Biot's poroelastic/poroviscoelastic theory, but the experimental results (for soil mechanics) justify its use [31,83,87]. When fully saturated conditions exist and the solid grains are likewise incompressible, $\alpha_{biot} = 1$ and $M \to \infty$. Equations 31 and 32 become:

$$\sigma_{ij} = 2G\epsilon_{ij} + \left(K - \frac{2G}{3} \right) \epsilon_{kk}\delta_{ij} - \delta_{ij}p, \tag{46}$$

$$\zeta = \epsilon_{kk}. \tag{47}$$

Equation 46 indicates that the pore pressure and solid grain response are independent contributors to the overall response, and Eq. 47 shows that changes in the solid structure are offset by corresponding changes in the fluid content. Therefore, the effective stress principle is obtained:

$$\sigma'_{ij} = 2G\epsilon_{ij} + \left(K - \frac{2G}{3} \right) \epsilon_{kk}\delta_{ij}, \tag{48}$$

and

$$\sigma_{ij} = \sigma_{ij}' - p\delta_{ij}. \tag{49}$$

The extension to poroviscoelasticity is made naturally because of the effective stress principle. When the viscoelasticity is applied only to the solid grains of the porous medium, the effective stress becomes:

$$\sigma_{ij} = (\sigma_{ij}')_{VE} - p\delta_{ij}, \tag{50}$$

where:

$$(\sigma_{ij}')_{VE} = 2\left(G * \dot{\epsilon}_{ij} \right)(t) + \left[\left(K * \dot{\epsilon}_{kk} \right)(t) - \frac{2}{3}\left(G * \dot{\epsilon}_{kk} \right)(t) \right]\delta_{ij}. \tag{51}$$

Effective stress distinguishes the role of the solid and fluid components in a porous material. This concept is useful when analyzing the physics of a coupled-type simulation. In addition, effective stress is supported by the FEA package used in this work. For that reason, the effective stress principle represents a large advantage over the full poroviscoelastic simulation. The trade-off in accuracy for fully saturated materials is small [25, 31, 83, 87]. However, if the full poroviscoelastic solution is desired, a user-defined material (UMAT) will be required in the construction of the finite-element software. In addition, a user-defined element (UEL) may also be required, depending on the specification of pore pressure.

3.9.1 Conservation Laws and Solution

Applying momentum conservation and continuity to the solid and fluid phases allows for simulation of the poroelastic problem. To fully specify the poromechanics problem,

boundary and initial conditions are required on the material domain. This includes pore pressure boundary and initial conditions. A number of boundary conditions and loading configurations are discussed in Chapter 6. Commercial FEA packages ensure that force equilibrium and continuity are enforced, and provide expedient solution routines for complicated material and geometric models. Within poromechanics, ABAQUS is able to simulate poroviscoelastic behavior by utilizing effective stress. The solution is strongly coupled to a hydrodynamic loading scenario, which is the subject of a later chapter.

3.10   *Poroviscoelastic Model Validation*

It is desired to use the herein developed PVE model in triboelement simulations. In order to prove feasibility of the PVE model, two validations are performed. The first is to confirm that the fluid pressure in a porous body agrees with established theory. The second comparison is made with experimental data obtained from articular cartilage.

3.10.1   Validation of FEA solution with Laplace's PDE

Pore pressure over a fixed domain is governed by Darcy's law and continuity. Mathematically, a partial differential equation (PDE) is constructed that specifies the pressure in the porous pad. In Cartesian coordinates, this PDE describes the pressure in a porous body (p) as a function of three spatial dimensions (x, y, z):

$$\frac{\partial^2 p}{\partial x^2} + \frac{\partial^2 p}{\partial y^2} + \frac{\partial^2 p}{\partial z^2} = 0 \tag{52}$$

Eq. 52 is known as Laplace's equation, which is an elliptic PDE. For validation purposes, the following 2D boundary value problem is constructed (neglecting the z-direction): the leading and trailing edges of the pad (x-direction) are exposed to atmospheric (gauge) pressure, which allows fluid flow across the boundary. The bottom boundary is fixed, and the top boundary has a constant pressure, p_{max}, along its edge. The pressure gradient in the porous pad facilitates fluid flow throughout the
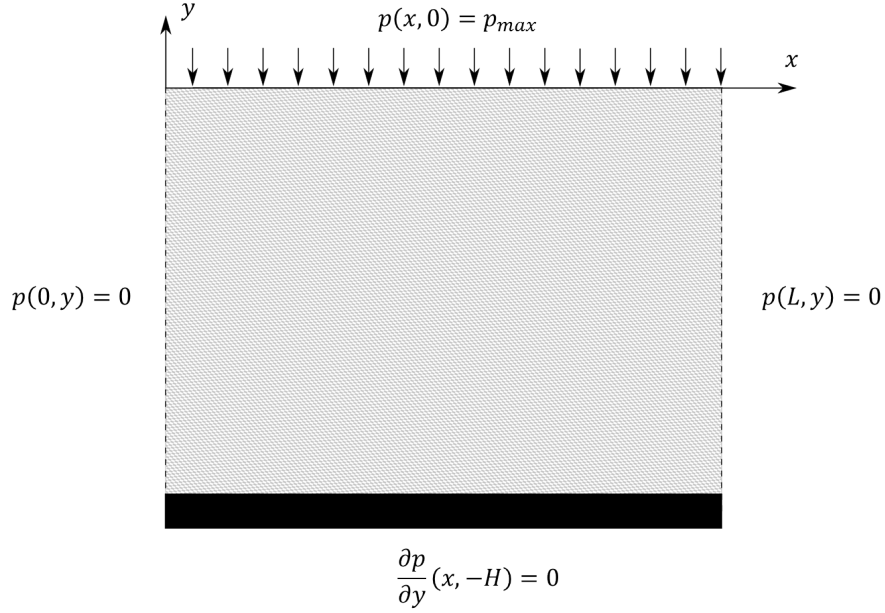
Figure 9: Boundary conditions on porous pad

pad. The pressure boundary conditions are defined mathematically:

$$p(0, y) = p(L, y) = 0 \tag{53}$$

$$\frac{\partial p}{\partial y}(x, -H) = 0 \tag{54}$$

$$p(x, 0) = p_{max} \tag{55}$$

The solution of the boundary value problem is obtained from potential theory. The same problem is posed in ABAQUS (Table 1), and the results are simulated for comparison. Fig. 10a shows the pressure over the porous domain from the analytical solution, and Fig. 10b shows the pressure obtained from ABAQUS. By comparison, there is excellent qualitative agreement between the solutions, and the FEA solution averages less than 1.5% error with the theoretical solution. This indicates that ABAQUS is capable of solving for the fluid pressure in a porous pad. Characterizing the pressure in a porous pad is an important aspect of the PVE model validation. In the following section, a real PVE material is compared to the full PVE formulation in ABAQUS.
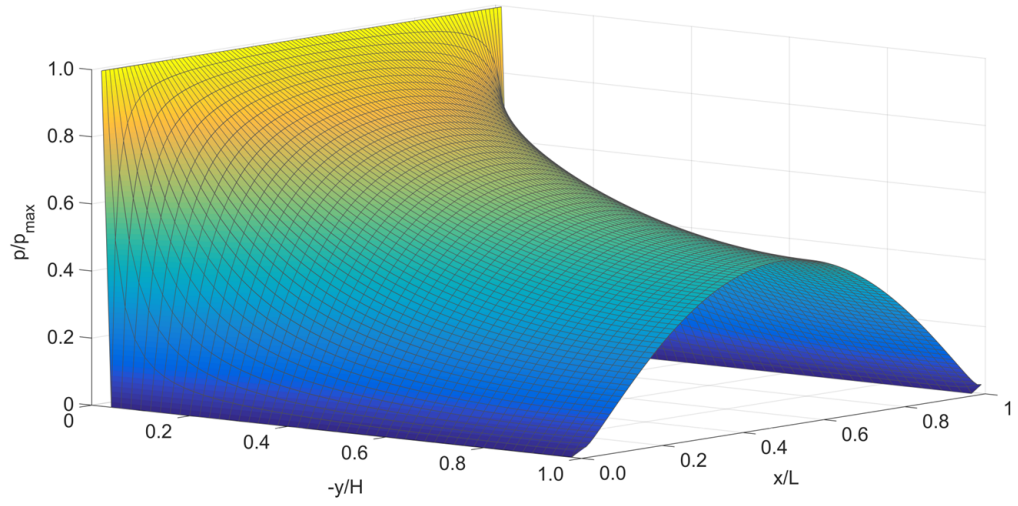
(a) Laplace solution over 2D domain
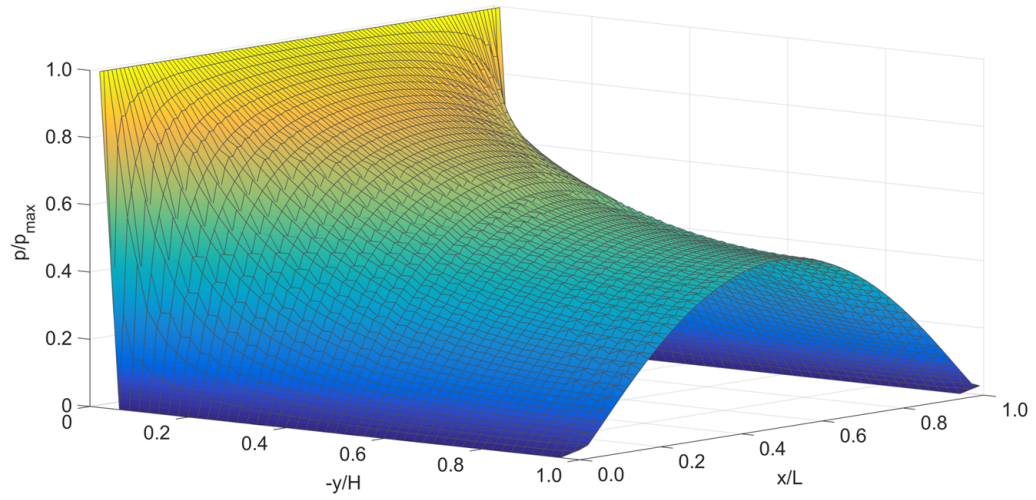
(b) ABAQUS solution over 2D domain

Figure 10: Comparison of analytical pressure solution to FEA solution

Table 1: ABAQUS parameters for Laplace's PDE validation

Parameter	Symbol	Value (units)
Element type		CPE8RP
Porous pad length	L	25.0 (cm)
Porous pad height	H	12.5 (cm)
Pore pressure	p_{max}	1000 (Pa)
# of elements		1250
Configuration		Plane strain
CPU time		8.8 (s)

3.10.2 Articular Cartilage Experimentation

Articular cartilage is recognized as a poroviscoelastic material [6,58,88,89], and serves as a test platform for understanding the physics of coupled solid-fluid interactions in flexible porous bodies. In previous work [1,2], articular cartilage was experimentally tested in stress-relaxation. The details of the experimental work are found in [47]. In short, articular cartilage explants were harvested from recently deceased equine cadavers. 10 mm plugs were created from the stifle joint (analogous to the human knee), and submerged in a biological medium for testing. Stress-relaxation was performed with a CETR UMT3 Tribometer, shown in Fig. 11. After the relaxation tests concluded, thickness measurements were performed on the cartilage plug with a needle probing technique (Fig. 12). These measurements characterize the uniaxial stress/strain relationship of saturated cartilage, and provide a test bed for multiphase materials.

3.10.3 PVE Model in ABAQUS

The experimental results obtained previously are uniaxial because the original research path was different from the current work. In the original research, a phenomenological model of articular cartilage was presented. This model looked at the conglomerate behavior of cartilage, and did not separate the solid and fluid components. Therefore, additional parameters for the permeability and permeating fluid
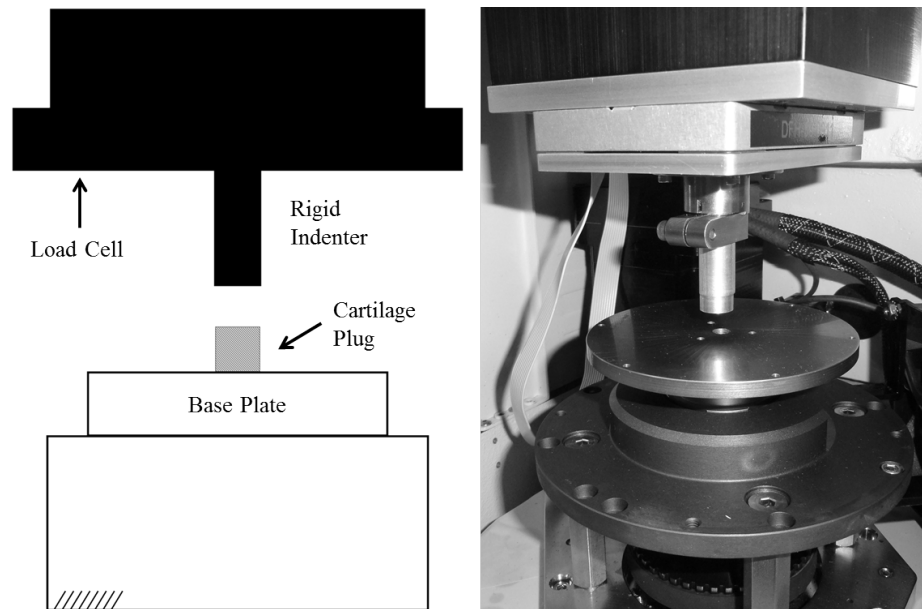
Figure 11: UMT Tribolometer used to test cartilage plug [47]
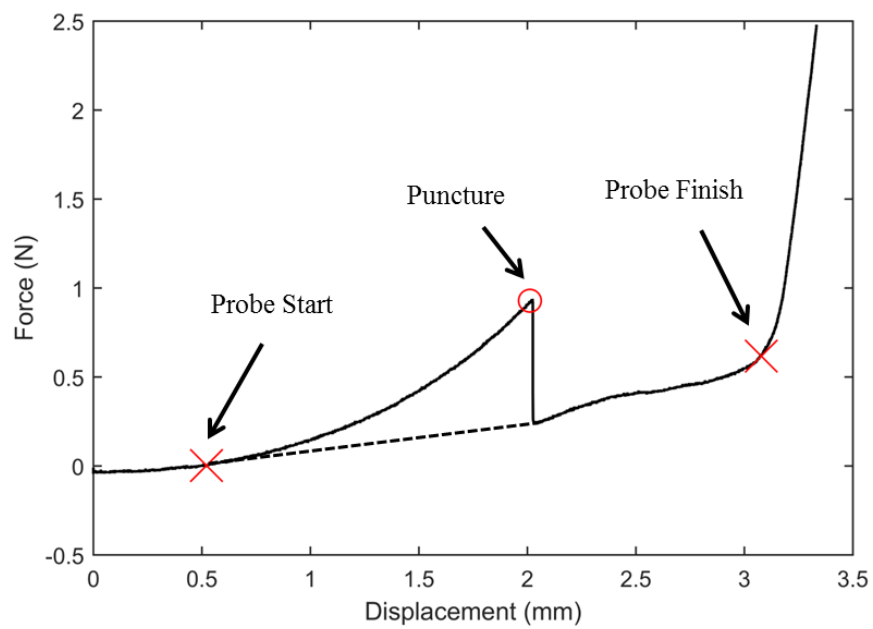
Figure 12: Needle probe techniques used to determine cartilage plug depth

Table 2: ABAQUS parameters used in PVE model validation

Parameter	Symbol	Value (units)
Element type		CAX8RP
Configuration		Axisymmetric
# of elements		1650
Poisson's ratio [90]	ν	0.2
Elastic modulus	E	0.405 (MPa)
PVE pad radius	r_o	5.00 (mm)
PVE pad height	H	3.296 (mm)
Strain/displacement	ϵ_0	7.58%/ 0.250 (mm)
Prony constant (bulk)	k_1	0.13
	k_2	0.1
	k_3	0.11
	k_4	0.035
Prony constant (shear)	g_1	0.13
	g_2	0.1
	g_3	0.11
	g_4	0.035
Prony time constant	τ_1	13.889 (s)
	τ_2	0.5 (s)
	τ_3	2.1277 (s)
	τ_4	83.333 (s)
Hydraulic conductivity (from [91])	K	$10^{-13}(m/s)$
CPU time		100.4 (s)

viscosity (synovial fluid) are needed to specify a poroviscoelastic material. In addition, Poisson's ratio is required to expand beyond uniaxial study. These parameters are obtained from literature as general inputs for analysis [90, 91]. The goal of comparing the experimental results to the PVE model is to verify that the physics of the PVE model are consistent with real material behavior. The PVE model is designed in ABAQUS with the specifications listed in Table 2. The parameters in Table 2 are presented as they would be input into ABAQUS. The dimensions used in Table 2 mimic the geometry of a test from [1, 2, 47]. The values of permeability, viscosity, and Poisson's ratio are obtained from relevant literature [90, 91], and the remaining parameters are fit to the experimental data.

The PVE simulation is designed to duplicate the experimental protocols used in previous work [47]. A transient (relaxation) analysis is simulated in time, and the mean pressure from the simulation is compared to experimental results. The domain is considered axisymmetic, and Figure 13 shows the following boundary and initial conditions on the fluid and solid phases of the material:

$$\frac{\partial p}{\partial r}(0, z, t) = 0 \tag{56}$$

$$p(r_o, z, t) = 0 \tag{57}$$

$$\frac{\partial p}{\partial z}(r, 0, t) = 0 \tag{58}$$

$$\frac{\partial p}{\partial z}(r, H, t) = 0 \tag{59}$$

$$p(r, z, 0_-) = 0 \tag{60}$$

$$\epsilon_r(0, z, t) = 0 \tag{61}$$

$$\sigma(r_o, z, t) = 0 \tag{62}$$

$$\epsilon(r, 0, t) = 0 \tag{63}$$

$$\epsilon_z(r, H, t) = -\epsilon_0 \tag{64}$$

$$\sigma(r, z, 0_-) = 0 \tag{65}$$

Fluid is only allowed to flow in the radial direction, as enforced by rigid platens in the vertical directions. Figure 14 shows the deformation and pore pressure in the cartilage body during stress relaxation. The cartilage plug remains affixed to the bone substrate at the lower boundary ($z = 0$), which explains the radial pinching that occurs at $y = 0$, $r = r_0$. Figure 15 shows the lateral flow of permeating fluid from the body at the atmospheric boundary ($r = r_0$, $t = 30$ s). Finally, Fig. 16 shows the model and experimental data in stress-relaxation (mean pressure at top boundary $z = H$). Excellent agreement exists between experiment and simulation, indicating that the PVE model used herein is capable of simulating real biphasic interactions.

$$\frac{dp}{dz}(r, H, t) = 0 \qquad \epsilon_z(r, H, t) = -\epsilon_0$$

$$\frac{dp}{dr}(0, z, t) = 0$$

$$\epsilon_r(0, z, t) = 0$$

$$p(r_o, z, t) = 0$$

$$\sigma(r_o, z, t) = 0$$

$$\frac{dp}{dz}(r, 0, t) = 0 \qquad \epsilon_z(r, 0, t) = 0$$
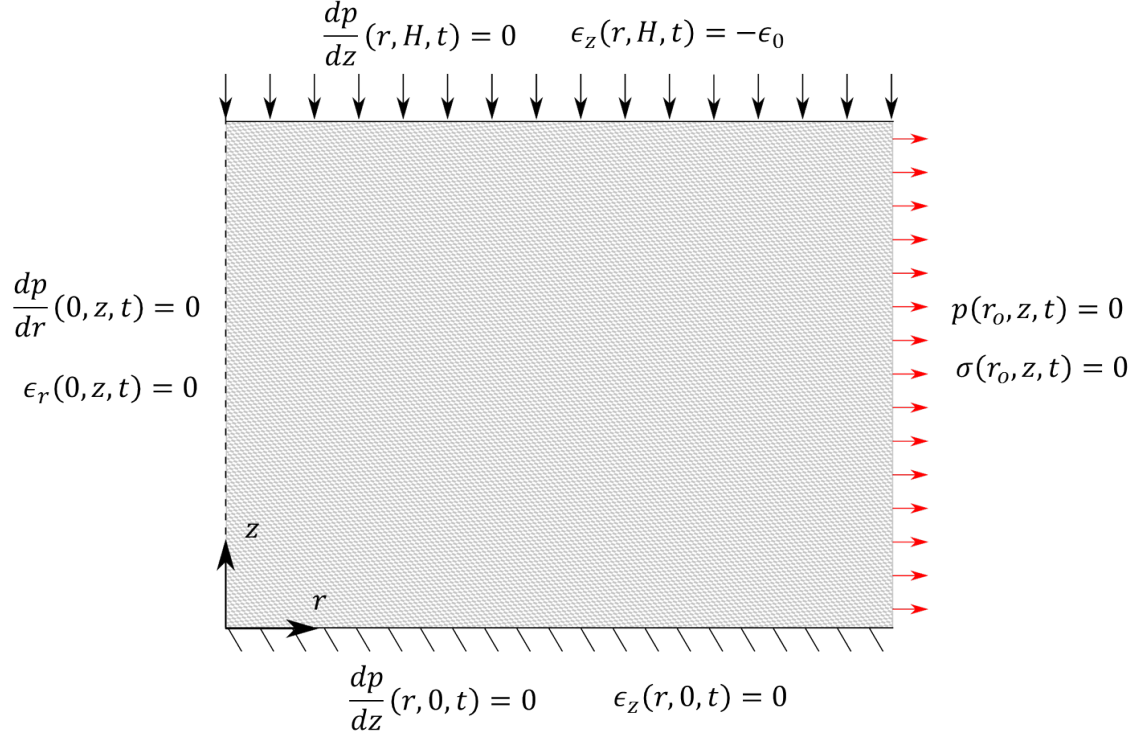
Figure 13: Boundary conditions imposed in cartilage plug simulation

The nature of cartilage is porous and compliant, and the PVE model is adept at describing the physics of such materials [6].

The PVE model is capable of describing complex solid-fluid interactions on the macroscale. The model developed herein is validated in uniaxial stress/strain, and similar formulations are capable of describing full material specifications [6,58,88,89]. In the following chapter, special attention is paid to the viscoelastic formulation used to model the solid contributions of the poroviscoelastic material description.

(a) Vertical deformation in the cartilage plug ($t = 30$ s)

(b) Pore pressure in the cartilage plug ($t = 30$ s)
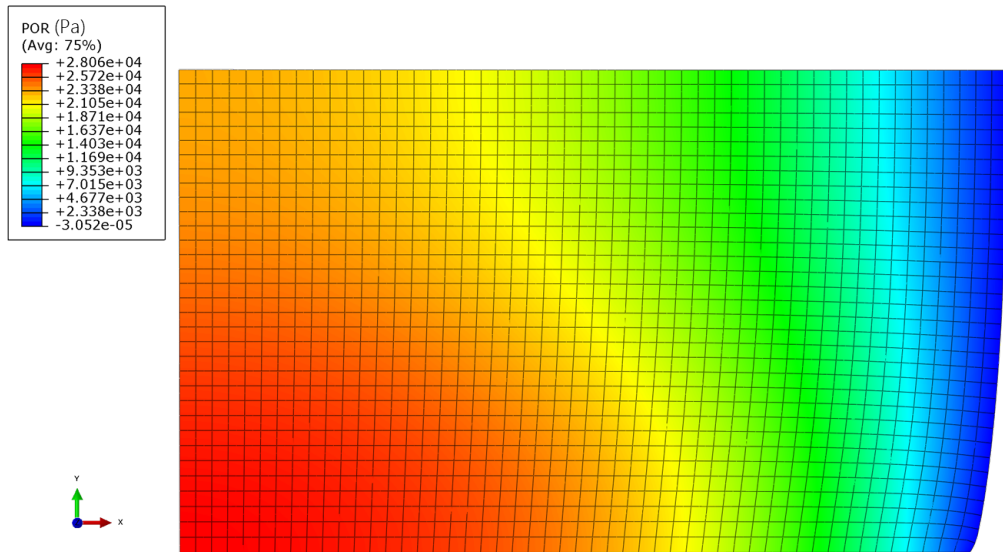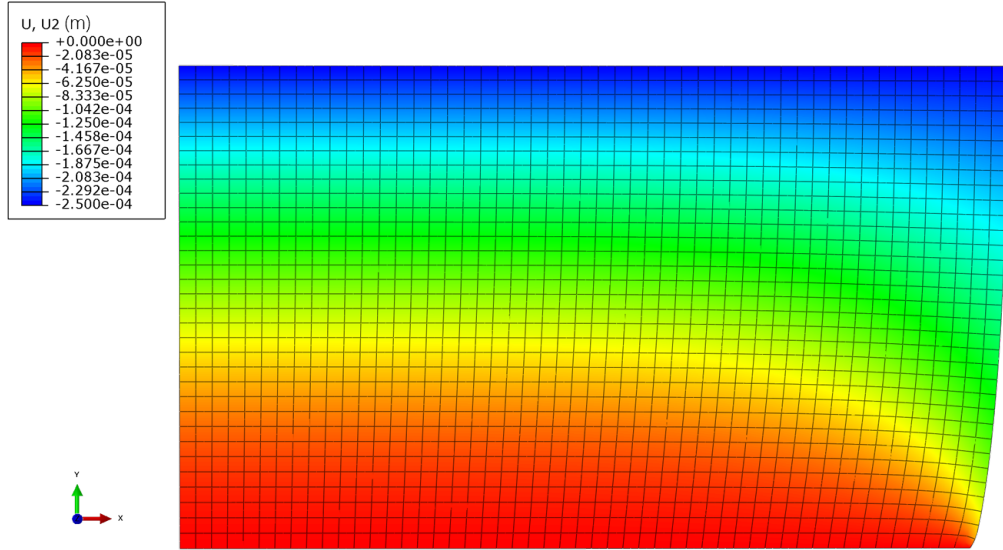
Figure 14: ABAQUS rendering of deformation and pore pressure in the cartilage plug
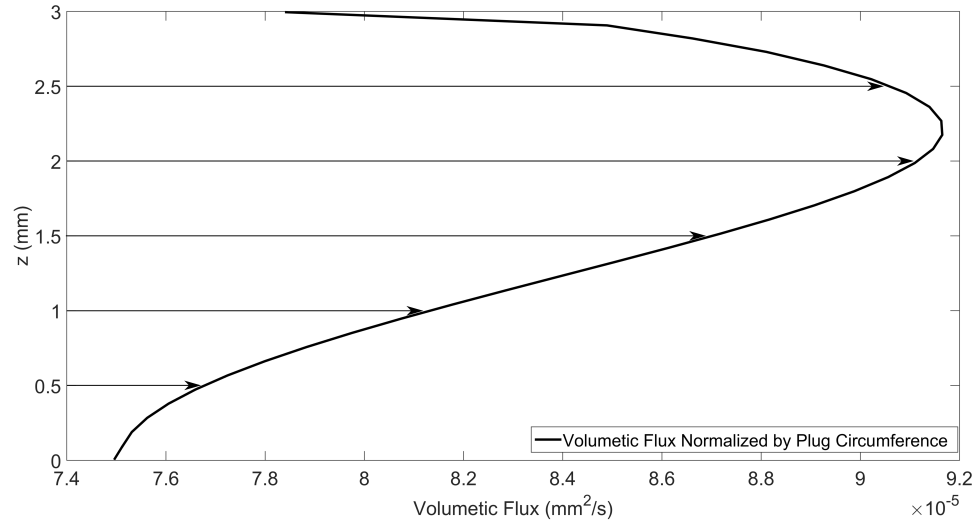
Figure 15: Volumetric flux across free boundary ($r = r_o$, $t = 30\ s$)
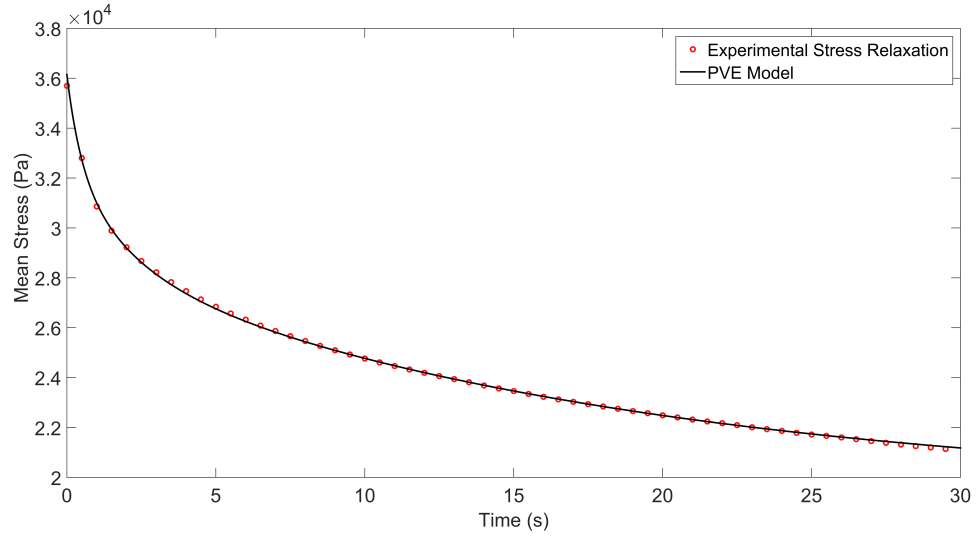
Figure 16: Comparison of PVE model to cartilage experiment in stress-relaxation

CHAPTER IV

SIMULATION OF FRACTIONAL CALCULUS VISCOELASTICITY

The principle of viscoelasticity was introduced in Chapter 3, and the advantages of fractional calculus model were discussed. What remains is to develop algorithms to model fractional calculus viscoelasticity in a time-dependent, displacement driven simulation. The ideal algorithm is accurate and expedient, regardless of the material's strain history. Mathematically, the problem is to solve the convolution integral:

$$\sigma\left(t\right) = \epsilon\left(0\right) E\left(t\right) + \int_0^t \dot{\epsilon}\left(\tau\right) E\left(t - \tau\right) \, \mathrm{d}\tau. \tag{1}$$

where the relaxation modulus, $E(t)$ is defined as the $n = 1$ CERF model (the fractional calculus counterpart to a Zener/Prony model [69]):

$$E(t) = E_0 + E_1 e^{\left(\mu_1^2 t\right)} erfc\left(\mu_1 \sqrt{t}\right), \tag{66}$$

The uniaxial case is used for development purposes, and is extended to three-dimensions when necessary.

In the following sections, five techniques to simulate fractional calculus viscoelasticity will be explored. Two techniques require the full strain history of a material, while the remaining three techniques use a limited strain history to expedite the simulation. The five techniques are summarized below:

 Full-length techniques

1. Convolution

2. Mechanical analogue

45

Expedited techniques

3. Truncated mechanical analogue

4. Fit with Prony series

5. Historic approximation with Prony series

4.1 Convolution

The traditional definition of a viscoelastic material involves the convolution integral. Two formulations based on superposition exist to relate stress and strain. These are given in Eqs. 1 and 2. The choice of independent variable dictates which equation to use. For displacement driven simulations (e.g. those performed with ABAQUS), the relaxation modulus is employed. In section 3.4, the CERF model was developed. A benefit of the CERF model is a simple time-domain representation. This is useful in determining model parameters from experimental data. The CERF relaxation modulus is placed directly in the convolution integral. Performing the integration gives precisely the stress. Unfortunately, the entire strain history is required in the convolution integral. For large-scale simulations, this is a computationally expensive model. Each integration point of each element must be tracked for the entire time history of the simulation. Not only does this represent a large storage burden, but evaluating the convolution integral is likewise computationally expensive. The benefit of this direct method is that the solution is exact according to the definition of viscoelasticity. For example, consider the step input of a relaxation test:

$$\epsilon(t) = \epsilon_0, \qquad t \geq t_0. \tag{67}$$

The solution is known for this case, as it is simply the relaxation modulus. The numerical method is verified from this known solution, as shown in Fig. 17. For different strain histories, convolution will be used as a baseline for comparison with the expedited methods developed herein.
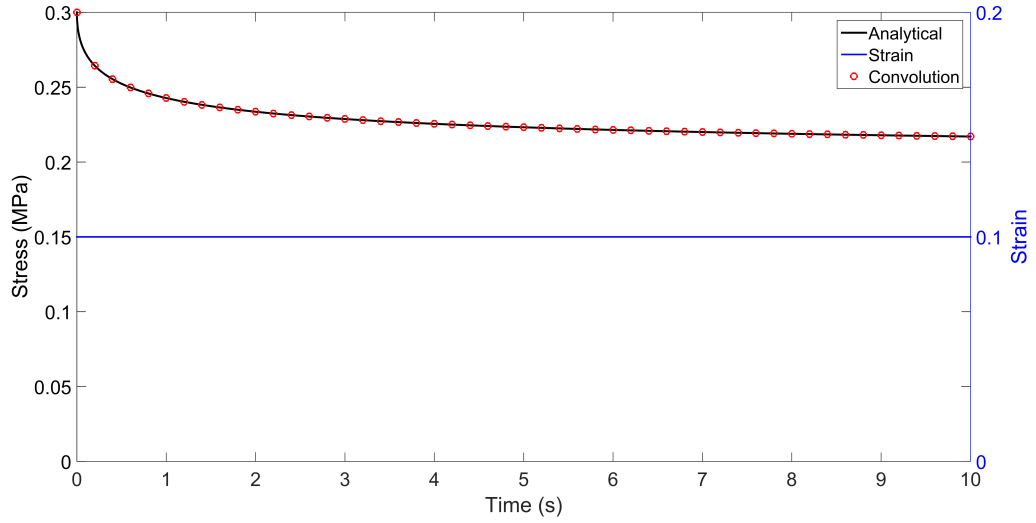
Figure 17: Verification of convolution integral and analytical stress relaxation

The storage requirement to evaluate the convolution integral cannot be circumvented. However, the convolution integral can be evaluated in an optimized way. Many numerical packages (e.g. Matlab) evaluate the full convolution integral, which has a length of $(2n-1)$ for a strain history with length (n). However, only the point at the forward time increment is needed; therefore, many unneeded calculations are performed with the convolution function. Either a user-written program or targeted use of built-in functions reduces the numerical cost. In Matlab for example, the convolution integral can be specified in the 'valid' region only. This returns a single value corresponding to the forward time step. The result is a more efficient algorithm for calculating the stress/strain relationship, and the answer is exact. However, the shortcoming is still simulation time and storage requirements, particularly for large (element wise) studies.

4.2   Mechanical analogue

A second method that uses the full time history is the mechanical analogue. Consider the fractional model shown in Fig. 4b. A differential equation relating stress, strain,

47

and the fractional derivative of stress and strain is constructed:

$$\left(1 + \frac{E_0}{E_1}\right)\frac{d^\alpha \epsilon_T}{dt^\alpha} + \frac{E_0}{\eta}\epsilon_T = \frac{1}{E_1}\frac{d^\alpha \sigma_T}{dt^\alpha} + \frac{1}{\eta}\sigma_T \tag{68}$$

To simulate this differential equation, numerical schemes (e.g. backward difference) are employed. Consider the backwards difference routine for a integer derivative:

$$\frac{d^n f(t)}{dt^n} = \lim_{N \to \infty}\left[\left(\frac{t}{N}\right)^{-n}\sum_{j=0}^{N-1}(-1)^j \binom{n}{j} f\left(t - j\frac{t}{N}\right)\right], \tag{69}$$

where $t/N = \Delta t$ and n is an integer. To evaluate non-integer derivatives, the bionomial coefficient must be expanded [92]:

$$(-1)^j \binom{\alpha}{j} = \frac{\Gamma(j - \alpha)}{\Gamma(-\alpha)\Gamma(j + 1)}. \tag{70}$$

Taking the Grűnwald-Letnikov (left-sided) definition of the fractional derivative, the fractional derivative is approximated using a backward difference scheme [92,93] where α has replaced n and is no longer required to be an integer. The only stipulation is that α exists as a real number. Substituting Eq. 70 in Eq. 69, the backwards difference fractional derivative is approximated:

$$\frac{d^\alpha f(t)}{dt^\alpha} \simeq \lim_{N \to \infty}\left[\left(\frac{t}{N}\right)^{-\alpha}\sum_{j=0}^{N-1}\frac{\Gamma(j - \alpha)}{\Gamma(-\alpha)\Gamma(j + 1)}f\left(t - j\frac{t}{N}\right)\right], \tag{71}$$

Defining the Grűnwald-Letnikov coefficient as:

$$A_{j+1} = \frac{\Gamma(j - \alpha)}{\Gamma(-\alpha)\Gamma(j + 1)}, \tag{72}$$

the recursive formula is obtained [93]:

$$A_{j+1} = \frac{j - 1 - \alpha}{j}A_j, \quad A_1 = 1. \tag{73}$$

Therefore, the numerical approximation of the Grűnwald-Letnikov fractional derivative is:

$$\frac{d^\alpha f(t)}{dt^\alpha} = \lim_{N \to \infty}\left[\left(\frac{t}{N}\right)^{-\alpha}\sum_{j=0}^{N-1}A_{j+1}f\left(t - j\frac{t}{N}\right)\right], \tag{74}$$

Note that to evalutate the fractional derivative, the entire history of the function is required. Evaluating the fractional derivatives in Eq. 68:

$$\frac{d^\alpha \sigma(t)}{dt^\alpha} \simeq \Delta t_{GL}^{-\alpha} \left[\sigma(t) + S_\sigma \right], \tag{75}$$

$$\frac{d^\alpha \epsilon(t)}{dt^\alpha} \simeq \Delta t_{GL}^{-\alpha} \left[\epsilon(t) + S_\epsilon \right], \tag{76}$$

where:

$$\Delta t_{GL} = \frac{t}{N}, \tag{77}$$

$$S_\sigma = \sum_{j=1}^{N_h-1} A_{j+1} \sigma \left(t - j \Delta t_{GL} \right), \tag{78}$$

$$S_\epsilon = \sum_{j=1}^{N_h-1} A_{j+1} \epsilon \left(t - j \Delta t_{GL} \right), \tag{79}$$

and $N_h = Int(t/\Delta t_{GL}) + 1$. Substituting Eqs. 75 and 76 into Eq. 68, the fractional differential equation is solved for stress at time t:

$$\left(1 + \frac{E_0}{E_1} \right) \Delta t_{GL}^{-\alpha} \left[\epsilon(t) + S_\epsilon \right] + \frac{E_0}{\eta} \epsilon(t) = \frac{1}{E_1} \Delta t_{GL}^{-\alpha} \left[\sigma(t) + S_\sigma \right] + \frac{1}{\eta} \sigma(t) \tag{80}$$

Equation 80 gives another method to evaluate the fractional calculus viscoelastic model, and in this case, the model is not limited to the constraints of the CERF model. Therefore, the fractional derivative can take any value between zero and one ($0 < \alpha < 1$). The mechanical analogue for $\alpha = 1/2$ is compared to the convolution integral for a stress relaxation and a sinusoidal strain history test, as shown in Figs. 18a and 18b, respectively. The mechanical analogue is clearly suitable for simulating fractional calculus viscoelasticity. However, the numerical simulation has the same limitations as the convolution method: namely the storage requirements are expensive for large element models and long simulations.

The two methods described above are suitable for small-scale simulation where modeling accuracy is critically important. The trade-off is that the storage and calculation requirements are cumbersome. To alleviate some of the computational

expense, three methods are proposed. Each method represents an approximation of the fractional calculus model.

4.2.1 Truncated mechanical analogue

To expedite the numerical process, the first method is a reduction of the aforementioned fractional differential equation. Recall that Eq. 74 evaluates the fractional derivative by considering the entire history of the function $f(t)$. By recognizing that $0 < \alpha < 1$, the Grűnwald-Letnikov coefficient has a fading memory behavior [92]. This is depicted in Fig. 19, and can be used to expedite the simulation by truncating the summation in Eqs. 78 and 79. Therefore, only the most recent historical information is used. Figure 19 shows vector A_j for a representative sample. Clearly, the recent history is most important for the evaluation of the fractional derivative, and as j increases, the fading memory contributes less to the response. By retaining a limited history of the most recent values, the computation burden of the fractional derivative is reduced. The length of history that must be stored depends on the strain itself and the desired accuracy of the solution. Examples of varying accuracy and strain types are provided in Figs. 20a and 20b, based on the percentage of the strain history stored.

The method proposed to evaluate the fractional differential equation is a hybrid method that reduces the full computation burden of evaluating the fractional derivative. However, a significant amount of information must still be stored with this technique. One advantage is that the storage space is pre-allocated based on the desired length of history. A disadvantage is that the error tolerance is not known *a priori*, and depends on the strain history itself.

The three methods discussed to this point require significant storage space, and are computationally handicapped because of the number of file calls that must be made at each iteration in time. Two methods that do not require the same storage
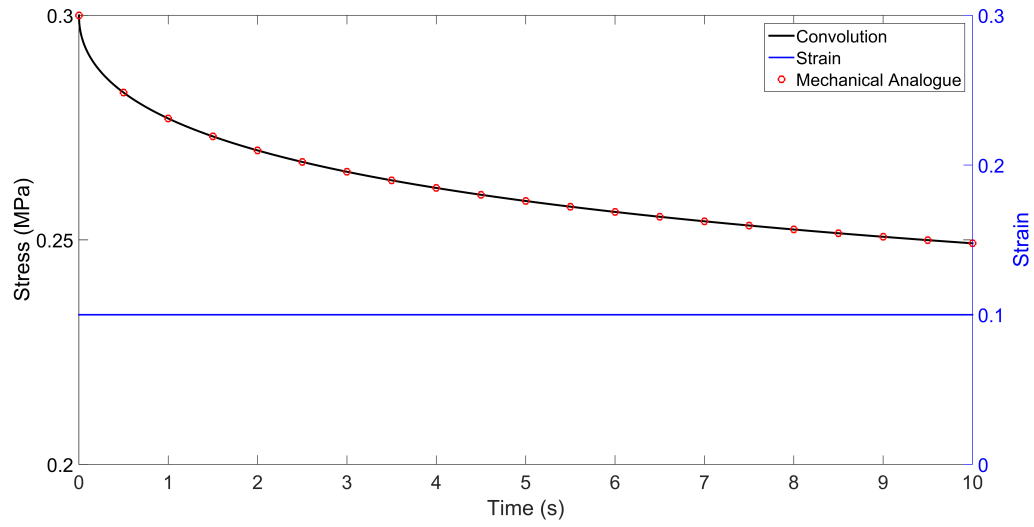
(a) Stress relaxation
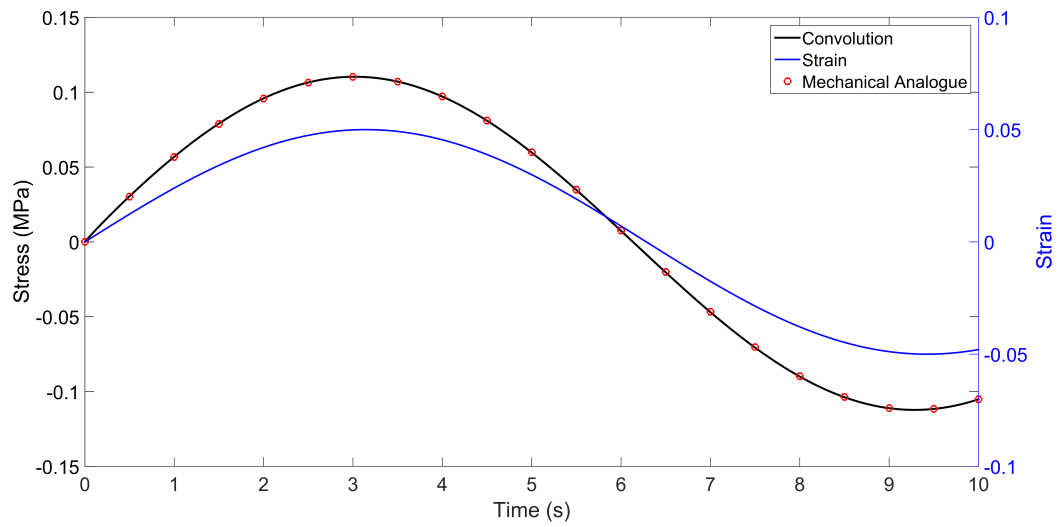
(b) Sinusoidal stress

Figure 18: Comparison of full-history models
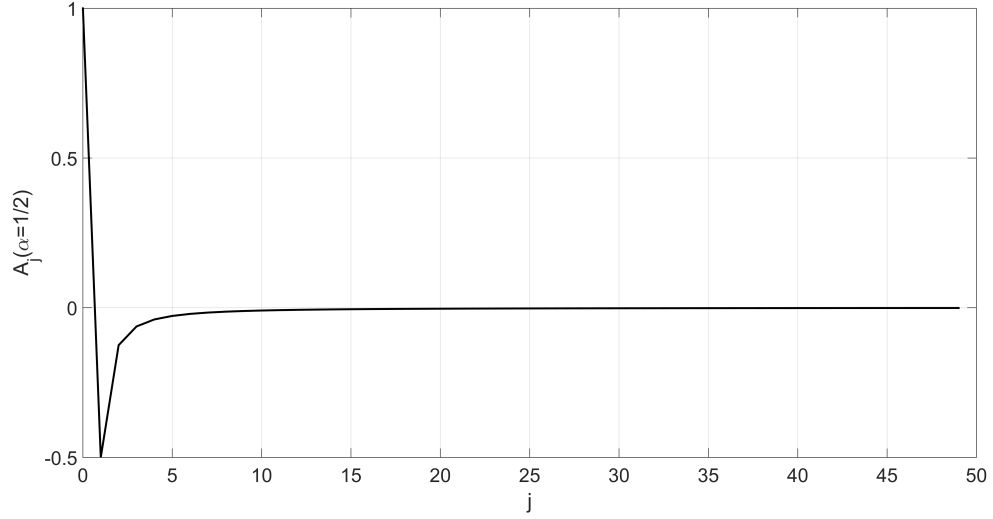
Figure 19: A_j visualized vectorially to show fading memory principle

requirements are presented next. Each utilizes integer-order derivatives to approximate fractional calculus derivatives.

4.3   Fit with Prony series

The fractional calculus viscoelastic models are often used in modeling applications because they require fewer terms to accurately characterize material behavior. Unfortunately, fractional calculus, unlike integer-order calculus, is strongly historic in numerical applications. While this proves to be advantageous for modeling viscoelasticity (as it has a historic component), fractional calculus is very computationally expensive to simulate in finite element models. Therefore, a technique that is employed to approximate fractional calculus VE models is to replace them with high fidelity integer order models. For example, the one-term CERF model is fit with a four term Prony series. The fit is shown in Fig. 21. The proposed approximation blends the advantages of both fractional and integer-order calculus. For example, the one-term fractional calculus model is completely smooth in the frequency domain [2], while the Prony series is portable in FEA simulations. The consequence of approximating a
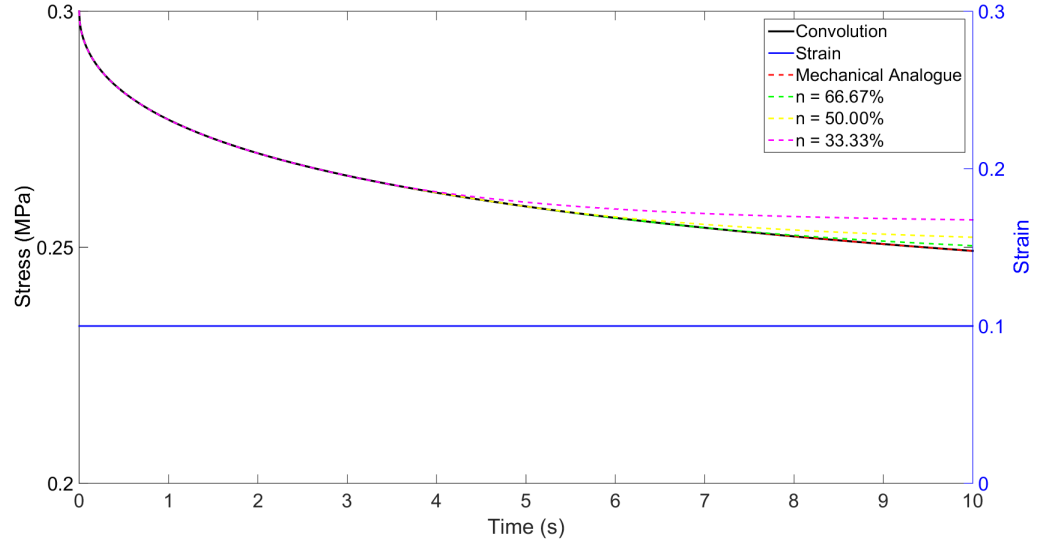
(a) Stress relaxation comparing truncated mechanical analogues
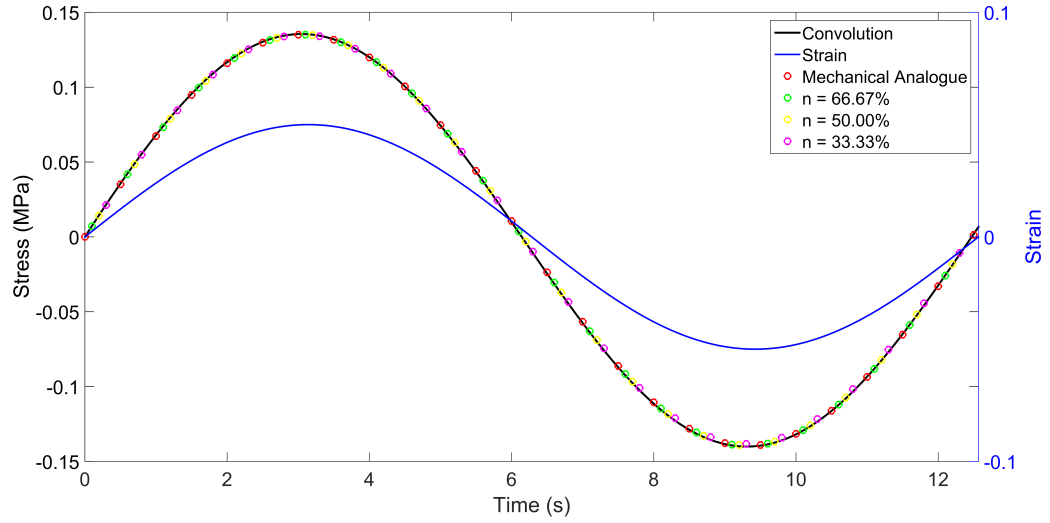
(b) Sinusoidal strain input comparing truncated mechanical analogues

Figure 20: Comparison of truncated mechanical analogue models
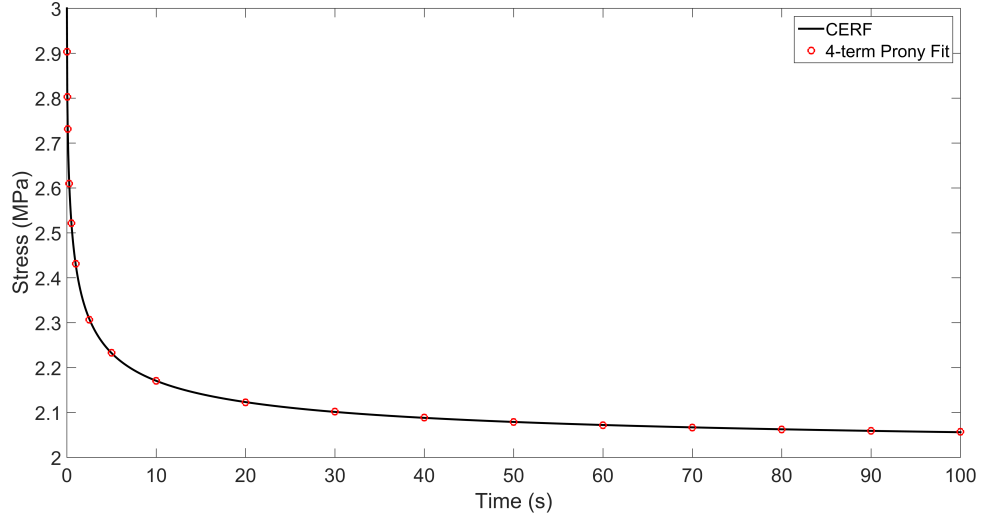
Figure 21: CERF relaxation fit with 4-term Prony series

fractional calculus model with a integer-order model is that additional complexity is introduced on the front end of a simulation.

If the fractional calculus model is approximated with a Prony series, simulation of the material behavior does not require historic information beyond state variables that describe the current time step. Consider the aforementioned convolution definition of a viscoelastic material (uniaxial):

$$\sigma\left(t\right) = \epsilon\left(0\right) E\left(t\right) + \int_0^t \dot{\epsilon}\left(\tau\right) E\left(t - \tau\right) \, \mathrm{d}\tau. \tag{1}$$

If causality is assumed, $\epsilon(t \leq 0) = 0$, Eq. 1 becomes:

$$\sigma\left(t\right) = \int_0^t \dot{\epsilon}\left(\tau\right) E\left(t - \tau\right) \, \mathrm{d}\tau. \tag{81}$$

Recalling the Prony series (Eq. 11), the stress is rewritten as:

$$\sigma\left(t\right) = E_T \left[\epsilon\left(t\right) - \sum_{n=1}^{\infty} \gamma_n \epsilon_n\left(t\right)\right], \tag{82}$$

where

$$E_T = E_0 + \sum_{n=1}^{\infty} E_n \tag{83}$$

54

and

$$\gamma_n = E_n/E_t. \tag{84}$$

The viscous strain is defined as [87]:

$$\epsilon_n (t) = \int_0^t \left[1 - e^{-\lambda_n(t-\tau)}\right] \dot{\epsilon}(\tau) \, d\tau. \tag{85}$$

For the forward time increment, Eq. 82 is defined as:

$$\sigma (t + \Delta t) = E_T \epsilon (t + \Delta t) - \sum_{n=1}^{\infty} E_n \epsilon_n (t + \Delta t), \tag{86}$$

and the viscous strain (Eq. 85) becomes:

$$\epsilon_n (t + \Delta t) = \int_0^{t+\Delta t} \left[1 - e^{-\lambda_n(t+\Delta t - \tau)}\right] \dot{\epsilon}(\tau) \, d\tau. \tag{87}$$

The integral in Eq. 87 is split into two parts:

$$\epsilon_n (t + \Delta t) = \int_0^t \left[1 - e^{-\lambda_n(t+\Delta t - \tau)}\right] \dot{\epsilon}(\tau) \, d\tau + \int_t^{t+\Delta t} \left[1 - e^{-\lambda_n(t+\Delta t - \tau)}\right] \dot{\epsilon}(\tau) \, d\tau. \tag{88}$$

The preceding equation now has two components: one that accounts for historic effects, and one that considers the forward time increment. Considering the forward integral, a fundamental assumption is made that the strain over the increment $\Delta\tau$ is small enough to be approximated as linear:

$$\dot{\epsilon}(\tau) = \frac{d\epsilon}{d\tau} = \frac{\Delta\epsilon}{\Delta\tau}. \tag{89}$$

where

$$\Delta\epsilon = \epsilon(t + \Delta t) - \epsilon(t). \tag{90}$$

Therefore, $\dot{\epsilon}(\tau)$ can be pulled out of the forward time integral

$$\epsilon_n (t + \Delta t) = \int_0^t \left[1 - e^{-\lambda_n(t+\Delta t - \tau)}\right] \dot{\epsilon}(\tau) \, d\tau$$
$$+ \frac{\Delta\epsilon}{\Delta t} \int_t^{t+\Delta t} \left[1 - e^{-\lambda_n(t+\Delta t - \tau)}\right] \, d\tau. \tag{91}$$

The second integral is now readily evaluated:

$$
\epsilon_n \left(t + \Delta t \right) = \int_0^t \left[1 - e^{-\lambda_n (t + \Delta t - \tau)} \right] \dot{\epsilon} \left(\tau \right) \, \mathrm{d}\tau
$$
$$
+ \frac{\Delta \epsilon}{\Delta t} \left(\Delta t - \frac{1}{\lambda_n} + \frac{e^{-\lambda_n \Delta t}}{\lambda_n} \right). \tag{92}
$$

The properties of exponentials allow for the expedient evaluation of the first integral as well:

$$
\epsilon_n \left(t + \Delta t \right) = \epsilon(t) - \int_0^t \left[e^{-\lambda_n \Delta t} e^{-\lambda_n (t - \tau)} \right] \dot{\epsilon} \left(\tau \right) \, \mathrm{d}\tau
$$
$$
+ \frac{\Delta \epsilon}{\Delta t} \left(\Delta t - \frac{1}{\lambda_n} + \frac{e^{-\lambda_n \Delta t}}{\lambda_n} \right). \tag{93}
$$

Pulling the exponential out gives:

$$
\epsilon_n \left(t + \Delta t \right) = \epsilon(t) - e^{-\lambda_n \Delta t} \int_0^t \left[e^{-\lambda_n (t - \tau)} \right] \dot{\epsilon} \left(\tau \right) \, \mathrm{d}\tau
$$
$$
+ \frac{\Delta \epsilon}{\Delta t} \left(\Delta t - \frac{1}{\lambda_n} + \frac{e^{-\lambda_n \Delta t}}{\lambda_n} \right). \tag{94}
$$

The remaining integral term shares similarities with Eq. 85, which is used to remove the integral (significantly reducing the computationally expensive portion of the simulation):

$$
\epsilon_n \left(t + \Delta t \right) = \epsilon(t) - e^{-\lambda_n \Delta t} \left(\epsilon_n(t) - \epsilon(t) \right)
$$
$$
+ \frac{\Delta \epsilon}{\Delta t} \left(\Delta t - \frac{1}{\lambda_n} + \frac{e^{-\lambda_n \Delta t}}{\lambda_n} \right). \tag{95}
$$

After some rearranging and algebra, the forward increment of viscous strain is:

$$
\epsilon_n \left(t + \Delta t \right) = \left(1 + e^{-\lambda_n \Delta t} \right) \epsilon(t) - e^{-\lambda_n \Delta t} \epsilon_n(t)
$$
$$
+ \frac{\Delta \epsilon}{\lambda_n \Delta t} \left(e^{-\lambda_n \Delta t} - 1 \right) + \Delta \epsilon, \tag{96}
$$

$$
\epsilon \left(t + \Delta t \right) = \epsilon(t) + \Delta \epsilon. \tag{97}
$$

Equations 96 and 97 are in terms of known quantities. Therefore, the stress (Eq. 86) is determined. The viscous strain, $\epsilon_n(t)$, must be stored for each n, corresponding to

Table 3: Fit parameters of Prony series to CERF model

	CERF	Prony
E_0	2.0 MPa	2.0502 MPa
E_1	1.0 MPa	0.1977 MPa
E_2	-	0.2507 MPa
E_3	-	0.2844 MPa
E_4	-	0.1204 MPa
$\mu_1|\lambda_1$	1.0 $s^{-1/2}$	0.1884 s^{-1}
λ_2	-	8.1853 s^{-1}
λ_3	-	1.0453 s^{-1}
λ_4	-	0.0286 s^{-1}

each Maxwell element in the Prony series. These state variables are the only storage requirement to determine the forward stress increment.

The properties of exponentials are fundamental in evaluating the $t + \Delta t$ relationship. The unique nature of exponentials makes the Prony series ideal for time stepping algorithms. The fundamental assumption that strain is linear over the Δt increment is critical to the execution of the algorithm. The validity of that assumption must be ascertained as the simulation is performed.

The advantage of the Prony series representation is apparent in simulation speed. Therefore, approximating the CERF model with a four-term Prony series is a viable option for the numerical simulation of a viscoelastic material. Returning to the fit shown in Fig. 21, the Prony series constants are determined. These properties are given in Table 3. The four-term Prony series is compared to the CERF model (determined by full convolution) in Figs. 22a and 22b. Figure 22a shows the Prony series in stress relaxation, and Fig. 22b shows a sinusoidal strain. The Prony fit can be used when simulation efficiency is paramount.
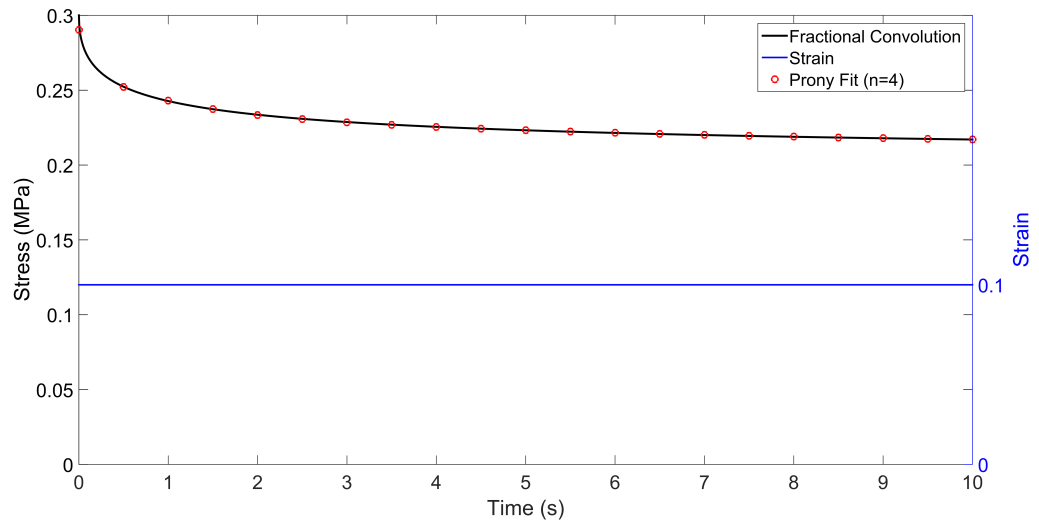
(a) Stress relaxation
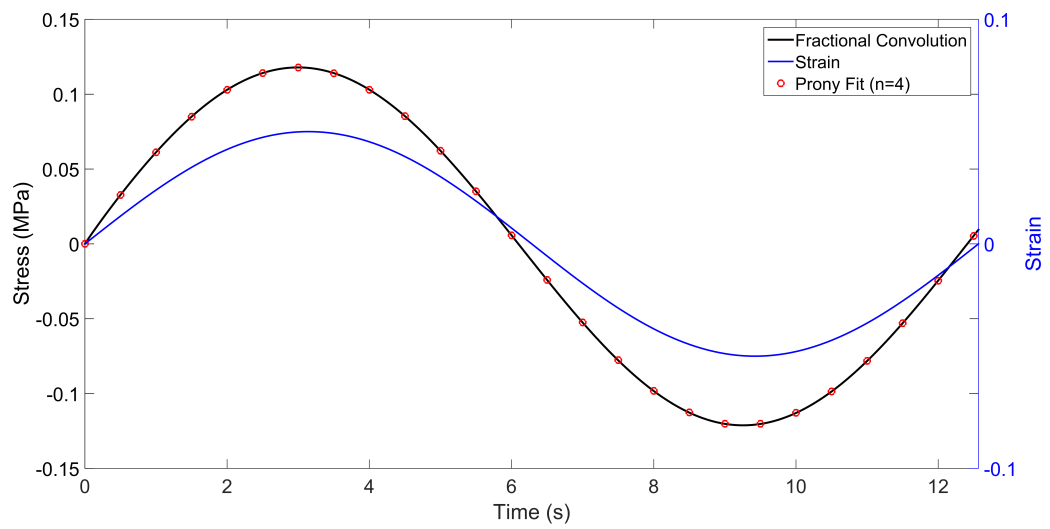
(b) Sinusoidal stress

Figure 22: Comparison of fractional and Prony fit (n=4)

4.4   Historic approximation with Prony series

The algorithm developed for the Prony series is extended to the CERF model. The definition of viscous strain changes to:

$$\epsilon_n\left(t\right) = \int_0^t \left[1 - e^{\mu_n^2(t-\tau)} erfc(\mu_n\sqrt{t-\tau})\right]\dot{\epsilon}\left(\tau\right)\,\mathrm{d}\tau. \tag{98}$$

The forward time increment of Eq. 98 is:

$$\epsilon_n\left(t + \Delta t\right) = \int_0^{t+\Delta t} \left[1 - e^{\mu_n^2(t+\Delta t-\tau)} erfc(\mu_n\sqrt{t+\Delta t-\tau})\right]\dot{\epsilon}\left(\tau\right)\,\mathrm{d}\tau. \tag{99}$$

Following the process used for the Prony series, the integral is split and a linear strain increment is assumed:

$$\epsilon_n\left(t + \Delta t\right) = \int_0^{t} \left[1 - e^{\mu_n^2(t+\Delta t-\tau)} erfc(\mu_n\sqrt{t+\Delta t-\tau})\right]\dot{\epsilon}\left(\tau\right)\,\mathrm{d}\tau$$
$$+ \frac{\Delta\epsilon}{\Delta t}\int_t^{t+\Delta t} \left[1 - e^{\mu_n^2(t+\Delta t-\tau)} erfc(\mu_n\sqrt{t+\Delta t-\tau})\right]\,\mathrm{d}\tau. \tag{100}$$

The second integral is evaluated analytically:

$$\epsilon_n\left(t + \Delta t\right) = \int_0^{t} \left[1 - e^{\mu_n^2(t+\Delta t-\tau)} erfc(\mu_n\sqrt{t+\Delta t-\tau})\right]\dot{\epsilon}\left(\tau\right)\,\mathrm{d}\tau$$
$$+ \frac{\Delta\epsilon}{\mu_n^2\Delta t}\left[1 - e^{\mu_n^2(\Delta t)} erfc(\mu_n\sqrt{\Delta t}) - \frac{2\mu_n\sqrt{\Delta t}}{\sqrt{\pi}}\right]. \tag{101}$$

The problem that arises is that the first integral cannot utilize the same expedient properties of exponentials that the Prony model uses. Namely, the $(t + \Delta t)$ term cannot be split up. Therefore, the integral must either be evaluated in full (which is essentially a convolution operation), or approximated. It is desired to expedite the simulation by using state variables, as was done for the viscous strain term in the Prony model. One technique that seemingly supports this is to expand the first integral about time t. A Taylor series is performed on the integral expression in

Eq. 101, truncating terms with order equal or higher than $(\Delta t)^2$

$$\int_0^t \left[1 - e^{\mu_n^2(t+\Delta t - \tau)} erfc(\mu_n\sqrt{t + \Delta t - \tau})\right] \dot\epsilon(\tau) \, \mathrm{d}\tau \approx$$

$$\int_0^t \left[1 - e^{\mu_n^2(t-\tau)} erfc(\mu_n\sqrt{t - \tau})\right] \dot\epsilon(\tau) \, \mathrm{d}\tau$$

$$+ \int_0^t \left[\Delta t \left(\frac{\mu_n}{\sqrt\pi\sqrt{t - \tau}} - \mu_n^2 e^{\mu_n^2(t-\tau)} erfc(\mu_n\sqrt{t - \tau})\right)\right] \dot\epsilon(\tau) \, \mathrm{d}\tau. \tag{102}$$

Simplifying:

$$\int_0^t \left[1 - e^{\mu_n^2(t+\Delta t - \tau)} erfc(\mu_n\sqrt{t + \Delta t - \tau})\right] \dot\epsilon(\tau) \, \mathrm{d}\tau \approx$$

$$\left(1 + \Delta t \mu^2\right)\left(\epsilon_n(t) - \epsilon(t)\right) + \epsilon(t) + \int_0^t \left[\Delta t \left(\frac{\mu_n}{\sqrt\pi\sqrt{t - \tau}}\right)\right] \dot\epsilon(\tau) \, \mathrm{d}\tau. \tag{103}$$

Therefore, returning to the viscous strain at the forward increment:

$$\epsilon_n(t + \Delta t) = \epsilon(t) + \left(1 + \Delta t \mu^2\right)\left(\epsilon_n(t) - \epsilon(t)\right) + \int_0^t \left[\Delta t \left(\frac{\mu_n}{\sqrt\pi\sqrt{t - \tau}}\right)\right] \dot\epsilon(\tau) \, \mathrm{d}\tau$$

$$+ \frac{\Delta\epsilon}{\mu_n^2 \Delta t}\left[1 - e^{\mu_n^2(\Delta t)} erfc(\mu_n\sqrt{\Delta t}) - \frac{2\mu_n\sqrt{\Delta t}}{\sqrt\pi}\right],$$

$$\tag{104}$$

$$\epsilon(t + \Delta t) = \epsilon(t) + \Delta\epsilon. \tag{105}$$

Equation 104 highlights a challenge associated with the CERF model. That is, there is a singularity in the derivative of the CERF model at $t = \tau$. If performing the entire convolution routine, this singularity can be handled, but the desire is to avoid a full convolution operation. The technique for simulating the viscous strain in the Prony series is not applicable for the CERF model. Therefore, another approach must be taken. Some techniques that were considered to remedy this problem include: approximation of the $erfc$ as an exponential series, integration by parts on the term with a singularity, and replacing the singularity with a delta dirac function and evaluating analytically. Unfortunately, each of these methods accumulates significant error as time progresses.

The singularity in Eq. 104 occurs when $\tau = t$. When evaluating the integral, it is clear that the singularity occurs at the most recent time history point. Therefore, the most important historical point is also the most troublesome point. A proposed remedy around the singular point is to approximate the historic component with a Prony model. In Eq. 100, the historic component is replaced with a Prony series, while the forward strain increment is retained as the CERF component. Using a known viscoelastic model ensures thermodynamic consistency, and allows for use of the convenient properties of the Prony series. Mathematically, $\epsilon_n(t + \Delta t)$ becomes:

$$
\begin{aligned}
\epsilon_n (t + \Delta t) = \left(1 + e^{-\lambda_n \Delta t}\right) \epsilon(t) - e^{-\lambda_n \Delta t} \epsilon_n(t) \\
+ \frac{\Delta \epsilon}{\mu_n^2 \Delta t} \left[1 - e^{\mu_n^2 (\Delta t)} erfc(\mu_n \sqrt{\Delta t}) - \frac{2\mu_n \sqrt{\Delta t}}{\sqrt{\pi}}\right].
\end{aligned}
\tag{106}
$$

The stress relaxation behavior of the hybrid model is compared to the fractional model in Fig. 23a. The hybrid model clearly deviates from the fractional model in stress relaxation. This is not surprising considering that stress relaxation negates the forward term (the second term of Eq. 101) because the change in strain is zero, $\Delta \epsilon = 0$. Therefore, the hybrid model becomes identically the one-term Prony model. However, considering a more realistic strain profile, like that shown in Fig. 23b, the hybrid model tracks the fractional model realistically. This indicates that the forward strain increment is the more important component of the stress calculation. The advantage of the hybrid model is that the storage requirement is exactly the same as the one-term Prony model, but it approximates fractional viscoelasticity. This represents a progressive step forward for the expedient simulation of fractional calculus viscoelasticity. However, the trade-off is that fidelity is lost with the hybrid model, and that up-front effort is expended to fit the correct Prony model to the desired fractional model. If the utility of simulation speed is paramount, the hybrid model is a viable option.
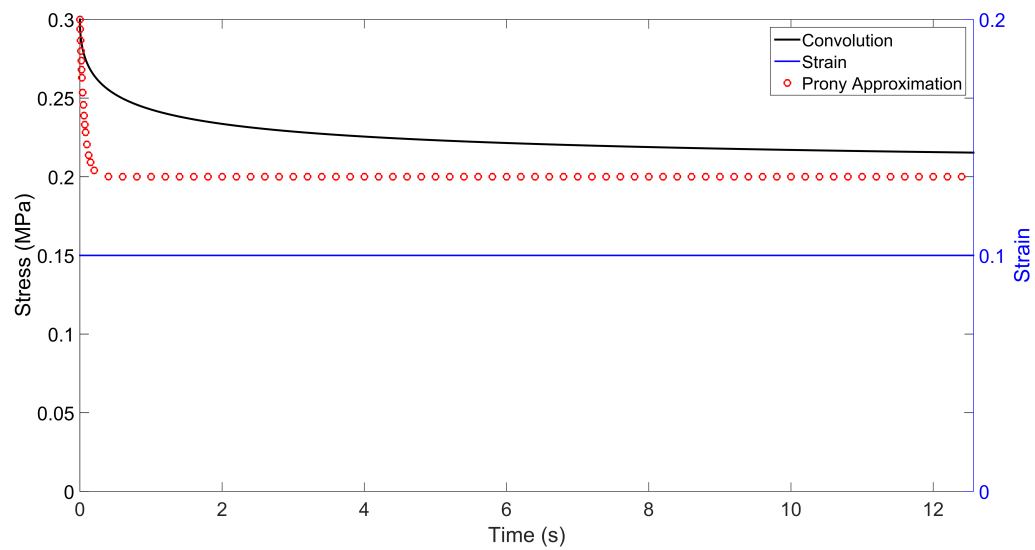
(a) Stress relaxation
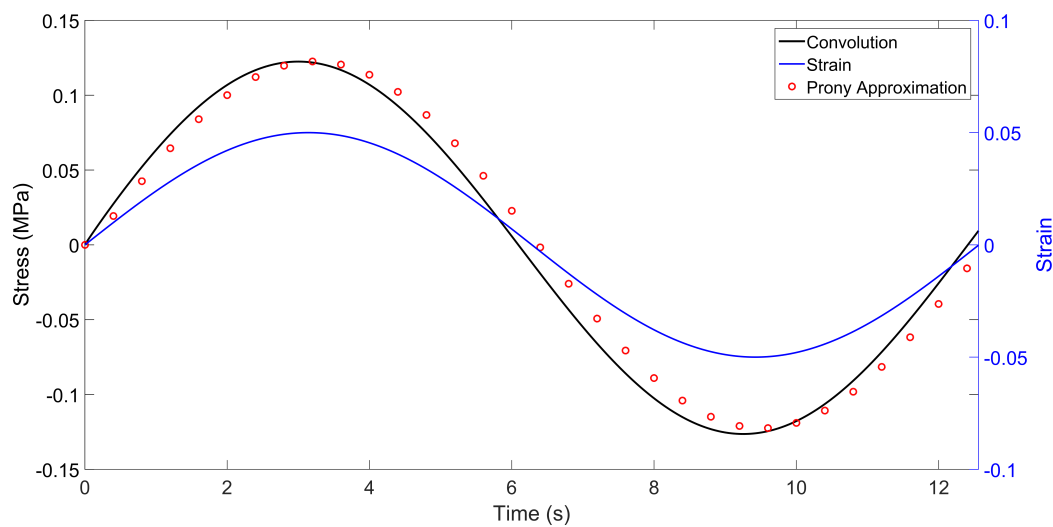
(b) Sinusoidal stress

Figure 23: Comparison of fractional and historic Prony fit

Table 4: Comparison of simulation techniques and simulation times

	Simulation Time (s)	Eff. (%)	Max Error Relative to Max Stress (%)
Full convolution	426.0 (s)	-	-
Mechanical analogue	199.6 (s)	53 (%)	0.69%
Truncated mechanical (n=50%)	136.0 (s)	68 (%)	0.73%
Fit with Prony series	3.1 (s)	99 (%)	0.09%
Historic approx. with Prony	3.0 (s)	99 (%)	14.3%

4.4.1 Summary

A number of algorithms are presented for the simulation of a fractional calculus viscoelastic model. A clear trade-off exists between model fidelity and simulation time. The five techniques discussed are compared side-by-side in Table 4. Each technique was simulated on the same machine 30 times and the simulation time was averaged. The efficiency metric is determined relative to the full convolution simulation (e.g. there is a 99% reduction in simulation time between the full convolution and the Prony series fit).

The specifics of the finite element analysis will determine which model is appropriate; however, a number of options are available. During the development of the aforementioned algorithms, a number of additional methods were considered. These include: exponential expansion of the CERF function, Guyan reduction to eliminate certain degrees of freedom, series expansions, representation of fractional calculus with smooth functions (to avoid the singularity present in the CERF), and approximation of the fractional derivative with integer-order derivatives, among others. Such techniques should be explored if the proposed models do not meet speed and accuracy thresholds determined from the displacement driven simulations. The threshold depends on the problem being solved, and likely cannot be accessed *a priori*. Therefore,

the end user must remain aware of the requirements of each simulation.

Fractional calculus is employed in the current work because it provides a succinct characterization of viscoelasticity, particularly in the frequency domain. The routine used to model fractional calculus in the time-domain should likewise be efficient. Fitting the fractional model with a four-term Prony series accomplishes this goal, and has the additional benefit of being supported by ABAQUS. Therefore, a separate user material file is not written. In the following section, the CERF viscoelastic model is verified in ABAQUS, and compared to the analytical solution obtained from evaluating the full convolution integral.

4.5 Validation of Viscoelastic Models in FEA

The aforementioned methods to simulate viscoelasticity are validated in FEA by testing single-element models. A single-element model is directly compared to available analytical solutions. Three tests are performed: stress relaxation, creep, and sinusoidal strain control. The first validation is for the Prony series, which is supported by ABAQUS. The fractional model (unsupported) follows.

4.5.1 Prony

ABAQUS has built-in functionality for viscoelasticity in its material library. All supported elements can be described by the Prony series. However, manipulation of the constitutive equations is necessary to conform to the requirements of ABAQUS. Table 5 gives the parameter conversion from the constitutive model to that of ABAQUS. The mechanics are governed by the elastic modulus and Poisson's ratio, and the shear and bulk modulus ratios and time constant. The uniaxial case is considered to isolate the stress/strain relationship.

Stress relaxation and creep are useful for validation because the relaxation and creep moduli are known analytically in the one-term Prony series:

Table 5: Input parameters for Prony validation in ABAQUS

	Symbol	Value (units)
Free spring Prony term	E_0	0.667 (MPa)
Maxwell spring Prony term	E_1	0.333 (MPa)
Prony time term	λ	0.5 ($1/s$)
Free spring Prony term	J_0	1 ($1/MPa$)
Maxwell spring Prony term	J_1	0.5 ($1/MPa$)
Prony time term	τ	3 (s)
Instantaneous elastic modulus	E_i	1.00 (MPa)
Instantaneous Poisson's ratio	ν	0.30
Prony constant (bulk)	k_1	0.33
Prony constant (shear)	g_1	0.33
Time constant	τ_1	2 (s)

$$E(t) = E_0 + E_1 e^{-\lambda t}, \tag{107}$$

$$J(t) = J_0 + J_1 \left(1 - e^{-t/\tau}\right). \tag{108}$$

Fixing the respective independent variable leads to simple expressions for the stress/strain relationship:

$$\sigma(t) = \left(E_0 + E_1 e^{-\lambda t}\right) \epsilon_0, \tag{109}$$

$$\epsilon(t) = \left[J_0 + J_1 \left(1 - e^{-t/\tau}\right)\right] \sigma_0. \tag{110}$$

In ABAQUS, stress relaxation is formed by applying a fixed displacement boundary condition in time, and tracking the resulting stress. Creep is determined from a fixed stress (or pressure) in time, and tracking the resulting strain. The results of this are shown in comparison to the analytical results in Fig. 24. The results clearly indicate agreement between the single element test in FEA and the analytical solution. A sinusoidal strain pattern is also tested for completeness, as shown in Fig. 25. Here, the analytical solution is formed by taking the convolution of the relaxation modulus and the rate of change of strain. Once again, the FEA simulation tracks the analytical identically. The results of the single element tests indicate that ABAQUS accurately

Table 6: Input parameters for ABAQUS

	Symbol	Value (units)
Element type		C3D8R
Instantaneous elastic modulus	E_i	2.903 (MPa)
Instantaneous Poisson's ratio	ν	0.3
Prony constant (bulk)	k_1	0.0681
	k_2	0.0863
	k_3	0.0980
	k_4	0.0415
Prony constant (shear)	g_1	0.0681
	g_2	0.0863
	g_3	0.0980
	g_4	0.0415
Time constant	τ_1	5.3079 (s)
	τ_2	0.1222 (s)
	τ_3	0.9567 (s)
	τ_4	34.9650 (s)

represents linear viscoelastic behavior described by the Prony series. This allows for a more complicated viscoelastic model to be built.

4.5.2 Complementary Error Function Model

The same tests used to validate the one-term Prony series are used for the CERF model. The CERF model is constructed from a best fit (in a least squares sense) four-term Prony series (refer to Table 3 for fit coefficients). These values are sent to ABAQUS in the manner discussed in Table 6. The four-term Prony series is an approximation of the CERF model, but is compared to the full CERF model in stress relaxation, creep, and sinusoidal strain. Figure 26 shows the stress relaxation and creep comparison. The stress relaxation result is analytical based on the relaxation modulus. Unlike the one-term Prony series, the CERF model does not have an elegant creep modulus. Therefore, the creep data is converted from the stress relaxation data using interconversion, discussed herein. In both creep and stress relaxation, the CERF approximation (simulated by ABAQUS) has qualitative and quantitative agreement
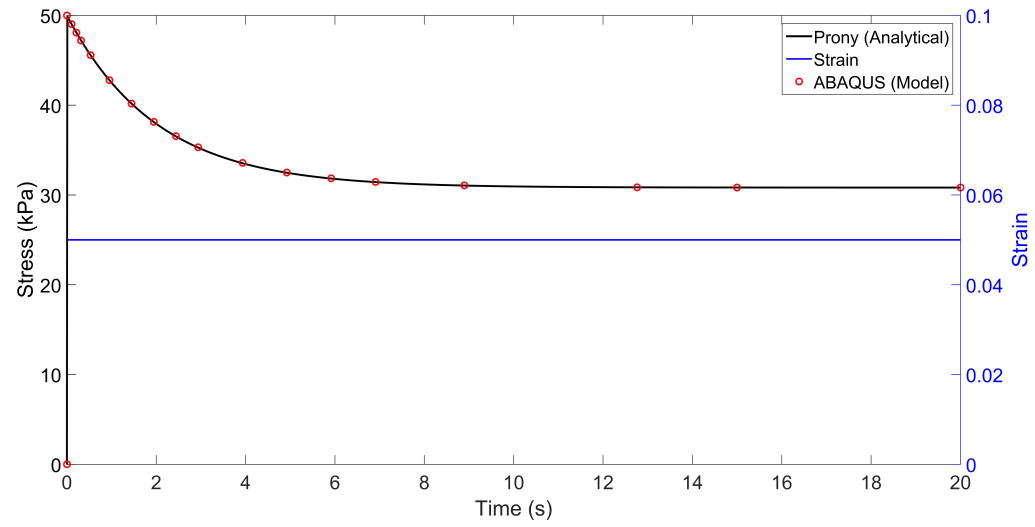
(a) Stress relaxation
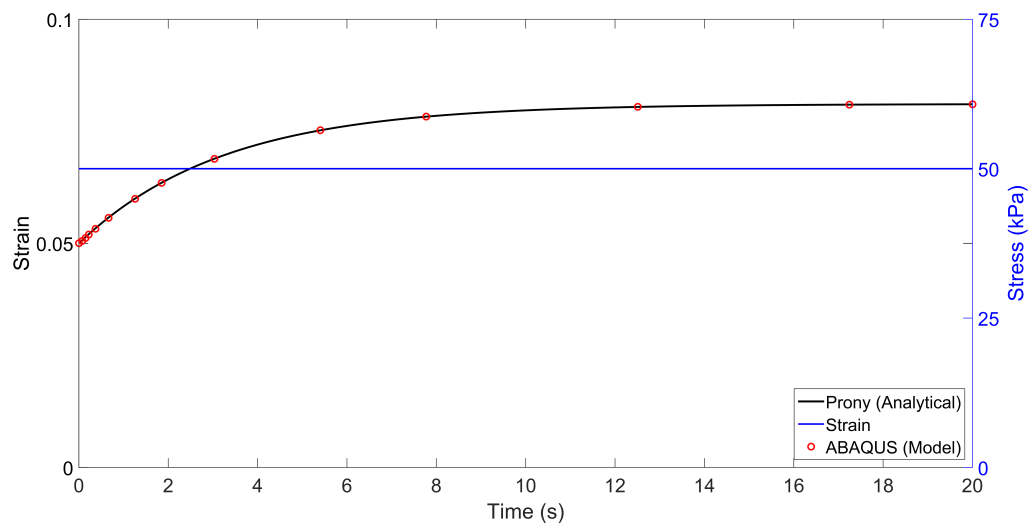
(b) Creep

Figure 24: Stress relaxation and creep validation of Prony viscoelastic model in ABAQUS
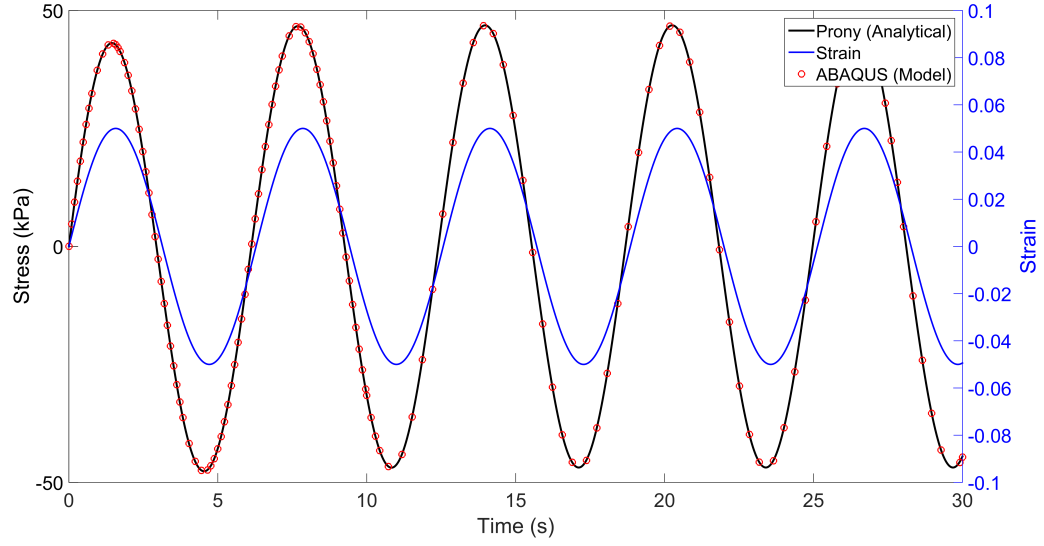
Figure 25: Validation of Prony viscoelastic model in ABAQUS from sinusoidal strain input

with the analytical solution. The sinusoidal strain case shows similar quality of fit, as seen in Fig. 27.

ABAQUS uses the techniques discussed in Section 4.3 to simulate viscoelastic behavior. The validation indicates that the ABAQUS results are consistent with the full, analytical solution. Therefore, the current study will use a Prony fit of the CERF model to simulate the time-domain behavior of viscoelastic materials. The viscoelastic model is included in the poroviscoelastic formulation of the substrate material.

4.5.3 Interconversion

The viscoelastic models presented in Chapter 3 are employed as constitutive models to characterize the storage and loss of the coupled HDL/PVE simulation. The Prony series and CERF models are well-defined in the time and frequency domains, with analytical expressions for the storage and loss moduli based on the time-domain fit of the simulation data. The disadvantage of using the Prony series and CERF models is
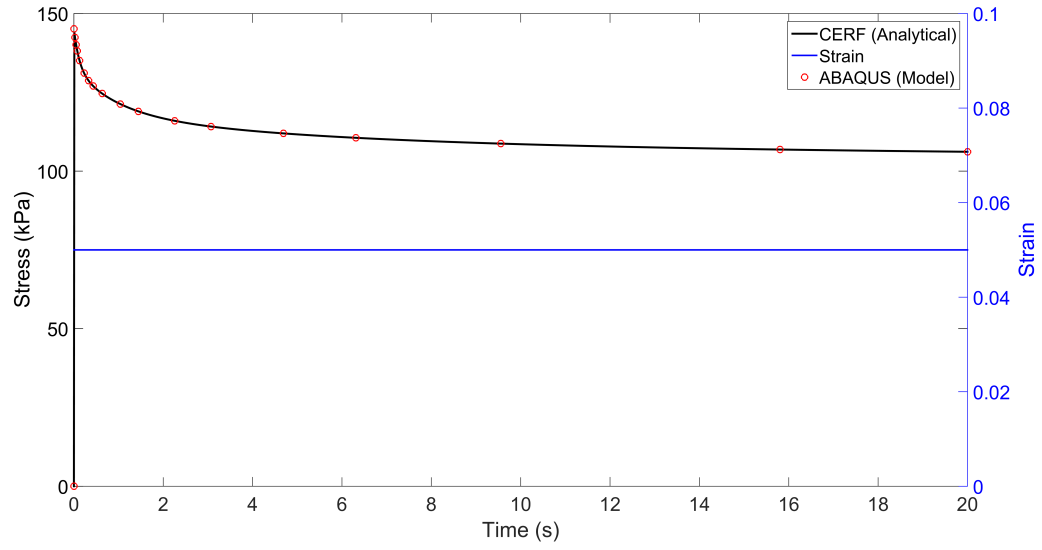
(a) Stress relaxation
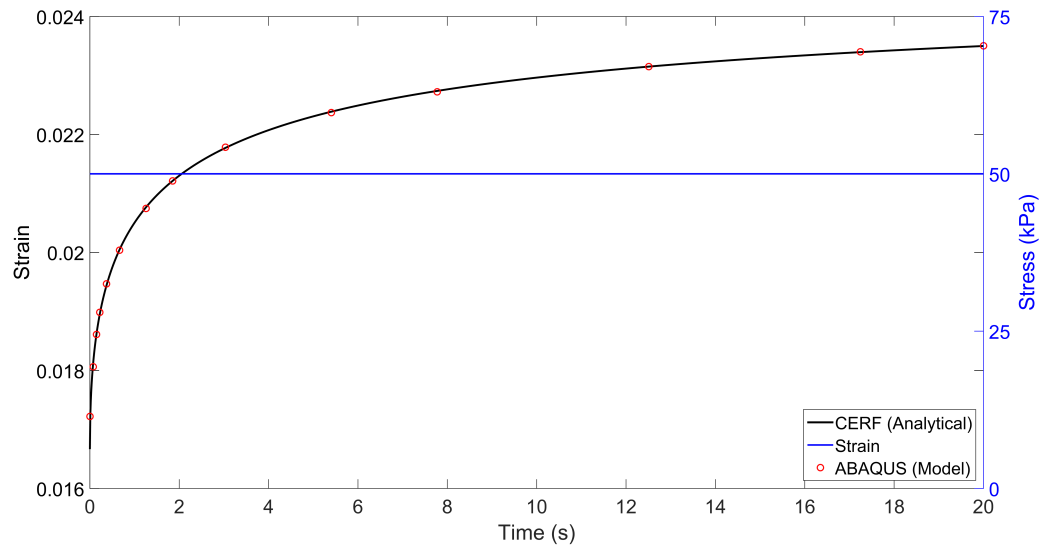
(b) Creep

Figure 26: Stress relaxation and creep validation of CERF viscoelastic model in ABAQUS
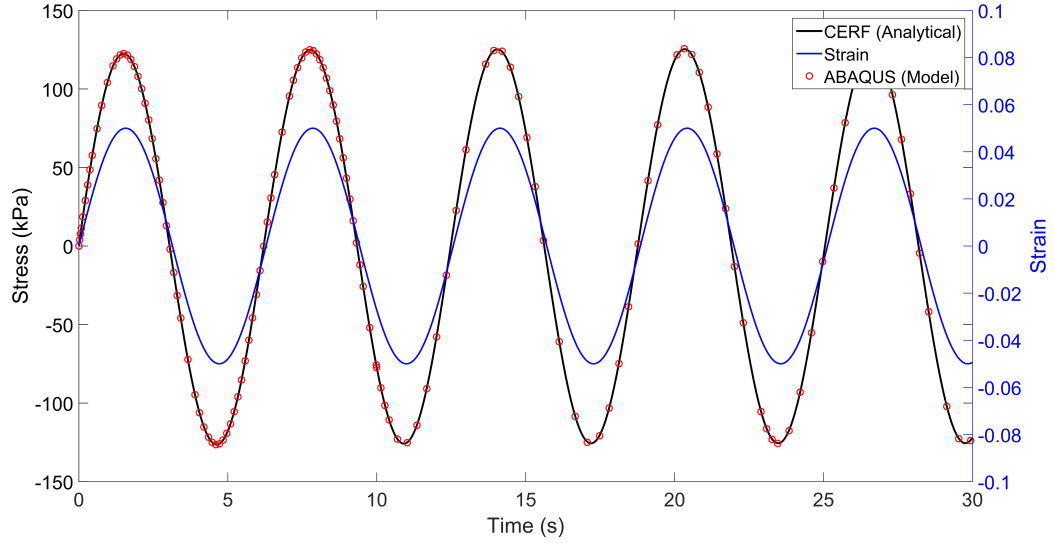
Figure 27: Validation of CERF viscoelastic model in ABAQUS from sinusoidal strain input

that there is not a known creep modulus formulation (with the exception of a Prony series with one Maxwell element). Therefore, to use these models, the creep data must be intercoverted to stress-relaxation data. Interconversion uses the theoretical relationship of the creep and relaxation modulus to translate between moduli without imposition of a constitutive model. The stress/strain formulations for viscoelasticity:

$$\sigma\left(t\right) = \epsilon\left(0\right) E\left(t\right) + \int_0^t \dot{\epsilon}\left(\tau\right) E\left(t - \tau\right) \, \mathrm{d}\tau, \tag{1}$$

and

$$\epsilon\left(t\right) = \sigma\left(0\right) J\left(t\right) + \int_0^t \dot{\sigma}\left(\tau\right) J\left(t - \tau\right) \, \mathrm{d}\tau, \tag{2}$$

are directly related in the Laplace domain:

$$\sigma\left(s\right) = sE\left(s\right)\epsilon\left(s\right), \tag{3}$$

and

$$\epsilon\left(s\right) = sJ\left(s\right)\sigma\left(s\right) \tag{5}$$

70

by substituting Eq. 5 into Eq. 3:

$$1 = s^2 J(s) E(s),$$
(111)

leading to the direct relationship between creep and relaxation modulus in the Laplace domain:

$$E(s) = \frac{1}{s^2 J(s)}.$$
(112)

The inverse Laplace transform is applied to Eq. 111, giving a convolution of the creep and relaxation moduli:

$$t = \int_0^t E(t - \tau) J(\tau) d\tau,$$
(113)

which can be differentiated to give a convenient relationship between the creep and relaxation moduli:

$$1 = E(0) J(t) + \int_0^t \dot{E}(t - \tau) J(\tau) d\tau.$$
(114)

The initial condition is determined at $t = 0$:

$$E(0) J(0) = 1,$$
(115)

and then the convolution integral is evaluated numerically, leading to a recursive relationship for the creep modulus [94, 95]:

$$J(t_n) = -J(t_{n-1}) +$$
$$\frac{4t_n - \sum_{i=1}^{n-1} (J(t_i) + J(t_{i-1}))(E(t_n - t_{i-1}) + E(t_n - t_{i-1}))(t_i - t_{i-1})}{(E(0) + E(t_n - t_{n-1}))(t_n - t_{n-1})},$$
(116)

where $n \geq 2$. When $n = 1$,

$$J(t_1) = \frac{3 - E(t_1)/E(0)}{G(0) + G(t_1)}.$$
(117)

Likewise, the relaxation modulus is interconverted with the same algorithm ($n \geq 2$):

$$E(t_n) = -E(t_{n-1}) +$$
$$\frac{4t_n - \sum_{i=1}^{n-1} (E(t_i) + E(t_{i-1}))(J(t_n - t_{i-1}) + J(t_n - t_{i-1}))(t_i - t_{i-1})}{(J(0) + J(t_n - t_{n-1}))(t_n - t_{n-1})},$$
(118)

71

Table 7: Input parameters for interconversion

Description	Symbol	Value (units)
Viscoelastic relaxation constants	E_0	8 (MPa)
	E_1	10 (MPa)
Relaxation time constant	λ	0.25 $(1/s)$
Viscoelastic creep constants	J_0	0.125 $(1/MPa)$
	J_1	0.0694 $(1/MPa)$
Creep time constant	τ	9 (s)

and

$$E(t_1) = \frac{3 - J(t_1)/J(0)}{J(0) + J(t_1)}. \tag{119}$$

Interconversion is a powerful tool because it allows the user to control the independent variable in a stress/strain or force/displacement simulation. In situations such as the coupled PVE/HDL problem, there is only one choice of independent variable that is physically realizable. However, the fitting functions from the correspondence principle are better suited for the opposite analysis. Interconversion links the two moduli, and allows for convenient fitting in the time-domain. Ultimately, interconversion is a tool that gives the user additional avenues for constitutively modeling the storage and loss properties of a system. In addition, the applications for viscoelasticity are apparent as well.

Figures 28 and 29 show the interconversion process for a known analytical solution. The parameters used in this example are given in Table 7. Interconversion of creep to relaxation and *vice versa* is an important step in specifying viscoelastic models. Additionally, interconversion is used to evaluate storage and loss properties of the coupled PVE/HDL problem.
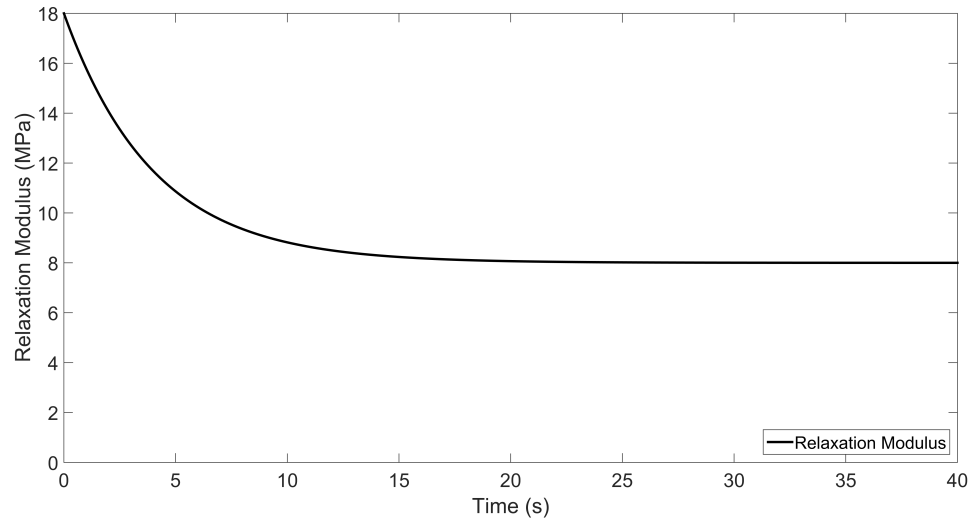
(a) Relaxation modulus from 1-term Prony series
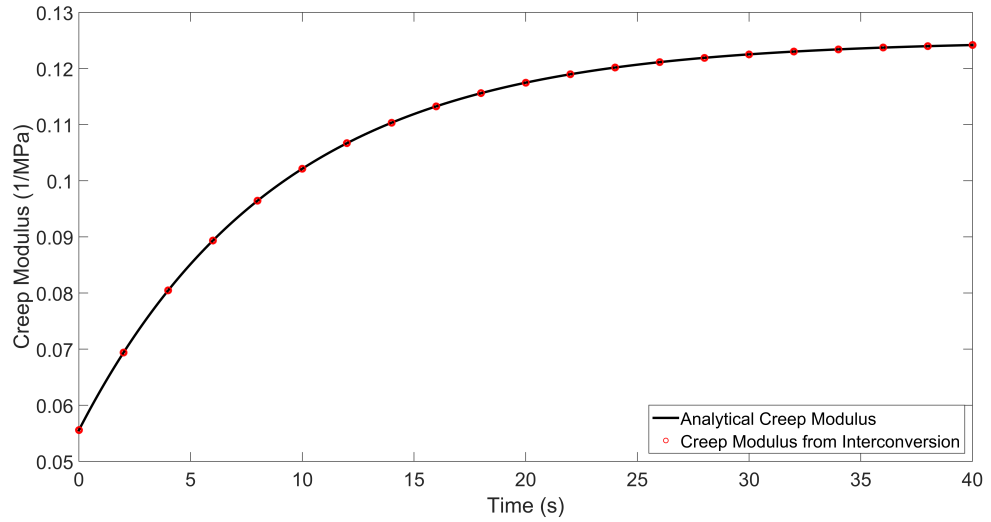
(b) Creep modulus from analytical and interconversion solutions

Figure 28: 1-term Prony series interconversion from relaxation to creep modulus
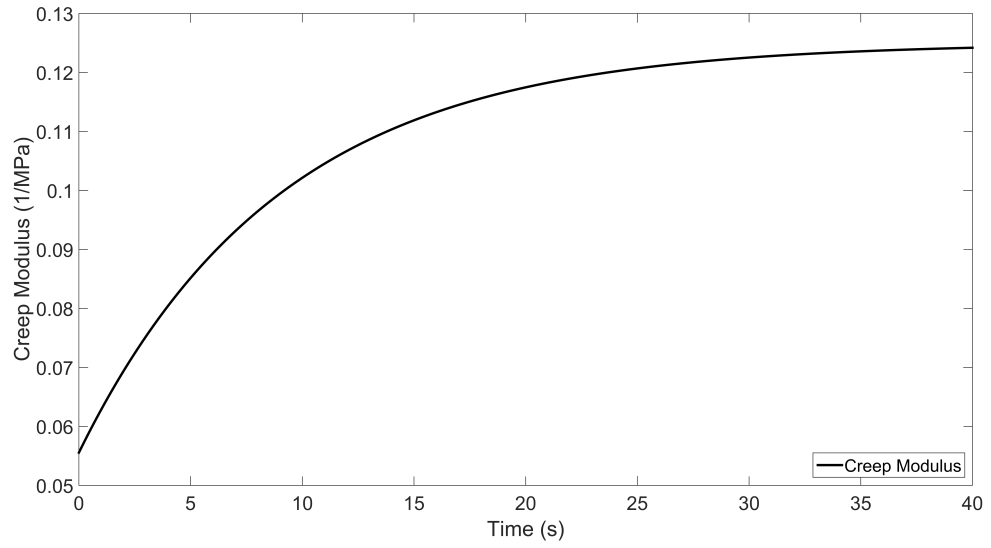
(a) Creep modulus from 1-term Prony series
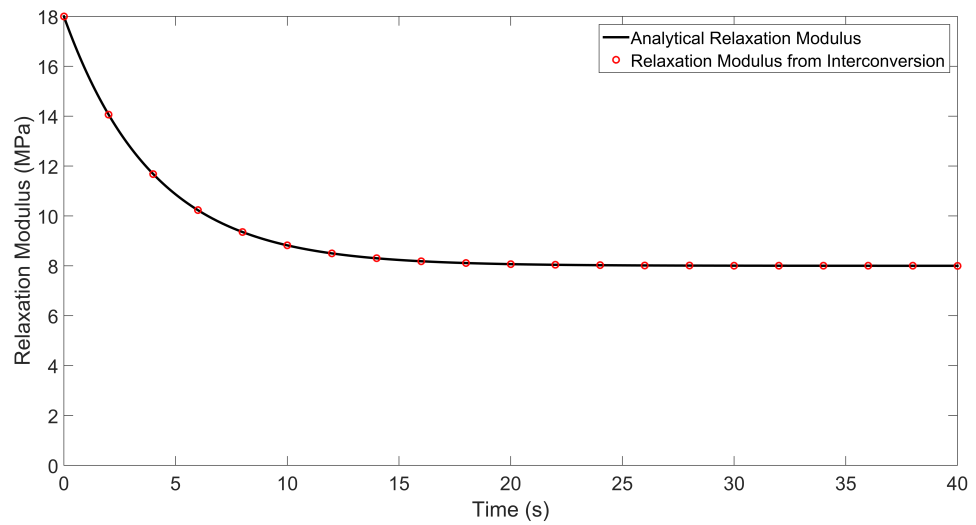
(b) Relaxation modulus from analytical and interconversion solutions

Figure 29: 1-term Prony series interconversion from creep to relaxation modulus

CHAPTER V

POROUS REYNOLDS EQUATION

The fluid mechanics of thin-films are well-defined for conventional, rigid, triboelements. The resulting Reynolds equation, which is derived from the Navier-Stokes equations and continuity, is ubiquitous in tribological applications. However, the traditional Reynolds equation assumes no-slip conditions occurring between rigid plates. With a porous and flexible interface, the boundary conditions must be modified. This is accomplished in a number of ways, with a popular method attributed to Beavers and Joseph [96]. This chapter addresses the governing fluid mechanics of a thin film on a porous substrate. The results are compared to the rigid case for a range of substrate permeability values.

5.0.4 Derivation of Porous Reynolds Equation

Consider the geometrically simple design of a thrust bearing, as shown in Fig. 30a. The surface plates have no-slip at the rigid interface, leading to the well-known iso-viscous and incompressible Reynolds equation [97]:

$$\frac{\partial}{\partial x}\left(\frac{\partial P}{\partial x}h^3\right) + \frac{\partial}{\partial z}\left(\frac{\partial P}{\partial z}h^3\right) = 12\mu\left[\frac{\partial}{\partial x}\left(\frac{-U_1 h}{2}\right) + U_1\frac{\partial h}{\partial x} + \frac{\partial h}{\partial t}\right]. \tag{120}$$

Now consider allowing one of the rigid surface plates to be flexible and porous, as shown in Fig. 30b. At the lower boundary of the film, flow is allowed to permeate into (or out of) the porous medium. In addition, pressure generated in the fluid can cause deformation of the porous substrate. It is desired to describe the fluid mechanics in this configuration in a similar manner to the rigid case. Mathematically, this is accomplished by modifying the boundary condition on the lower surface, and solving for new fluid velocities in the film channel.
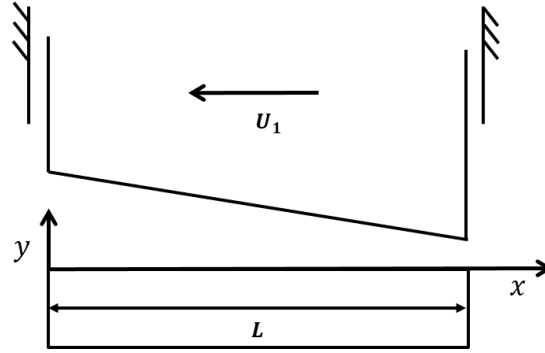
(a) Thrust bearing with rigid interfaces
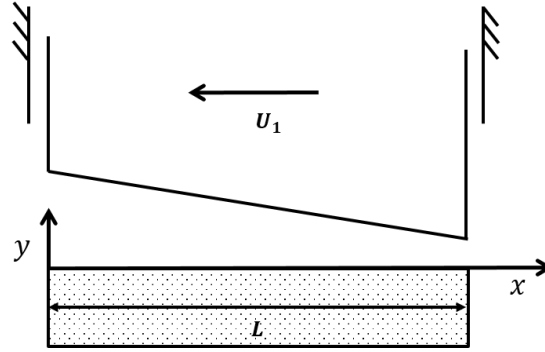
(b) Thrust bearing with porous interface on bottom boundary

Figure 30: Thrust bearings in the rigid and porous cases
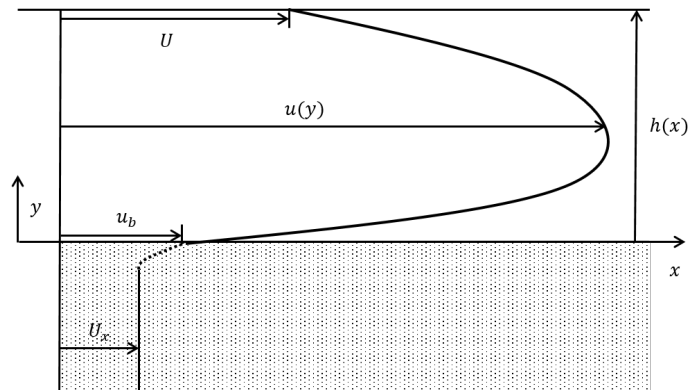
Figure 31: Boundary layer approximated by the Beavers-Joseph boundary condition (modified from [96])

The introduction of a porous and flexible boundary, shown in Fig. 30b, modifies the boundary conditions of the Reynolds equation. A popular porous boundary condition is attributed to Beavers and Joseph [96]. Beavers and Joseph provide a slip-flow condition for the porous interface, which is based on experimental findings. Fig. 31 represents the fluid velocity profiles in the fluid channel and the porous filter. At the no-slip interface $(y = h)$, the fluid velocity is U, and at the porous interface $(y = 0)$, the fluid velocity is u_B. The porous filter velocity (from Darcy's law) is U_x. The Beavers and Joseph boundary condition relates the interface velocity to the filter velocity. In effect, the slip-flow boundary condition approximates the boundary layer shown in Fig. 31. Mathematically, the slip-flow condition is given as [96]:

$$\left.\frac{\partial u}{\partial y}\right|_{y=0} = \frac{\alpha_B}{\sqrt{k}} \left[u_B - U_x\right] \tag{121}$$

where α_B is a slip-coefficient, and k is the permeability of the porous structure. Beavers and Joseph show that this *ad hoc* boundary condition reasonably captures experimental results for a range of materials. In reality, it is unlikely that slip is actually occurring at the interface; however, the slip-coefficient helps to rectify the results from experiments and the theory. Therefore, the slip coefficient is a useful parameter for the designer to retain. The porous interface is incorporated in the Reynolds equation by modifying one of the rigid boundary conditions.

Following the usual assumptions of the Reynolds equation, the fluid velocity terms are defined as:

$$\frac{\partial^2 u}{\partial y^2} = \frac{1}{\mu}\frac{\partial P}{\partial x} \tag{122}$$

$$\frac{\partial^2 v}{\partial y^2} = 0. \tag{123}$$

$$\frac{\partial^2 w}{\partial y^2} = \frac{1}{\mu}\frac{\partial P}{\partial z} \tag{124}$$

The Beavers-Joseph slip condition is applied as a boundary condition at $y = 0$:

$$\left.\frac{\partial u}{\partial y}\right|_{y=0} = \frac{\alpha_B}{\sqrt{k}} \left[u\left(x, 0, z\right) - U_x\left(x, 0, z\right)\right] \tag{125}$$

$$v\left(x, 0, z\right) = -V_0\left(x, 0, z\right) - V'\left(x, 0, z\right). \tag{126}$$

$$\left.\frac{\partial w}{\partial y}\right|_{y=0} = \frac{\alpha_B}{\sqrt{k}} \left[w\left(x, 0, z\right) - W_z\left(x, 0, z\right)\right], \tag{127}$$

where U_x, V_0, and W_z are Darcy flow terms (filter velocities):

$$U_x = k\left.\frac{\partial P}{\partial x}\right|_{y=0} \tag{128}$$

$$V_0 = k\left.\frac{\partial P}{\partial y}\right|_{y=0} \tag{129}$$

$$W_z = k\left.\frac{\partial P}{\partial z}\right|_{y=0}. \tag{130}$$

At the no-slip boundary $(y = h)$:

$$u\left(x, h, z\right) = -U_1 \tag{131}$$

$$v\left(x, h, z\right) = -V_1, \tag{132}$$

$$w\left(x, h, z\right) = 0. \tag{133}$$

Equations. 125-133 define the boundary of the fluid film channel. Returning to Eq. 122, and integrating with respect to y yields:

$$\frac{\partial u}{\partial y} = \frac{1}{\mu}\frac{\partial P}{\partial x}y + C_1, \tag{134}$$

and integrating again for the u velocity:

$$u\left(y\right) = \frac{1}{2\mu}\frac{\partial P}{\partial x}y^2 + C_1 y + C_2. \tag{135}$$

With reference to the boundary conditions, at $y = 0$, Eq. 135 equals:

78

$$u(0) = C_2, \tag{136}$$

which is inserted into Eq. 125:

$$\left.\frac{\partial u}{\partial y}\right|_{y=0} = \frac{\alpha_B}{\sqrt{k}} \left[C_2 - U_x\left(x, 0, z\right)\right], \tag{137}$$

and rearranged:

$$C_2 = \frac{\sqrt{k}}{\alpha_B} \left.\frac{\partial u}{\partial y}\right|_{y=0} + U_x\left(x, 0, z\right). \tag{138}$$

The derivative term is found naturally from Eq. 134:

$$\left.\frac{\partial u}{\partial y}\right|_{y=0} = C_1, \tag{139}$$

which gives C_1 and C_2 in terms of each other:

$$C_2 = \frac{\sqrt{k}}{\alpha_B} C_1 + U_x\left(x, 0, z\right). \tag{140}$$

The second boundary condition at $y = h$ allows for C_1 and C_2 to be solved:

$$u(h) = -U_1 = \frac{1}{2\mu} \frac{\partial P}{\partial x} h^2 + C_1 h + C_2. \tag{141}$$

It remains an exercise in algebra to arrive at the simplified equation for fluid velocity in the x direction:

$$\begin{aligned} u(y) = \frac{1}{2\mu} \frac{\partial P}{\partial x} &\left[y^2 - \left(y + \frac{\sqrt{k}}{\alpha_B}\right)\left(\frac{h^2 - 2k}{h + \sqrt{k}/\alpha_B}\right) - 2k\right] \\ &- \left(\frac{U_1}{h + \sqrt{k}/\alpha_B}\right)\left(y + \frac{\sqrt{k}}{\alpha_B}\right). \end{aligned} \tag{142}$$

Equation 142 describes the fluid velocity in the x-direction as a function of geometry (h), fluid viscosity (μ), pressure gradient ($\partial P/\partial x$), bearing velocity (U_1), and the two

porous parameters permeability (k) and slip coefficient (α_B). From these parameters, two nondimensional groupings are created to simplify Eq. 142:

$$\xi_0 = \frac{\sqrt{k}/\alpha_B}{h + \sqrt{k}/\alpha_B} \tag{143}$$

$$\xi_1 = \frac{3\left[h\left(\sqrt{k}/\alpha_B\right) + 2k\right]}{h\left(h + \sqrt{k}/\alpha_B\right)} \tag{144}$$

Equations 143 and 144 effectively modify the film thickness, based on the properties of the porous substrate. With those groupings, the velocity profile in the x-direction is determined:

$$u(y) = \frac{1}{2\mu}\frac{\partial P}{\partial x}(y - h)\left(y + \frac{1}{3}h\xi_1\right) - \frac{U_1}{h}\left[y\left(1 - \xi_0\right) + h\xi_0\right]. \tag{145}$$

As the permeability approaches the non-porous case ($k \to 0$), the film modifiers approach zero ($\xi_0 \to 0$, $\xi_1 \to 0$), and Eq. 145 agrees with the conventional fluid velocity of the Reynolds equation. The w velocity follows an identical derivation as u, except that Couette flow in the z-direction is not considered in this work:

$$w(y) = \frac{1}{2\mu}\frac{\partial P}{\partial z}(y - h)\left(y + \frac{1}{3}h\xi_1\right) \tag{146}$$

The velocity profiles u and w describe the lateral flow of lubricant in the fluid channel. Applying continuity in the fluid channel:

$$\frac{\partial(\rho v)}{\partial y} = -\frac{\partial(\rho u)}{\partial x} - \frac{\partial(\rho w)}{\partial z} - \frac{\partial \rho}{\partial t}, \tag{147}$$

and inserting the fluid velocities (Eqs. 145 and 146):

$$\frac{\partial(\rho v)}{\partial y} = -\frac{\partial}{\partial x}\left\{\frac{\rho}{2\mu}\frac{\partial P}{\partial x}(y - h)\left(y + \frac{1}{3}h\xi_1\right) - \frac{U_1}{h}\left[y\left(1 - \xi_0\right) + h\xi_0\right]\right\}$$
$$- \frac{\partial}{\partial z}\left\{\frac{\rho}{2\mu}\frac{\partial P}{\partial z}(y - h)\left(y + \frac{1}{3}h\xi_1\right)\right\} - \frac{\partial \rho}{\partial t}. \tag{148}$$

The continuity equation is integrated with respect to y using the following boundary conditions at the bearing interface:

$$v(y = 0) = V_0 + V' \tag{149}$$

80

$$v(y = h) = V \tag{150}$$

where V_0 is the fluid velocity entering or leaving the porous medium (governed by Darcy's law). V' is the velocity of the flexible interface due to deformation, and V is the conventional squeeze term:

$$V = \frac{\partial h}{\partial t}. \tag{151}$$

These boundary conditions are retained after Eq. 148 is integrated across the film (with respect to y):

$$
\begin{aligned}
\int d(\rho v) dy = & -\int_0^h \frac{\partial}{\partial x}\left\{\frac{\rho}{2\mu}\frac{\partial P}{\partial x}(y - h)\left(y + \frac{1}{3}h\xi_1\right)\right\} dy \\
& + \int_0^h \frac{\partial}{\partial x}\left\{\frac{\rho U_1}{h}\left[y(1 - \xi_0) + h\xi_0\right]\right\} dy \\
& - \int_0^h \frac{\partial}{\partial z}\left\{\frac{\rho}{2\mu}\frac{\partial P}{\partial z}(y - h)\left(y + \frac{1}{3}h\xi_1\right)\right\} dy \\
& - \int_0^h \frac{\partial \rho}{\partial t} dy.
\end{aligned}
\tag{152}
$$

The integrals of Eq. 152 are integrated using Leibniz's theorem:

$$
\begin{aligned}
\int_{u_0(v)}^{u_1(v)} \frac{\partial}{\partial v} f(\phi, v) d\phi = & \frac{\partial}{\partial v}\int_{u_0(v)}^{u_1(v)} f(\phi, v) d\phi \\
& - f(u_1, v)\frac{\partial u_1}{\partial v} + f(u_0, v)\frac{\partial u_0}{\partial v}.
\end{aligned}
\tag{153}
$$

For example, if the following substitutions are made:

$$v = x, \qquad \phi = y, \qquad u_0(x) = 0, \qquad u_1(x) = h(x),$$

$$f_1(y, x) = \frac{\rho}{2\mu}\frac{\partial P}{\partial x}(y - h)\left(y + \frac{1}{3}h\xi_1\right)$$

$$f_2(y, x) = \frac{\rho U_1}{h}\left[y(1 - \xi_0) + h\xi_0\right],$$

then Eq. 153 is used for the terms that correspond to the x-direction:

$$
\begin{aligned}
\int_0^h \frac{\partial}{\partial x}\left\{\frac{\rho}{2\mu}\frac{\partial P}{\partial x}(y - h)\left(y + \frac{1}{3}h\xi_1\right) - \frac{\rho U_1}{h}\left[y(1 - \xi_0) + h\xi_0\right]\right\} dy = \\
\frac{\partial}{\partial x}\int_0^h \frac{\rho}{2\mu}\frac{\partial P}{\partial x}(y - h)\left(y + \frac{1}{3}h\xi_1\right) dy - f_1(h, x)\frac{\partial h}{\partial x} + f_1(0, x)\frac{\partial \emptyset}{\partial x} - \\
\frac{\partial}{\partial x}\int_0^h \frac{\rho U_1}{h}\left[y(1 - \xi_0) + h\xi_0\right] dy + \frac{\rho U_1}{h}\frac{\partial P}{\partial x}\left[h(1 - \xi_0) + h\xi_0\right]\frac{\partial h}{\partial x} + f_2(0, x)\frac{\partial \emptyset}{\partial x}
\end{aligned}
\tag{154}
$$

Assuming the the density and viscosity of the fluid do not depend on spatial coordinates ($\rho \neq \rho(x, y, z), \mu \neq \mu(x, y, z)$), the integrals in Eq. 154 are readily evaluated:

$$\int_0^h \frac{\partial}{\partial x} \left\{ \frac{\rho}{2\mu} \frac{\partial P}{\partial x} (y - h) \left(y + \frac{1}{3} h \xi_1 \right) - \frac{\rho U_1}{h} \left[y (1 - \xi_0) + h \xi_0 \right] \right\} dy =$$
$$\frac{\partial}{\partial x} \left\{ \frac{\rho}{12\mu} \frac{\partial P}{\partial x} \left[-h^3 (1 + \xi_1) \right] \right\} - \frac{\partial}{\partial x} \left[\rho U_1 \frac{h (\xi_0 + 1)}{2} \right] + \rho U_1 \frac{\partial h}{\partial x} \tag{155}$$

The same process is used for the z-direction:

$$\int_0^h \frac{\partial}{\partial z} \left\{ \frac{\rho}{2\mu} \frac{\partial P}{\partial z} (y - h) \left(y + \frac{1}{3} h \xi_1 \right) \right\} dy =$$
$$\frac{\partial}{\partial z} \left\{ \frac{\rho}{12\mu} \frac{\partial P}{\partial z} \left[-h^3 (1 + \xi_1) \right] \right\}, \tag{156}$$

and the density term:

$$\int_0^h \frac{\partial \rho}{\partial t} dy = h \frac{\partial \rho}{\partial t}. \tag{157}$$

Combining the results of Eqs. 155 - 157, and performing the simple integration on the left hand side of Eq. 152 with the boundary conditions given in Eqs. 149-150 yields the modified Reynold's equation:

$$\frac{\partial}{\partial x} \left\{ \frac{\partial P}{\partial x} \left[h^3 (1 + \xi_1) \right] \right\} + \frac{\partial}{\partial z} \left\{ \frac{\partial P}{\partial z} \left[h^3 (1 + \xi_1) \right] \right\} =$$
$$12\mu \left\{ \frac{\partial}{\partial x} \left[\frac{-U_1 h (\xi_0 + 1)}{2} \right] + U_1 \frac{\partial h}{\partial x} + \frac{h}{\rho} \frac{\partial \rho}{\partial t} + (V + V_0 + V') \right\}. \tag{158}$$

Equation 158 is further simplified by assuming the density does not change with respect to time:

$$\frac{\partial}{\partial x} \left\{ \frac{\partial P}{\partial x} \left[h^3 (1 + \xi_1) \right] \right\} + \frac{\partial}{\partial z} \left\{ \frac{\partial P}{\partial z} \left[h^3 (1 + \xi_1) \right] \right\} =$$
$$12\mu \left\{ \frac{\partial}{\partial x} \left[\frac{-U_1 h (\xi_0 + 1)}{2} \right] + U_1 \frac{\partial h}{\partial x} + (V + V_0 + V') \right\}. \tag{159}$$

Equation 159 is the Reynolds equation with a porous boundary. As the permeability of the substrate decreases, ξ_0 and ξ_1 approach zero, and Eq. 159 degenerates to the conventional Reynolds equation presented in Eq. 120.

$$k \to 0, \quad \xi_0 \to 0, \quad \xi_1 \to 0$$

$$\frac{\partial}{\partial x}\left(\frac{\partial P}{\partial x}h^3\right) + \frac{\partial}{\partial z}\left(\frac{\partial P}{\partial z}h^3\right) =$$
$$12\mu\left[\frac{\partial}{\partial x}\left(\frac{-U_1 h}{2}\right) + U_1\frac{\partial h}{\partial x} + (V + V')\right]. \tag{160}$$

The previous exercise leads to the definition of an effective film thickness that considers the contribution of permeability of the substrate:

$$H_1^3 = h^3\left(1 + \xi_1\right). \tag{161}$$

Conversely, as the permeability of the substrate increases, the effective film thickness increases approximately with the square root of k:

$$k \gtrsim O(h^2), \quad \xi_0 \to 1, \quad H_1^3 \propto \sqrt{k}.$$

Increasing the permeability of the substrate means that the fluid can move more freely through the porous medium. Therefore, the effective fluid film thickness is increased compared to the rigid case. Some example results are presented for a porous interface in the following section.

5.0.5 Implications of Porous Boundary on Reynolds Equation (Left Hand Side)

The Beavers-Joseph boundary condition is considered for its effect on the velocity profile in the fluid channel (Eq. 145). Figure 32 shows the apparent slip at the porous boundary $(y = 0)$ for a virtually parallel channel (as shown in Fig. 31). The parameters used for Fig. 32 are given in Table 8. At the top interface $(y = h)$, no slip occurs, and the fluid moves with the journal's velocity U_1, while the lower, porous interface experiences non-zero velocity, u_b. This is in contrast to the rigid, no-slip case, where $u/U_1 = 0$ at $y = 0$ (also shown in Fig. 32). Beavers and Joseph indicate that real materials have slip coefficients between $\alpha_B = 0.001$ and $\alpha_B = 10$. The implications of a porous boundary are to change the relative fluid velocity between the two plates. In cases where α_B is large (e.g. lattice foametals), there is a large effect on the velocity profile. This can even cause a negative velocity at the interface if
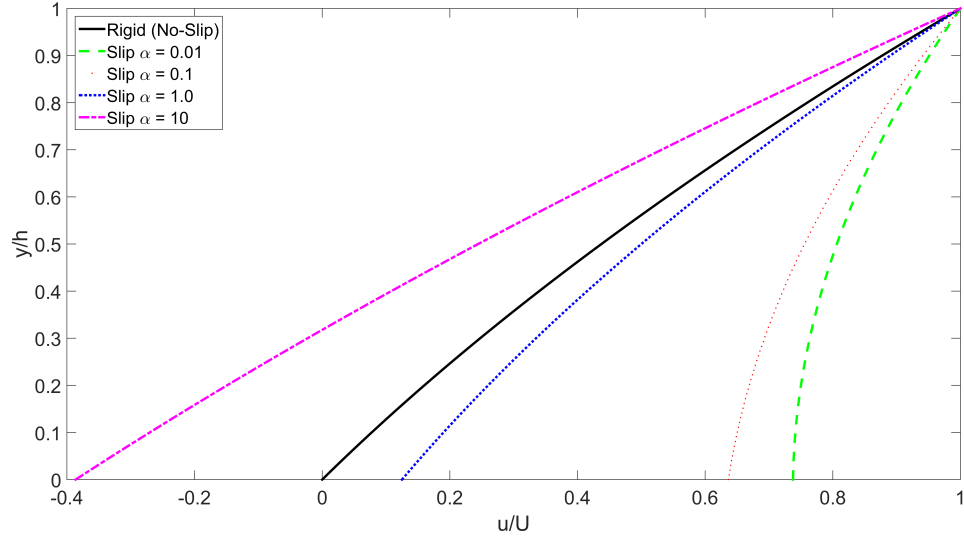
Figure 32: Velocity profile in fluid channel for rigid and slip cases

Table 8: Parameters for Beavers-Joseph slip analysis

Parameter	Symbol	Value (units)
Permeability	k	10^{-10} (m^2)
Pressure gradient	$\frac{dP}{dx}$	0.50 $(kPa/\mu m)$
Channel height	h	100 (μm)
Fluid viscosity	μ	1 $(Pa \cdot s)$
Bearing velocity	U_1	0.1 (m/s)

the Poiseuille flow is large enough and acts counter to the Couette flow. In the case of the Poiseuille flow acting counter to the Couette flow, there is a unique combination of α_B and k that replicates the no-slip condition.

Permeability plays an important role in the left hand side (LHS) of the porous Reynolds equation. Consider the previously defined effective film thickness, H_1, and its dependence on permeability. Figure 33 shows the effective film thickness for various materials, normalized by the geometric film thickness dimension (corresponding to the rigid case). The consequence of permeability is very large over a range of
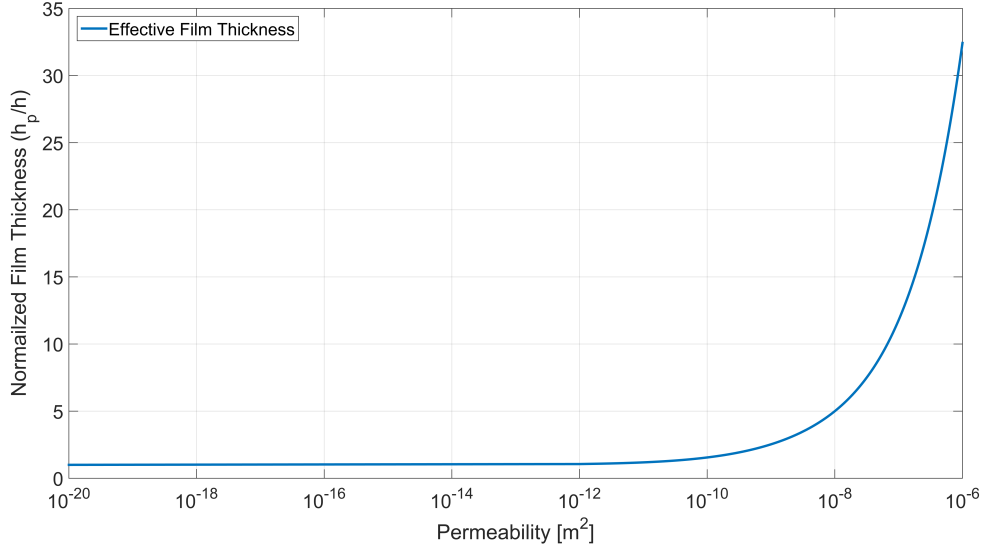
Figure 33: Effective film thickness relative to permeability

realistic materials. Figure 33 shows that the effective film thickness is proportional to the square root of permeability, as discussed previously. A permeable boundary changes the nature of hydrodynamic lubrication. It is desired to understand these changes, and try to shape them in a beneficial way. To accomplish this, the hydrodynamic lubrication problem must be solved in an accurate and expedient manner. The following section addresses the numerical aspects of simulating the HDL problem with a porous interface.

5.0.6 Numerical Solution of the Porous Reynolds Equation

The porous Reynolds equation is solved with a finite volume/finite difference technique [98]. The aforementioned substitution of H_1 (Eq. 161) is made in the porous Reynolds equation (Eq. 159):

$$
\frac{\partial}{\partial x}\left(H_1^3\frac{\partial P}{\partial x}\right) + \frac{\partial}{\partial z}\left(H_1^3\frac{\partial P}{\partial z}\right) =
$$
$$
12\mu\left\{\frac{\partial}{\partial x}\left[\frac{-U_1 h\left(\xi_0 + 1\right)}{2}\right] + U_1\frac{\partial h}{\partial x} + (V + V_0 + V')\right\}. \tag{162}
$$
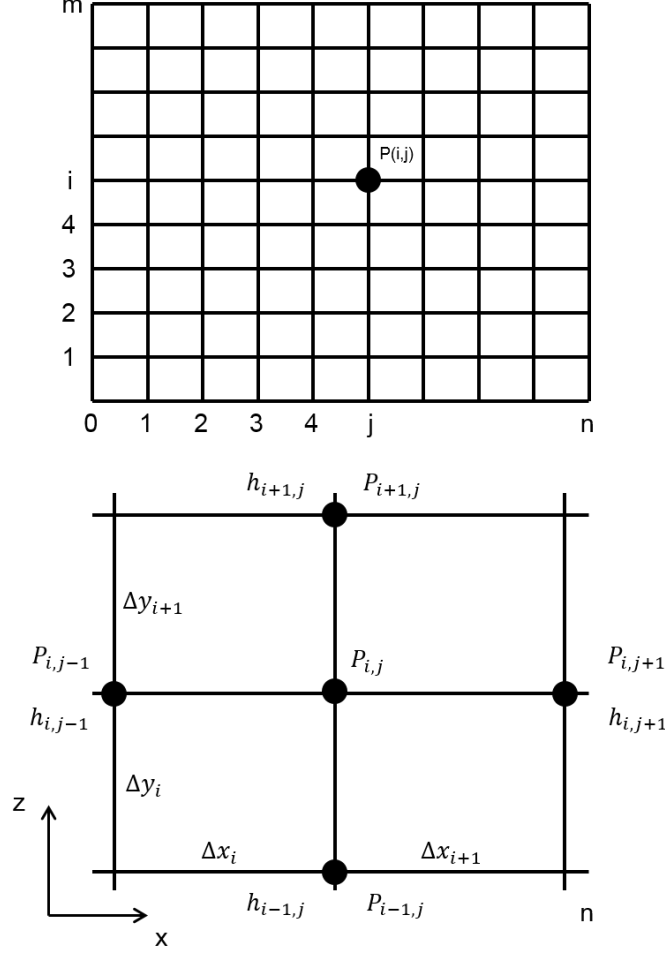
Figure 34: Numerical discretization of hydrodynamic lubrication problem, reproduced from [98]

Then, the bearing domain is discretized according to Fig. 34:

$$\left[\frac{\partial}{\partial x}\left(H_1^3\frac{\partial P}{\partial x}\right)\right]_{i,j} + \left[\frac{\partial}{\partial z}\left(H_1^3\frac{\partial P}{\partial z}\right)\right]_{i,j} =$$
$$12\mu\left\{\frac{\partial}{\partial x}\left[\frac{-U_1 h\left(\xi_0+1\right)}{2}\right] + U_1\frac{\partial h}{\partial x} + \left(V + V_0 + V'\right)\right\}_{i,j}. \tag{163}$$

The derivatives are evaluated with a central difference numerical method, the details of which are given in Appendix A. With the known and calculated terms, the Reynolds equation is solved for pressure at each step:

$$P_{i,j} = \left(a_1 P_{i,j+1} + a_2 P_{i,j-1} + a_3 P_{i+1,j} + a_4 P_{i-1,j} + a_0\right) \tag{164}$$

86

The constants, a_i, are also given in Appendix A. Various numerical techniques, such as Jacobi's or Gauss-Seidel iteration, can be used to solve for $P_{i,j}$. Convergence and local and global error tolerances are accessed at the same time. Depending on the bearing type and geometry, relevant boundary conditions are applied. In the current work, the pressure at the boundary is atmospheric:

$$P(0, z, t) = P(L, z, t) = P(x, 0, t) = P(x, D, t) = 0. \tag{165}$$

However, in other triboelement types, the boundary conditions may need to reflect more complex arrangements, such as cavitation. This might be of particular interest if lubricant is drawn from the porous pad in such regions. Such work is left for future study.

The numerical solution is validated for the non-porous case with the works of Pinkus [99], Green [98], and the known long and short bearing solutions [97]. In addition, the porous HDL solution is qualitatively shown in agreement with Prakash and Vij [63] and Etsion and Michael [64], although the application of their studies is different.

5.1 Implications of Porous Boundary

In the case where rigid/porous boundaries exist in triboelements, the physics can sometimes be solved analytically. A long or short bearing approximation must be used for the Reynolds equation, and the porous solution (Laplace's equation) is coupled to the fluid dynamics. Prakash and Vij [63] and Etsion and Michael [64] use this approach. However, the solution to Laplace's equation is an infinite sum of harmonic equations, lessening the advantage of solving the problem analytically. The numerical solution to Laplace's equation is straightforward, and can also be coupled to the HDL problem by sharing pressure information at the porous/fluid boundary. In addition, the full 2D Reynolds equation can be used. Therefore, the numeric solution

Table 9: Parameters for pressure profile comparison at various permeabilities

Parameter	Symbol	Value (units)
Bearing length	L	25 (mm)
Bearing depth	D	0.5 (m)
Inlet film thickness	h_i	40 (μm)
Ratio of inlet/outlet films	a	2.2
Fluid viscosity	μ	0.1 $(Pa \cdot s)$
Bearing velocity	U_1	0.02 (m/s)
Beavers-Joseph Slip Coefficient	α_B	0.1
Bearing velocity	U_1	0.1 (m/s)
Maximum pressure	P_{max}	38.7 (kPa)
Load support (per unit depth)	W	606 (N/m)

of Laplace's equation will be used to determine the pressure in a porous body. This naturally couples with the porous Reynolds equation at shared nodes.

Although the porous Reynolds equation differs from the rigid case in principle, the pressure profile that is generated by solving the porous Reynolds equation has a similar shape to that of the traditional Reynolds equation, as shown in Fig. 35. Therefore, the character of the pressure profile remains similar for the porous and non-porous cases. In Fig. 36, the geometry of the bearing is held constant while the permeability is varied. Essentially, the bearing is operating at steady-state, and the vertical flow of fluid into the bearing is neglected ($V = V_0 = V' = 0$). Table 9 gives the simulation parameters. The resulting pressure profiles are shown in 1D. Although greater permeabilities erode the pressure magnitude, and therefore the load support, the shape of the pressure profile does not significantly change.

When film thickness is fixed, the sensitivity to permeability is apparent, as shown in Fig. 37. The range of permeabilities shown in Fig. 37 span many orders of
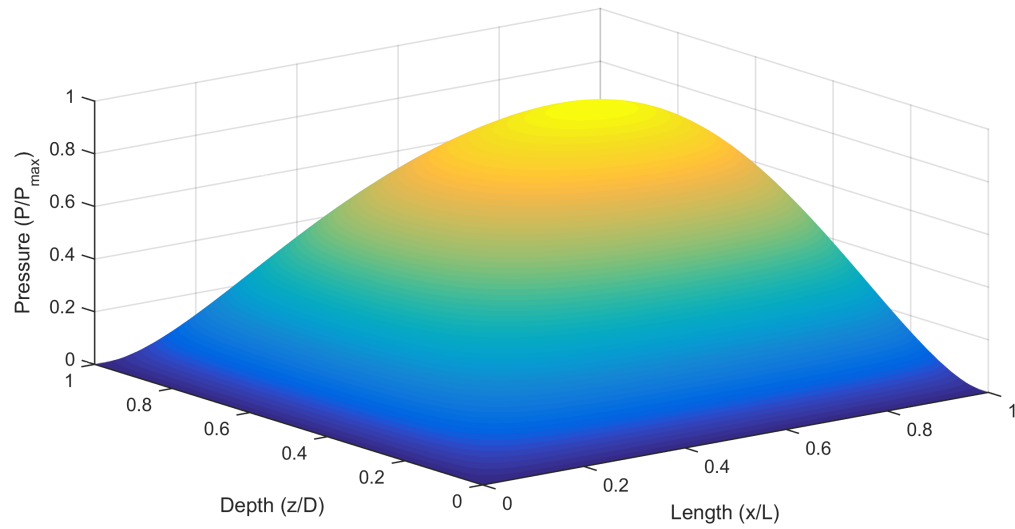
Figure 35: Representative 2D pressure profile from porous Reynolds equation
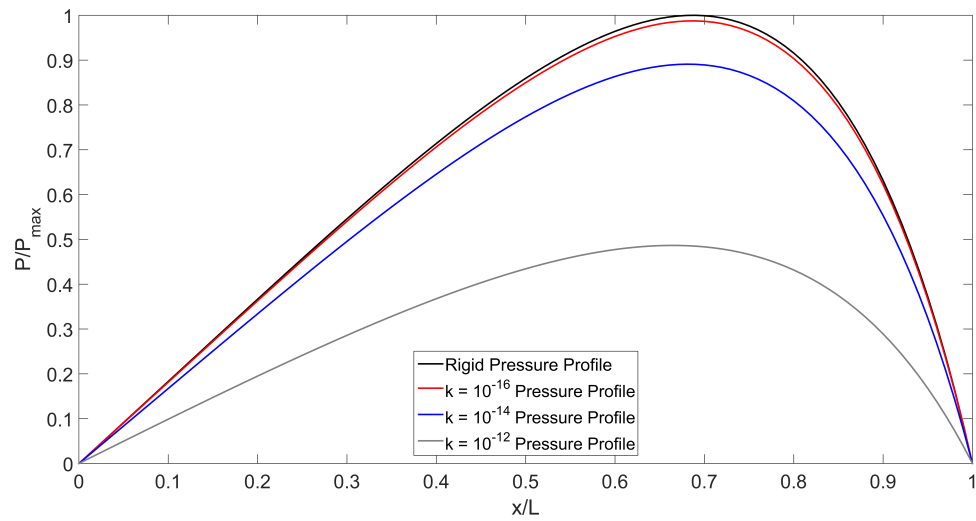
Figure 36: 1D pressure profile from porous Reynolds equation for various permeabilities
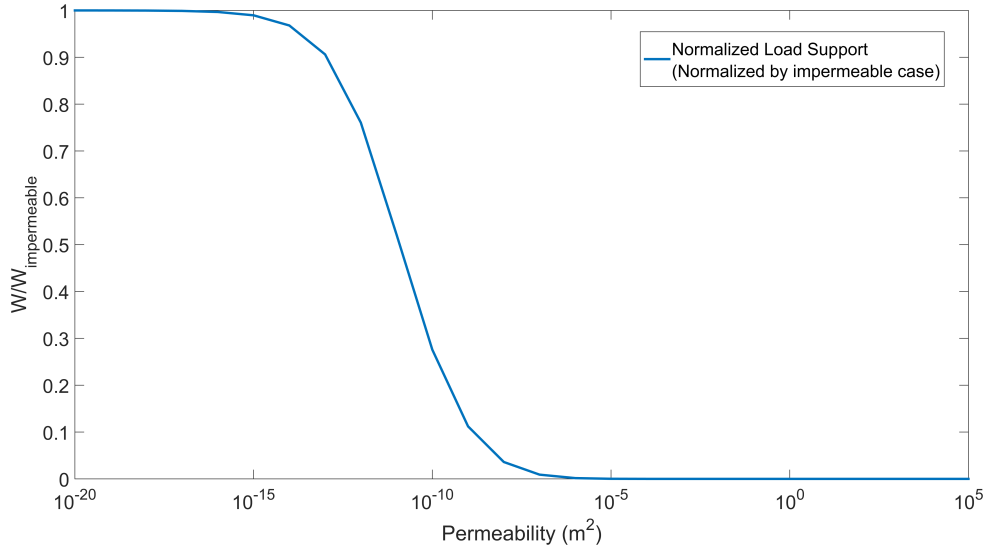
Figure 37: Normalized load support relative to permeability

magnitude, but also encompass many promising materials, from articular cartilage ($k \approx 10^{-14}$ $[m^2]$) to polyurethane foams ($k \approx 10^{-9}$ $[m^2]$). To sustain appreciable loads, a relatively low permeability is required. However, coupled with an elastic or viscoelastic action, the PVE pad can significantly influence triboelement performance. Like a sintered bearing, lubricant availability from the porous substrate is an operational advantage [100]. It is hypothesized that these bearing types could have use in harsh operating environments, where shock loads or lubricant loss are possible.

The geometry of the porous substrate is a design consideration; however, it proves to be less influential for the example parameters chosen. This is shown in Fig. 38 for various pad length to width ratios (at the said fixed inlet film thickness, and $k = 10^{-14}$). The influence of the porous pad's depth on load support capacity is marginal except for extremely shallow or deep pads. For permeabilities low enough to support fluid film loads, the pressure gradient at the interface does not appear to be significantly influenced by the pad's dimensions. The pad depth is larger than the film thickness by at least one order of magnitude in this simulation. Larger pressures may alter the sensitivity to pad geometry; however, general bearing pad configurations
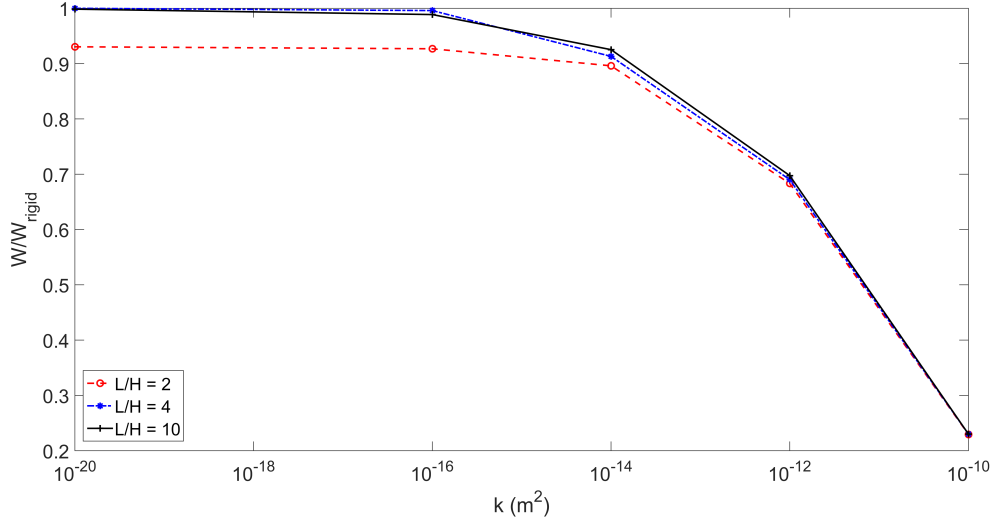
Figure 38: Load support versus permeability for different pad length to height ratios

will not see a large variation in load support (or film thickness for fixed loads) due to the pad dimensions.

Permeability and the slip coefficient are important considerations on the LHS of the Reynolds equation. Another strong coupling phenomenon is the vertical flow of lubricant into (or out of) the bearing substrate. This manifests as the Darcy flow term on the RHS of the Reynolds equation. To solve the Reynolds equation, the pressure in the substrate must be known, and visa versa. Practical limits on permeability and geometry are obtained with the aforementioned figures.

The rigid/porous case allows for analysis of the fluid coupling terms in the porous Reynolds equation. In these simulations, the substrate is not allowed to deform. It will be shown in the following chapters that deformation of the substrate is a significant consideration. In many applications, the PVE pad deformation becomes the dominant mechanism for consideration in the coupled HDL/PVE simulations.

CHAPTER VI

COUPLING OF HYDRODYNAMIC LUBRICATION AND POROVISCOELASTICITY

The individual components of the poroviscoelastic model and the accompanying porous Reynolds equation have been developed in the previous chapters. What remains is to couple these phenomena and simulate the resulting behavior. This discussion is centered around the finite-element program ABAQUS; however, efforts are made to generalize the solution techniques of coupled solid-fluid interactions.

Two solution approaches for coupling the PVE/HDL mechanisms are discussed in this chapter. Both techniques are used to arrive at steady-state; however, one method proves superior in determining the dynamic properties of storage and loss.

6.1 Model Specifications

A two-dimensional (x, y) porous pad is hydrodynamically loaded from a sliding bearing that generates fluid pressure by means of a converging gap. The 2D case is specified as a test bed for understanding the physics of a coupled PVE/HDL bearing design. ABAQUS is used as the analysis tool for the coupled phenomena. This is done for two predominant reasons: prevalence in academia and industry, and support of pore-pressure elements. A number of pore pressure elements exist in the ABAQUS element library. The element chosen for the current study is CPE8RP. These elements are plane strain, 8 node elements with biquadratic displacement and bilinear pore pressure. In addition, reduced integration is supported. The CPE8RP element is a 2D element that is compatible with a coupling fluid pressure from the long bearing $(L >> D)$ solution of the Reynolds equation (neglecting pressure gradients in the

z-direction).

The FEA model of the porous pad is designed in a generic manner, so that a variety of boundary conditions and loads can be tested. A number of these boundary conditions are explored in the following chapter. In general, the boundary conditions must be specified for both phases of the material. Therefore, fluid pressure and solid stresses/strains must be specified at the boundary of the porous pad. The top boundary of the porous pad interfaces with the HDL load; therefore, the fluid boundary condition must be matched at this boundary. Flow into and out of the porous pad is naturally enforced by the pressure gradient in the pad, meaning that lubricant is assumed available in excess at the pad boundary (flooded conditions). In the ABAQUS pore pressure elements, flow only occurs at the pore pressure nodes. By matching meshes and grids between the PVE and HDL problems, the pore pressure is naturally coupled at the boundary. The nodal results are interpolated to give a smooth flow profile for analysis purposes.

6.1.1 Simulation Description

The coupled PVE/HDL problem is solved with a combination of finite elements and finite volume/finite difference methods. The HDL solution acts as a continuously updating load on the substrate. ABAQUS uses a variable time marching technique to expedite the solution procedure when possible. The time incrementation is controlled according to the solution history. A fixed time step can be specified if a uniform time step is desired; however, this greatly reduces simulation efficiency.

The solution to the coupled problem is performed in multiple steps to alleviate convergence issues. The first step places a hydrodynamic load on the surface of the poroviscoelastic pad, and reaches a fluid pressure equilibrium in the porous body. This is defined in ABAQUS as a geostatic step, which iterates until the initial stress state of the model is in equilibrium with the boundary conditions/loads. The use

of a geostatic step is necessary for model convergence, particularly for simulations with large pressures, and relatively fast deformations in the porous medium. After the geostatic step, the subsequent steps "release" the pad to deform according to the physics of the material, subjected to a fluid pressure load (obtained from the porous Reynolds equation). The simulation is run to steady-state, where certain system properties are obtained. After reaching steady-state, the simulation can be continued to determine the properties of storage and loss (outlined in Chapter 7).

6.2   Simulation to Steady-State

Two methods were developed to obtain the steady-state response of the coupled PVE/HDL problem. Steady-state is the normal operational condition for the bearing configuration, and represents a baseline for performance metrics. The properties of storage and loss are obtained relative to the steady-state solution, and indicate the bearing's performance due to a system disturbance. Figure 39 diagrams the general control schematic for the coupled simulation, as steady-state is obtained.

6.2.1   Method I: Separation of Convergence Mechanisms

The first method is driven externally to ABAQUS with a script procedure written in the programming language Python. The poromechanics are defined and solved by ABAQUS while the fluid mechanics are solved by Python. Figure 40 displays the flow of information when this approach is used. Essentially, the Python script applies an initial fluid load on the solid material and begins the simulation in ABAQUS. The simulation progresses in time (causing deformation) to a specified time increment, where the pertinent results are stripped from the output database (.odb). The results are used to modify the Reynolds equation by assessing a new film profile and the vertical diffusion into the porous substrate. The new pressure profile becomes an updated boundary condition on the solid mechanics, and the process is repeated until steady-state is achieved.
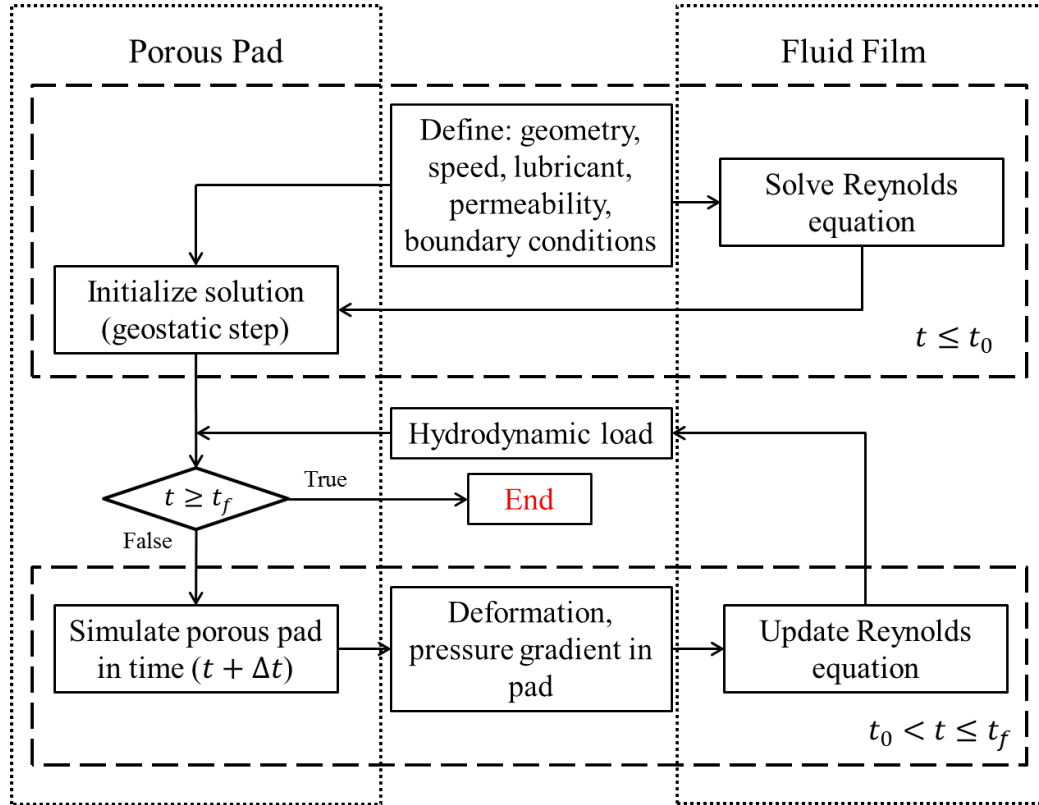
Figure 39: Schematic of coupling between HDL and PVE problems, including initialization

The advantage of this method is that ABAQUS is manipulated externally, and the results are retrieved naturally from the ABAQUS user interface. Python has built-in features that allows for the evaluation of the Reynolds equation numerically, as described in Chapter 4. Python is the scripting language of ABAQUS; therefore, a full complement of features are available and supported by ABAQUS. This is particularly useful for parametric studies, as Python routines can be used to vary parameters and geometries. Additionally, the ABAQUS graphical user interface can be used to modify the geometry, load, and boundary conditions. An example is given in Appendix B for the coupling procedure used with Method I.

The disadvantage of the aforementioned method is that two time scales are used to solve the problem: one for the FEA simulation, and one for the HDL solution. Therefore, the path taken to steady-state is not physical, although the state is. To access dynamic properties from steady-state, a different method is used; however, to arrive at steady-state efficiently, Method I can be used. A second method is proposed to alleviate the different time scales used in Method I.

6.2.2 Method II: Coupled Convergence Mechanisms

The second method to couple the solid and fluid mechanics is to track the solid mechanics, and at each increment update the load case. This is accomplished with user subroutines in ABAQUS. Four primary subroutines are needed to strip data from the simulation, update and solve the fluid mechanics, and apply the new fluid load to the solid mechanics. The flow of information for this case is shown in Fig. 41. In contrast to Method I, the solution of the solid and fluid mechanics is updated at each increment with Method II. This leads to a physically meaningful path to steady-state from the initial conditions, and likewise allows for the determination of storage and loss relative to a steady-state position. One proposed advantage of the poroviscoelastic substrate is the transient response to a disturbance; therefore,
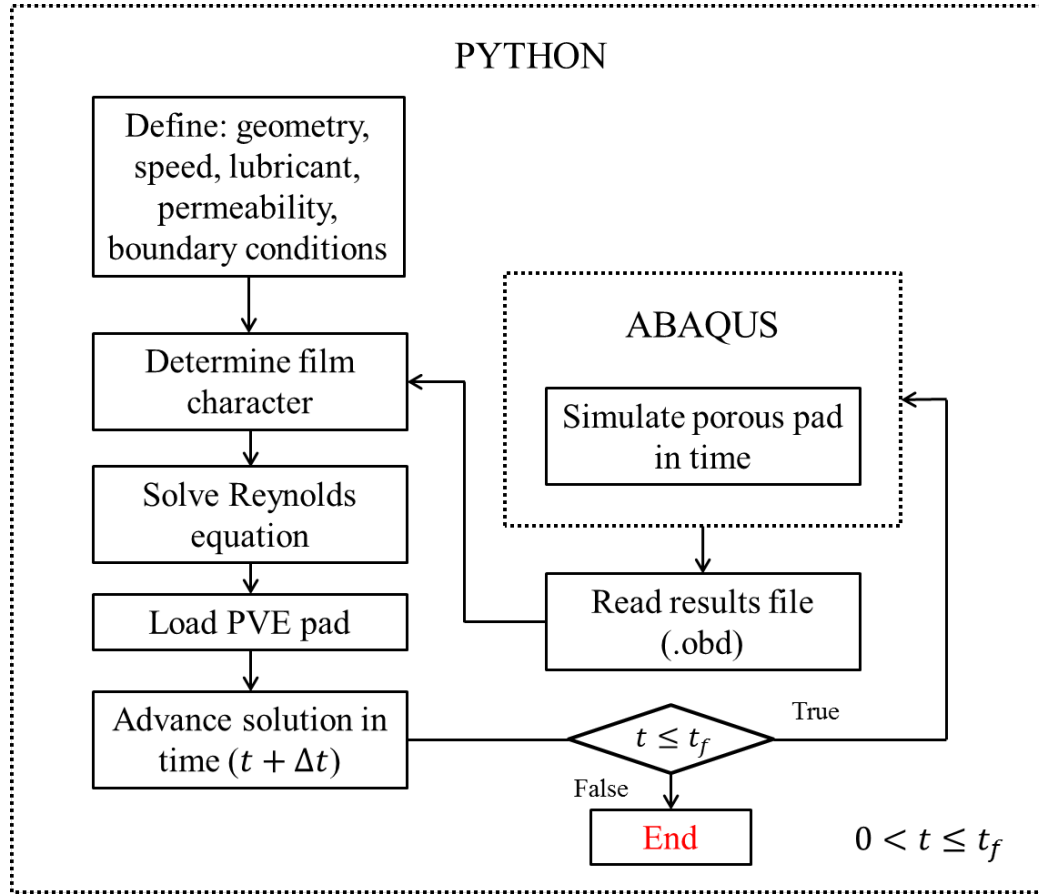
Figure 40: Flow of information schematic for Method I

Method II is required to determine these characteristics.

In Method II, the solid and fluid mechanics are evaluated at each time step. The flow of information is given in Fig. 41. At each time step, simulation results are queried from the .fil file, which is accessed with the 'URDFIL' subroutine. Internal subroutines are all written in FORTRAN, and called directly by ABAQUS. The .fil file contains field variables (e.g. displacements, stresses, pore pressures) relative to node or element identifiers. The pertinent results are stripped and rearranged in an array that is common to all of subroutines. The interface displacement is obtained and combined with the fixed bearing geometry to create a film thickness profile for the bearing. This film thickness is an input to the Reynolds equation solver, which is another FORTRAN subroutine. The Reynolds equation subroutine takes geometric, material, and state variables ($\frac{\partial p}{\partial y}$) and returns the updated pressure profile. This information is used to modify the film thickness in time (using the squeeze term, V). The film thickness changes are made over time so that the film thickness is a continuous function. This is consistent with the physics of an incompressible fluid.

After the solution of the Reynolds equation converges, the pressure is determined at the nodal points of the porous material. The fluid routine can have the same or a different mesh from the solid mechanics; however, if different meshes are chosen, then interpolation is used to determine the nodal pore pressures. These pore pressures are imposed as a boundary condition in ABAQUS by use of the 'DISP' subroutine. Additionally, the solid phase of the PVE material is loaded with the 'CLOAD' subroutine ($\sigma = -P$). This load and boundary condition is appropriate for fluid loaded materials [31,83]. Examples of the FORTRAN subroutines and input files are presented in Appendix B.
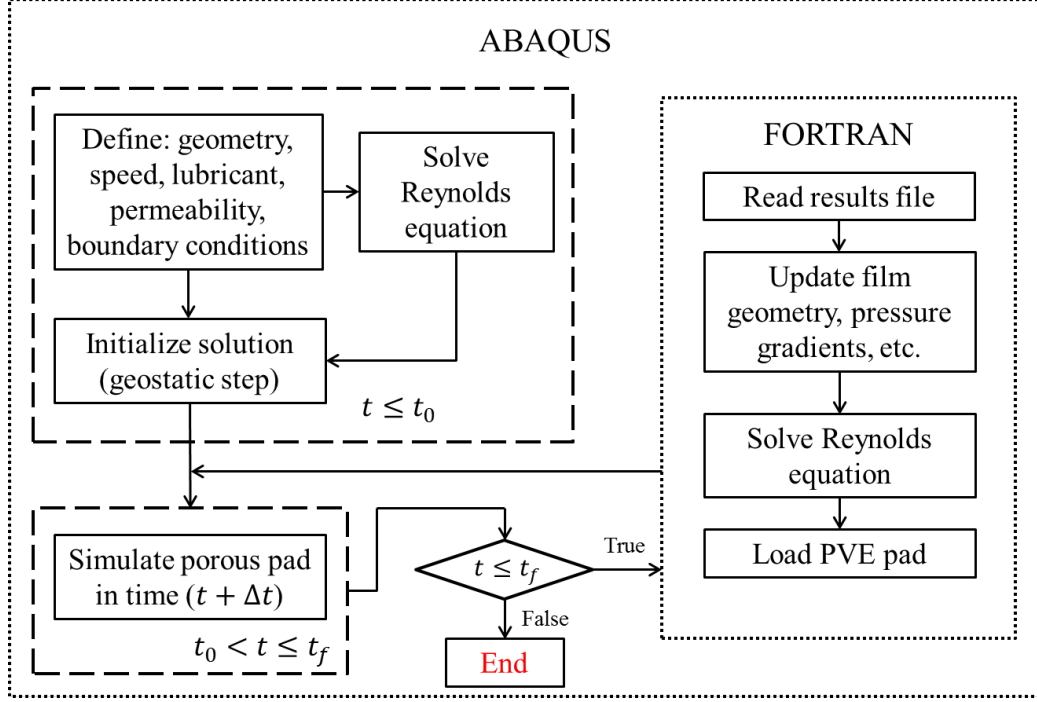
Figure 41: Flow of information schematic for Method II

6.2.3 Comparison to Methods I and II

The two methods outlined herein represent different approaches for arriving at steady-state for the coupled HDL/PVE problem. In addition to the convergence mechanism differences of Methods I and II, there is a fundamental difference in the parent/child relationship. ABAQUS is the child in Method I and the parent in Method II. However, both Methods reach the same steady-state solution for identical simulations (geometry, mesh, load support, etc.). Figure 42 shows the path to steady-state for Method I and Method II, respectively. In Figure 42a, the displacement of the middle node $(x = L/2)$ from the top edge of the porous pad is tracked versus time. Figure 42b shows a zoomed-in portion of the same simulation as Figure 42a, which highlights the different solution techniques. Method I and Method II do not have the same transient response, although the paths are very similar. Method II more accurately simulates the behavior of an actual material; however, Method I reaches an identical steady

state. Figure 43 shows the deformation of the porous substrate at steady-state. Both methods have converged to the same solution (with a maximum of 0.01% difference in the example problem).

Method I is more user-friendly, and allows for full Python functionality. This is particularly useful for parametric studies, and for modifying accuracy tolerances, time-steps, etc. In cases where the initial conditions are not close to the equilibrium solution, Method I can provide a smoothing effect in the early stages of the solution. This reduces the chances of the solution diverging, and/or small time increments causing spurious oscillations in the poromechanics solution [87]. If the time increment used in Method I is reduced to the time increment used by ABAQUS, Method I will take the same solution path as Method II; however, the storage space and simulation time will balloon to unrealistic requirements.

Method II is less user-friendly, requiring modifications to the input (.inp) and user-subroutine (.for) files for any simulation changes. However, Method II is superior for modeling transient behavior, as the coupling forces from the fluid film are updated at every increment. In addition, example problems indicate that Method II is actually a more compact simulation in terms of output file sizes and simulation time. It is hypothesized that Method II is more computationally efficient because it makes smaller changes to the poromechanics boundary conditions between iterations. Therefore, the simulation is able to use larger time steps while maintaining simulation accuracy. As the primary driver of simulation time is due to the poromechanics (not the fluid mechanics), Method II solves the coupled simulation more efficiently. In addition, accessing the .fil file (Method II) is more efficient than the .odb file (Method I). The additional programming burden of Method II makes distribution and modification of the developed codes challenging; however, the input file (.inp) for Method II can be generated in part with the Python script of Method I. This improves the usability and distribution of Method II substantially.
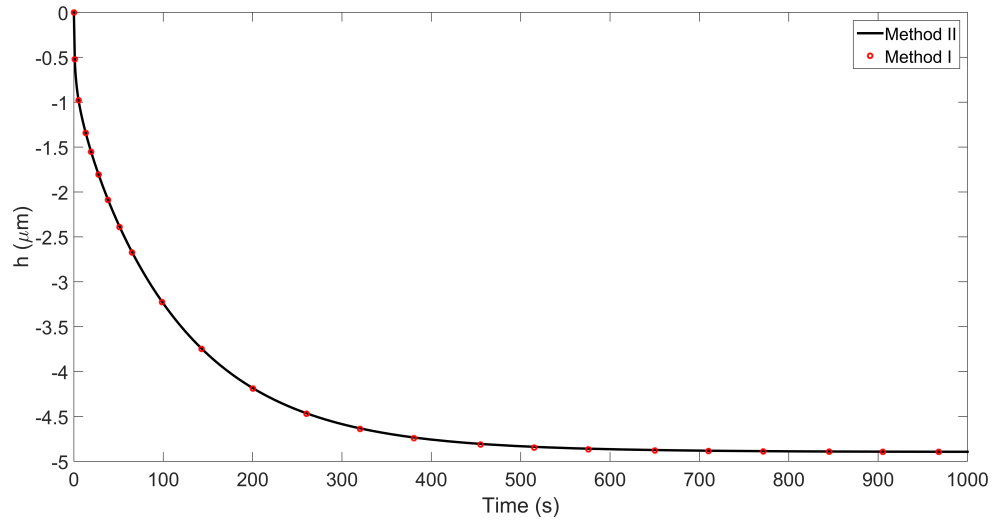
(a) Entire simulation path
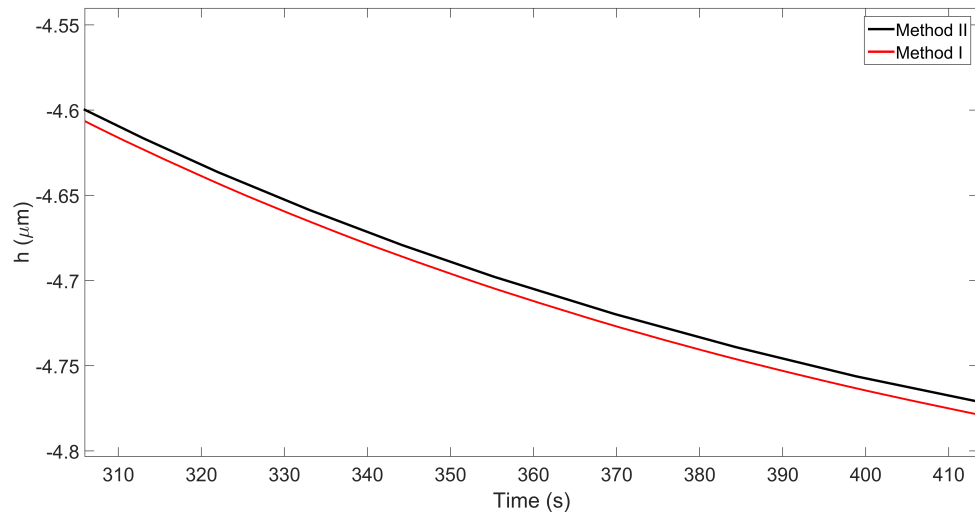
(b) Zoom in portion showing offset between methods

Figure 42: Path of node deforming with respect to time, comparing Method I and Method II

101
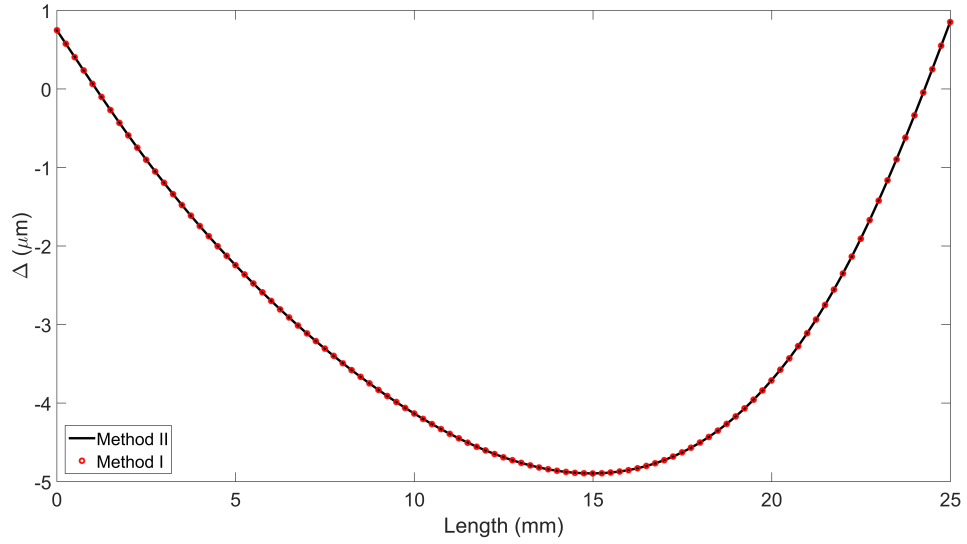
Figure 43: Steady-state solution showing pad deformation solved by Methods I and II

The two methods developed herein provide a framework for solving coupled solid/fluid problems. In the current application, Method II is deemed superior for determining the desired quantities, particularly storage and loss. However, both methods give a routine that can be used to solve problems from similar classes. A skeleton code for each method is listed in Appendix B in hopes that it will be useful for those trying to couple disparate phenomena. While the provided framework gives a technique for modeling triboelement performance, the numerical models must be tested in relation to mesh density, fidelity, and simulation time. These considerations are addressed in the following section.

6.3   Mesh Convergence

Simulating both the fluid and solid mechanics requires a discretization of the physical domain. To verify that the discretization chosen for each mechanism is appropriate, a mesh convergence study is performed. A benchmark with prescribed conditions (geometric and material) is assessed for the individual mechanisms. For the Reynolds

Table 10: Parameters for mesh convergence

Parameter	Symbol	Value (units)
Permeability	k	10^{-14} (m^2)
Load per depth	W	600 (N/m)
PVE pad length	L	25.00 (mm)
PVE pad height	H	12.50 (mm)
Fractional elastic modulus	E_0	9.5 (MPa)
Fractional elastic modulus	E_1	10 (MPa)
Fractional dissipative constant	μ_1	4 $(s^{-1/2})$
Poisson's ratio	ν	0.25

equation, a fixed height slider bearing is studied. For the poroviscoelastic material, a fixed fluid pressure is imposed on a material face. Both of these cases are varied relative to the grid density, and the solutions provide some guidance on acceptable grid fidelity moving forward. The computational expense of solving the finite element model is significantly greater than that of solving the Reynolds equation. This is in part because the Reynolds equation contains one fewer spatial dimensions. Therefore, the mesh size and density of the finite element analysis is the primary driver of simulation time.

6.3.1 ABAQUS Mesh Convergence

A mesh convergence study is performed for a specified example geometry and loading. The parameters used in this analysis are presented in Table 10. The displacement and fluid flux at the top edge of the porous pad are the quantities of interest.

The results of the mesh convergence study give insight into PVE/HDL simulations. Figures 44a and 44b show that higher loads demand finer meshes to maintain pore pressure tolerances. In fact, the minimum number of elements required to complete the simulation depends on the loading condition. A usable minimum number of

elements must be established depending on the parameters of the simulation. In addition, more compliant materials also require finer meshes, as time-dependent changes to the model cause the largest deviations to the pressure profile generated from the HDL solution. These large changes potentially translate to model divergence issues. The primary metrics of interest in the porous pad are deformations in the top surface, and pressure gradients across the same boundary. Figures 44a and 44b indicate that the displacements of the top edge are relatively insensitive to mesh density, once a minimum threshold is met to ensure that the model solves. A delicate balance exists between model fidelity and solution time, and the mesh density should be examined for each set of parameters chosen to study. In general, models that meet the solution tolerances set forth will be converged for the displacement and pressure gradients at the porous interface. In the current study, 1250 elements are used to simulate the PVE pad, with a deformation tolerance less than 0.2% of the densest mesh tested. The following section discusses the mesh convergence of the fluid film load which couples to the PVE simulation.

6.3.2 Reynolds Mesh Convergence

The Reynolds equation is solved in accordance to the methods outlined in Chapter 5. Equivalent mean pressure loads are chosen for the lower pressure ($\sim 1MPa$) and higher pressure ($\sim 10MPa$) cases taken from the ABAQUS simulation. Figures 45a and 45c show the lower load mesh convergence for load and mean pressure, respectively. The load and mean pressure have different convergence rates because a Simpson's 1/3 integral rule is used to determine the load support, while the mean pressure is determined as the average pressure across the bearing's length.

Figures 46a and 46c show the higher load mesh convergence for load and mean pressure, respectively. Clearly, the 1D Reynold's equation does not require a very fine grid to converge at the tested pressures. It is advantageous to match the grid of the
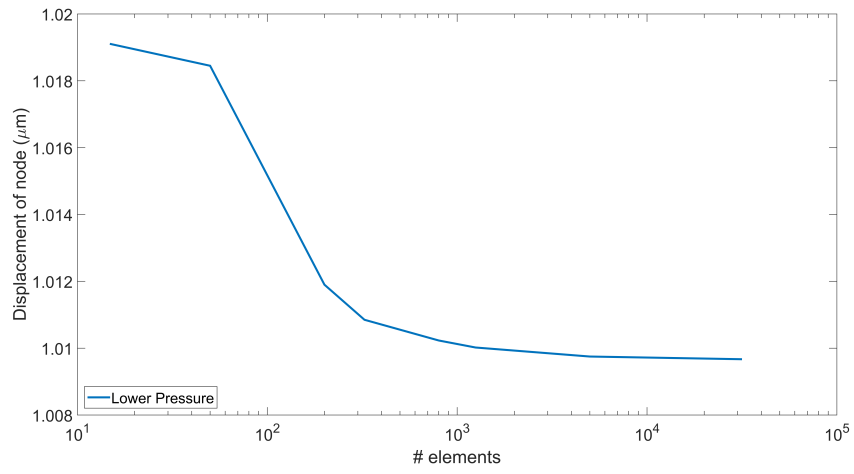
(a) Mesh convergence for low pressure load
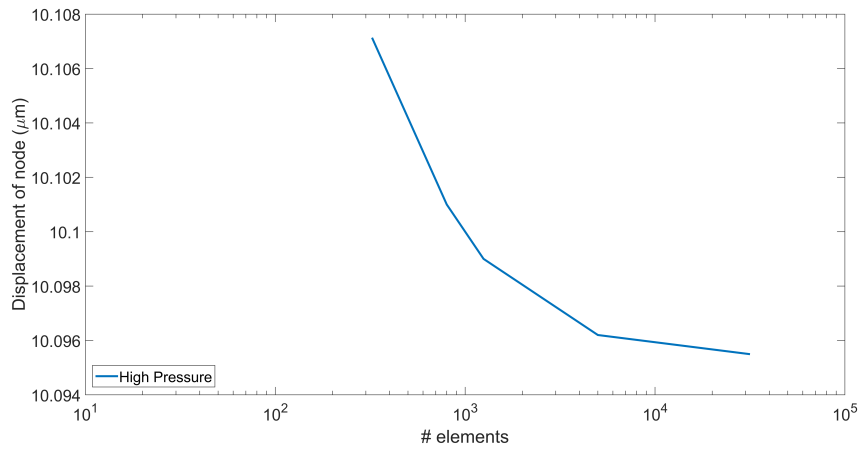
(b) Mesh convergence for high pressure load
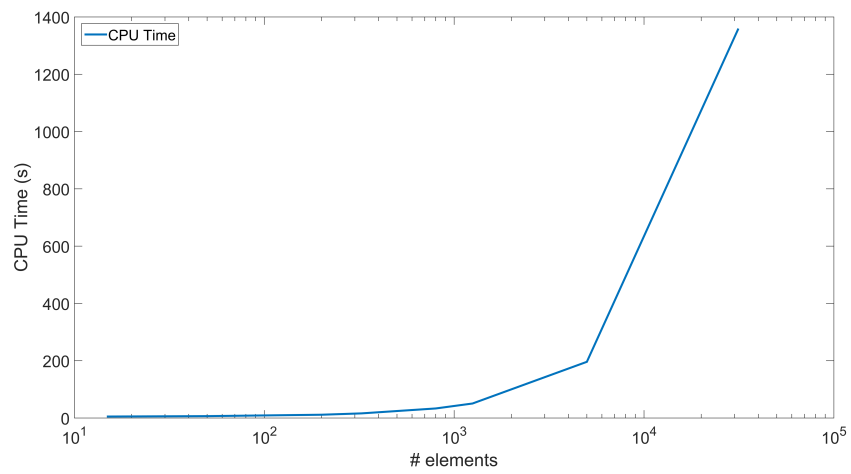
(c) CPU time for simulation (low pressure)

Figure 44: Mesh convergence study of FEA solution

105

Table 11: Example parameters used for Reynolds mesh convergence study

Parameter	Symbol	Value (units)
Bearing length	L	$25\ mm$
Inlet film thickness	h_i	$30\ \mu m$
Outlet/inlet film thickness ratio	a	2.2
Viscosity	μ	$0.5\ Pa \cdot s$
Slip coefficient	α_B	0.1
Permeability	k	$0.0\ m^2$
Mean pressure (low)	P_m	$1\ MPa$
Bearing velocity (low)	U	$0.094\ m/s$
Mean pressure (high)	P_m	$10\ MPa$
Bearing velocity (high)	U	$0.94\ m/s$

ABAQUS simulation to that of the pressure profile (so that nodal pressures can be applied directly). At the fidelities needed for convergence of the solid mechanics, the Reynolds equation is appropriately converged as well. This is true for the low and high load situations. Therefore, the lateral mesh density required by the poromechanics is an appropriate mesh for the fluid mechanics as well. In the cases tested, the finite element grid is approximately twice as fine as is required by the discrete Reynolds equation. However, there is not an appreciable difference in the Reynolds equations solution times (course vs. fine); therefore, the Reynolds mesh is matched to the FEA mesh for convenience.

The effect of permeability is negligible to the results of the mesh convergence. Like the other inputs to the Reynolds equation, permeability changes the pressure in a fluid film; however, it does not influence the mesh convergence at a designated load or geometry. The loads tested herein are specific to the simulation parameters chosen for study. A mesh convergence study should always be re-preformed for pressures that deviate greatly from the examples shown.

Having the same spatial grid between the solid and fluid materials is advantageous when defining the loading and boundary conditions. This allows for solutions at the nodes of each simulation to be directly imposed and coupled. As discussed, the
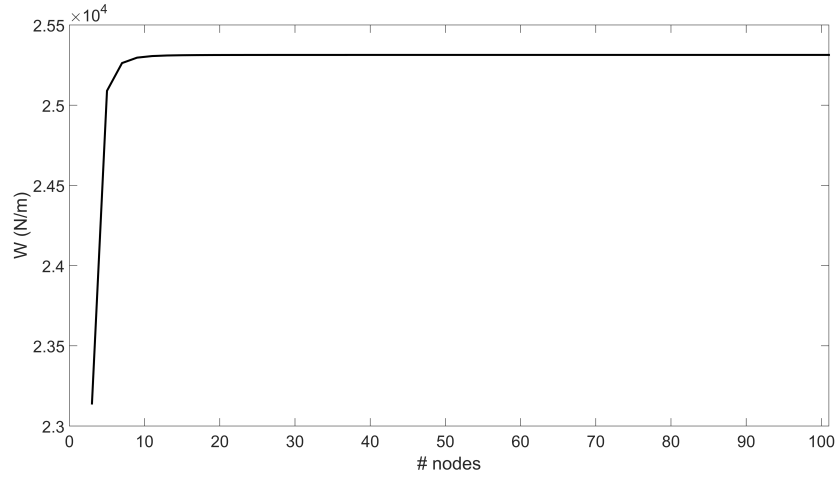
106

(a) Load support versus number of nodes
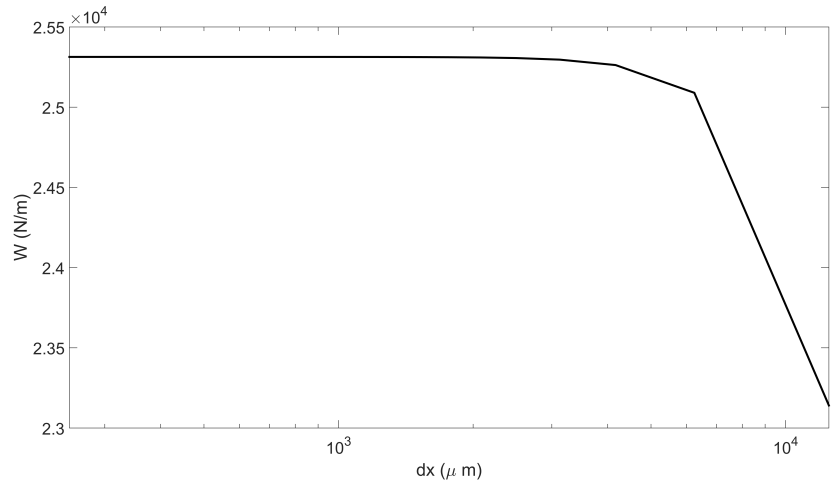
(b) Load support versus discrete step size
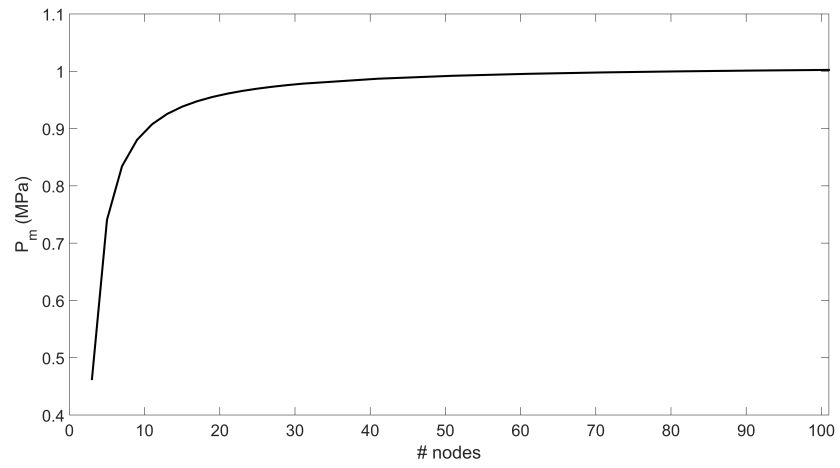
(c) Mean pressure versus number of nodes

Figure 45: Mesh convergence study of discrete Reynolds equation ($P_m = 1\ MPa$)
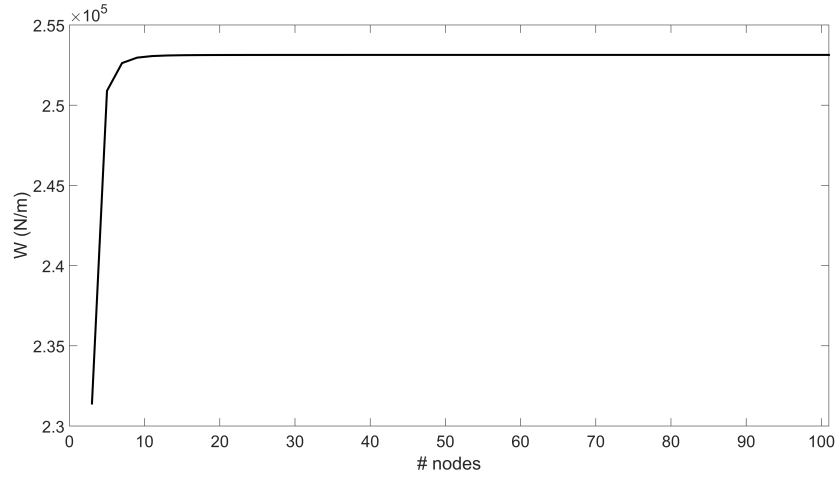
(a) Load support versus number of nodes
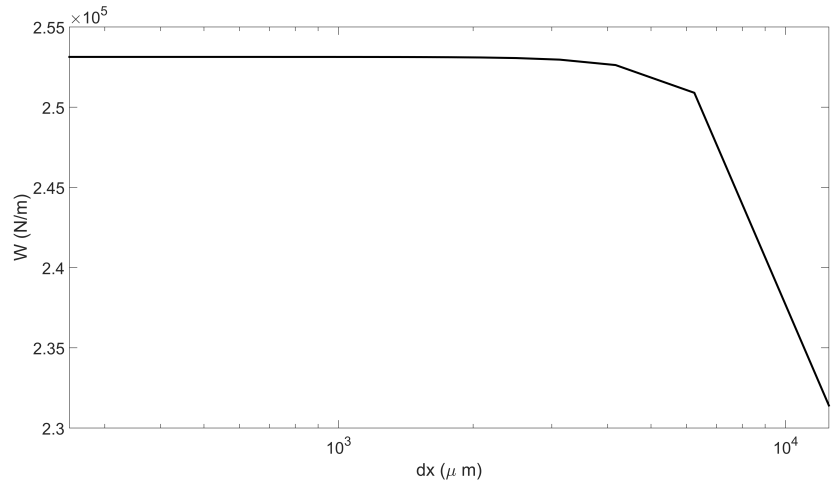
(b) Load support versus discrete step size
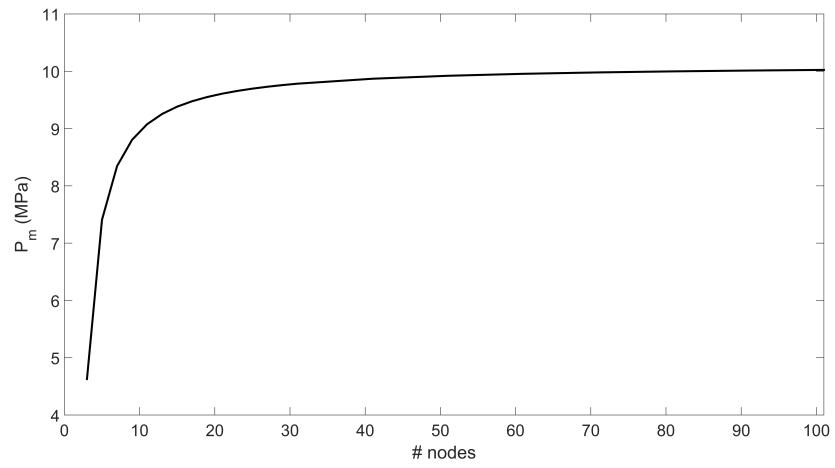
(c) Mean pressure versus number of nodes

Figure 46: Mesh convergence study of discrete Reynolds equation ($P_m = 10\ MPa$)

108

computational burden of solving the Reynolds equation is significantly smaller than that of the poroviscoelastic problem. Therefore, the grid used by ABAQUS will be the default grid for the fluid film solution as well. The pore pressure magnitudes and specified tolerances are the primary considerations for mesh convergence and simulation time in ABAQUS.

6.3.3   ABAQUS Mesh Optimization

The results of the mesh convergence study in Section 6.3.1 are useful for understanding the grid size needed to simulate PVE behavior subjected to a pore pressure load. However, the results are not optimized for simulation time. For instance, in areas of the substrate body where large pressure gradients are not present (e.g. near the impermeable boundary), the element sizes can be increased. The nature of the problem suggests that the top layer of elements is the most important; therefore, high fidelity meshes should be used in that area. However, significant computational savings occur with mesh optimization.

An example problem is posed to explore an optimized mesh design. Figure 47 shows three meshes with varying degrees of manipulation. The number of nodes on the top surface of the PVE pad is consistent for all meshes; however, the number of elements comprising the PVE pad is different, as given by Table 12. The mesh with square elements (Fig. 47a) is used as a benchmark. The results of an example simulation are compared to the benchmark for simulation time and results.

The nodes at the top of the PVE pad are the most significant for the current study, so results are shown with those points (Fig. 48). Figures 49 and 50 show the pore pressure and displacement in the PVE body. The local significance of the top edge of the PVE pad, where the HDL solution is coupled, allows for larger element sizes in the PVE body as you move away from the top edge. This means that mesh optimization can supply CPU time savings, especially if the simulation is extended

Table 12: Example mesh optimization parameters

Mesh	Elements	CPU Time (s)	Max Disp. (μm)
Square (Benchmark)	5000	196.20	1.01
Refined Mesh I	1609	69.7	1.01
Refined Mesh II	594	26.9	1.01

to three dimensions. The current study prioritizes the nodes nearest to the hydro-dynamic fluid load; however, if flow through the porous pad is important in future work, then the mesh optimization will be revisited.

6.4 Summary

The methods developed herein give equivalent solutions at steady-state. This is important for simulating the operating condition of a given triboelement. In addition, these techniques are useful for solving similar coupled-type problems. The mesh convergence study likewise gives guidelines for similar problems. In future work, mesh optimization may become a critical aspect of the solution technique if a full, 3D, simulation is performed. Rectangular elements are used to replicate the benchmark created herein. These elements can be optimized accordingly in future studies. In the following chapter, the Method II will be used to obtain the transient properties of storage and loss.
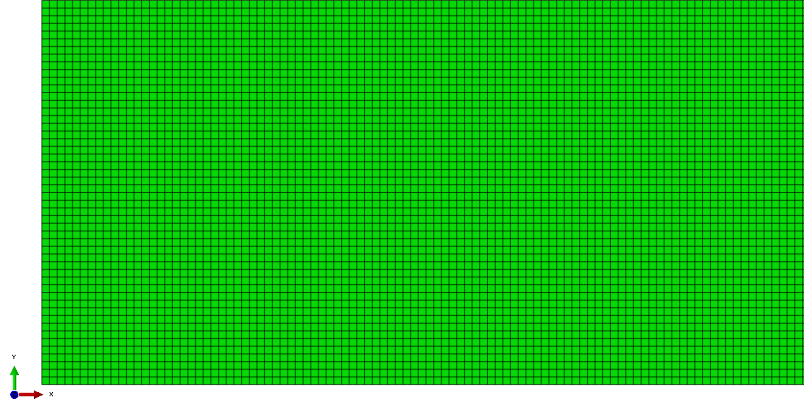
(a) Benchmark mesh of PVE pad
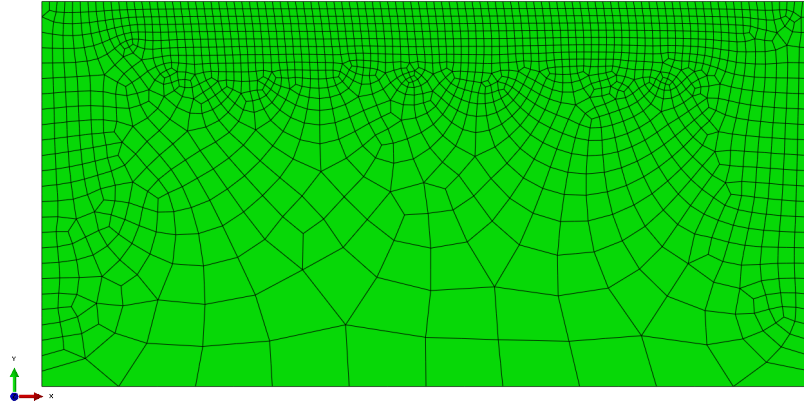
(b) Refined mesh I of PVE pad
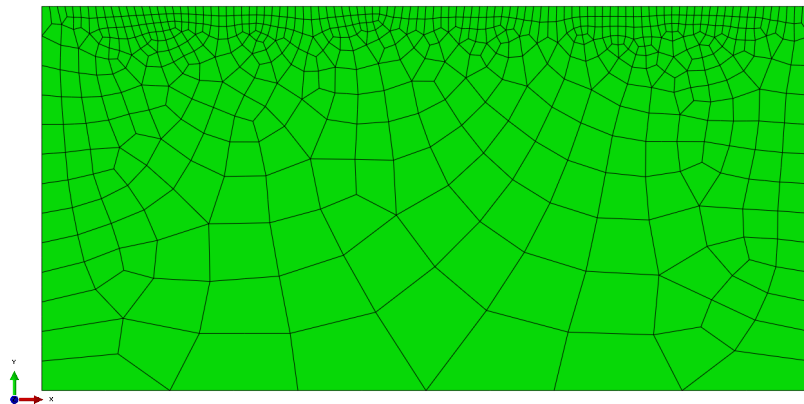
(c) Refined mesh II of PVE pad

Figure 47: Meshes used in optimization study
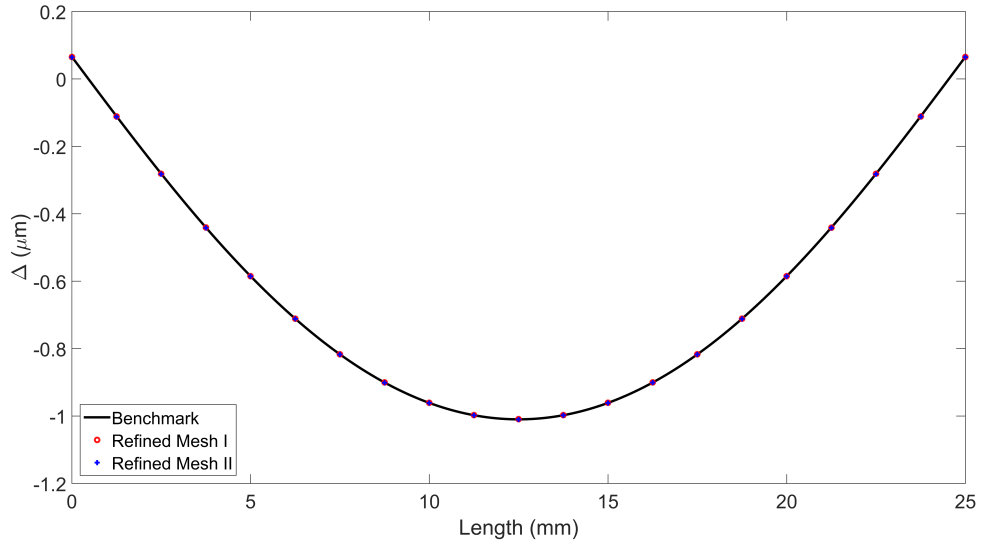
(a) Deformation at top edge of PVE pad
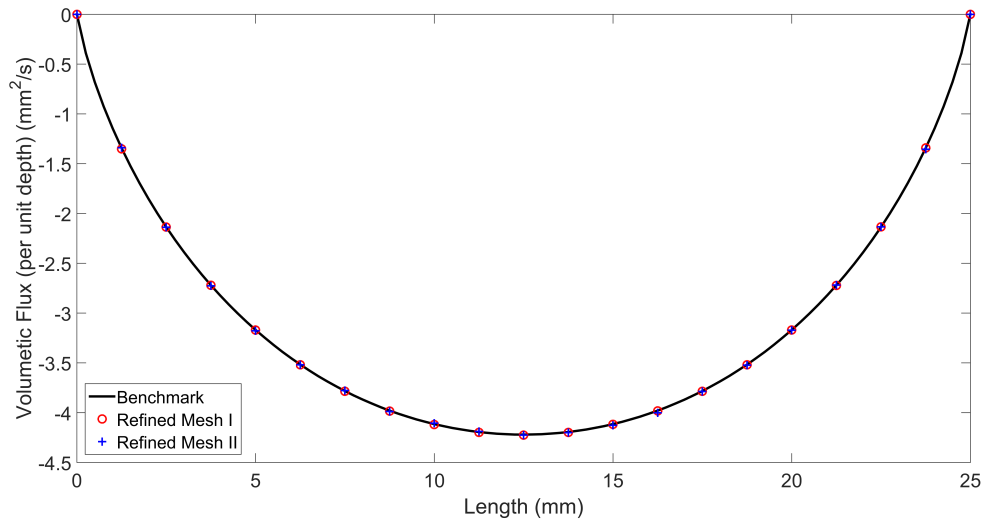
(b) Reaction volumetric flux (per unit depth)

Figure 48: Comparison of mesh optimization(s) to benchmark for important metrics at the top edge of the PVE pad

(a) Pore pressure in benchmark mesh of PVE pad

(b) Pore pressure in optimized mesh of PVE pad

(c) Pore pressure in finely optimized mesh of PVE pad
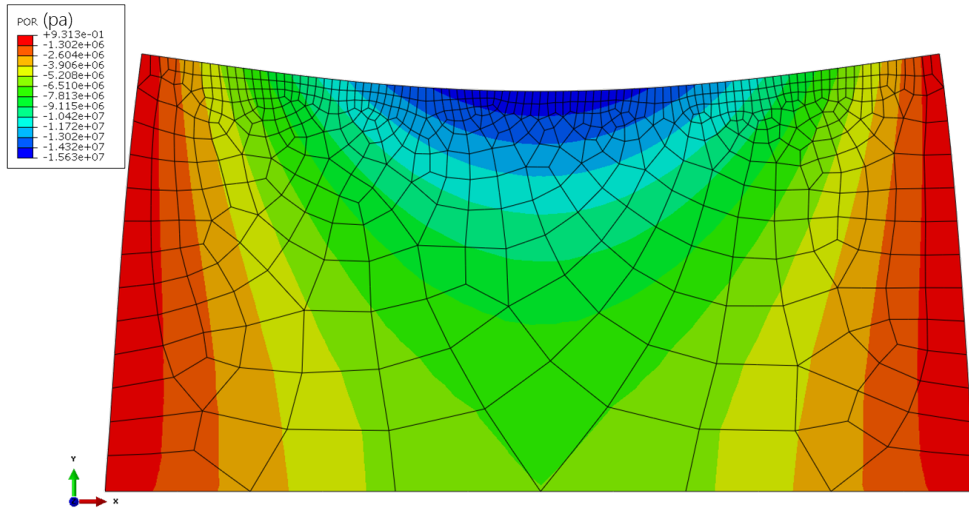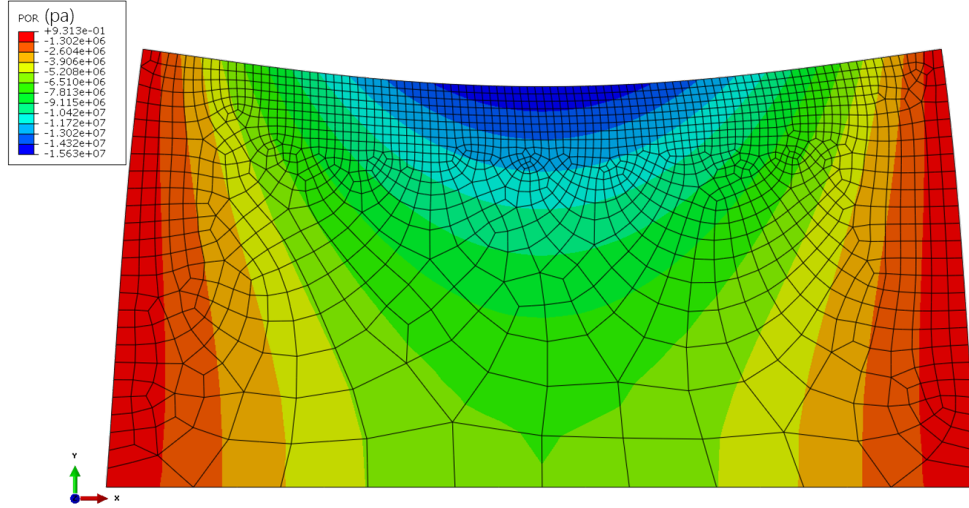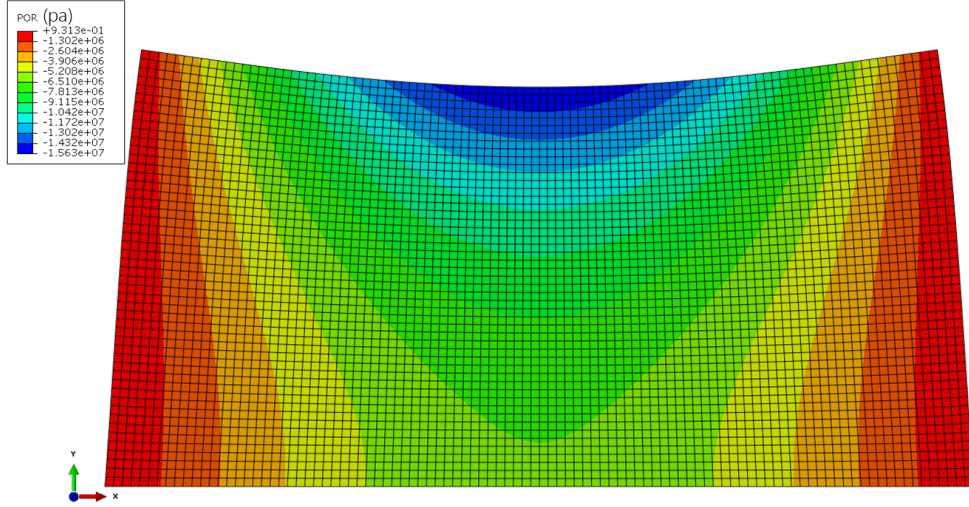
Figure 49: Pore pressure in the PVE pad
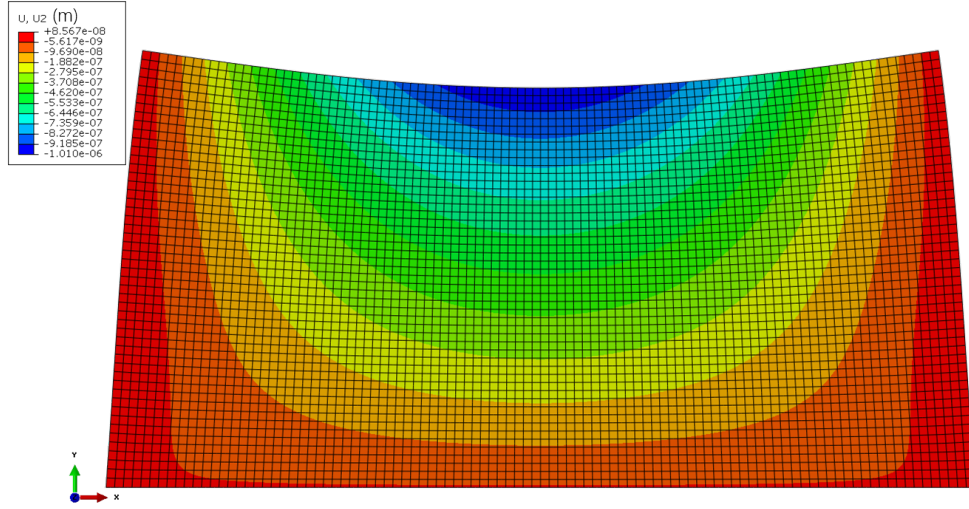
(a) Deformation in benchmark mesh
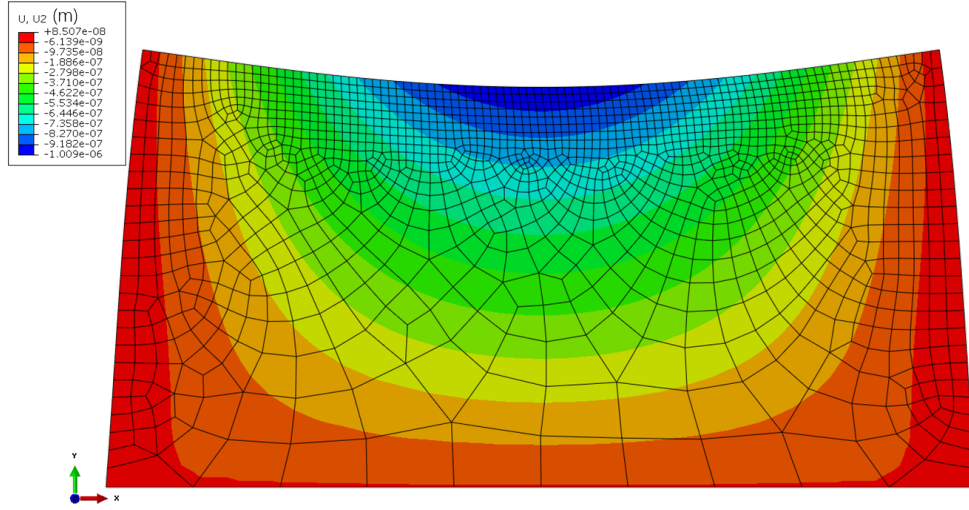
(b) Deformation in optimized mesh
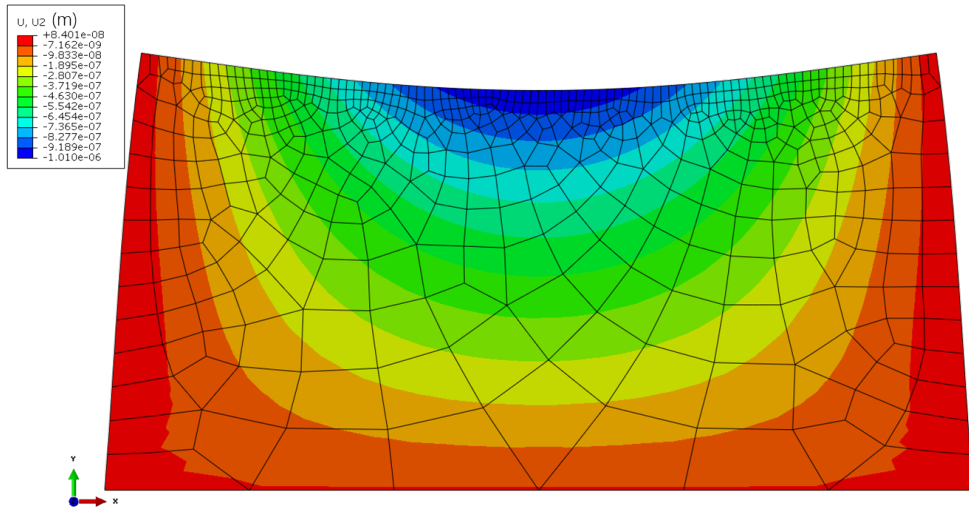
(c) Deformation in finely optimized mesh

Figure 50: Deformation in the PVE pad (magnified for clarity)

114

CHAPTER VII

APPLICATION OF MODEL TO DETERMINE DYNAMIC PROPERTIES

The preceding chapters provide the necessary prerequisites for building a coupled PVE/HDL simulation. What remains is to simulate example problems, and make comparisons between the traditional rigid case and PVE/HDL case. A number of loading and boundary conditions will be discussed herein. First, the simulations will be compared at steady-state, and then the transient behavior will be assessed.

7.1 Test Configurations

Two cases are proposed to explore the performance of triboelements with flexible/porous interfaces. A thrust bearing, like that of Fig. 30, is analyzed in a "long bearing" configuration (corresponding to plane strain in the poromechanics). The geometry and specifications of the problem are given in Table 13 (the fractional calculus parameters are retained from Table 6). Each case has identical geometric and tribological characteristics. The difference between the cases are the boundary conditions.

The first case is "glued" at the lateral edges ($x = 0$ and $x = L$) of the PVE pad. In this application, glued means that the PVE pad is fixed at the edges, and no strain occurs at the boundary. However, fluid is still allowed to permeate across the porous boundary. Figure 51 shows the boundary conditions imposed on the porous pad. Assuming a submerged bearing, the leading and trailing edges of the pad are exposed to atmospheric pressure (gauge), which allows fluid flow across the boundary. The bottom boundary is fixed and rigid, and the top boundary is flexible and the

Table 13: Parameters for PVE/HDL analysis

Parameter	Symbol	Value (units)
Permeability	k	$10^{-14} \ (m^2)$
Load per depth	W	600 (N/m)
PVE pad length	L	25 (mm)
PVE pad height	H	6.25 (mm)
Bearing velocity	U_1	0.02 (m/s)
Fluid viscosity	μ	0.1 $(Pa \cdot s)$
Slip coefficient	α	0.1
Inlet film thickness (if fixed)	h_i	40 (μm)
Film thickness ratio (if fixed)	a	2.2
Fractional elastic modulus	E_0	2 (MPa)
Fractional elastic modulus	E_1	1 (MPa)
Fractional dissipative constant	λ_n	1 $(s^{-1/2})$
Poisson's ratio	ν	0.30

pressure, p, is equal to the fluid film pressure, P. The pressure gradient in the porous pad facilitates fluid flow throughout the pad. The pressure boundary and initial conditions are defined mathematically:

$$p(0, y, t) = p(L, y, t) = 0 \tag{166}$$

$$\frac{\partial p}{\partial y}(x, -H, t) = 0 \tag{167}$$

$$p(x, 0, t) = P(x, 0, t) \tag{168}$$

$$p(x, y, 0) = 0 \tag{169}$$

$$\epsilon_x(0, y, t) = \epsilon_x(L, y, t) = 0 \tag{170}$$

$$\epsilon_y(0, y, t) = \epsilon_y(L, y, t) = 0 \tag{171}$$

$$\epsilon_x(x, -H, t) = \epsilon_y(x, -H, t) = 0 \tag{172}$$

$$\sigma_x(x, 0, t) = 0 \tag{173}$$

$$\sigma_y(x, 0, t) = -P(x, 0, t) \tag{174}$$

$$\sigma_x(x, y, 0) = \sigma_y(x, y, 0) = 0 \tag{175}$$

Equations 166-168 enforce the fluid pressure boundary conditions, while Eqs. 170-174 are placed on the solid matrix. Equation 167 enforces no flow across the rigid boundary at $y = -H$. Figure 51a shows the boundaries where flow exists, and these values are determined from the fluid pressure gradients. Pressure boundary conditions are enforced to maintain continuity with the HDL solution from the Reynolds equation.

The second case is not glued at the lateral edges ($x = 0$ and $x = L$), shown in Fig. 52; however, strains in the x-direction are restricted. This means that the PVE pad can deform in the y-direction at the boundaries $x = 0$ and $x = L$, but not laterally. Mathematically, the boundary and initial conditions are:
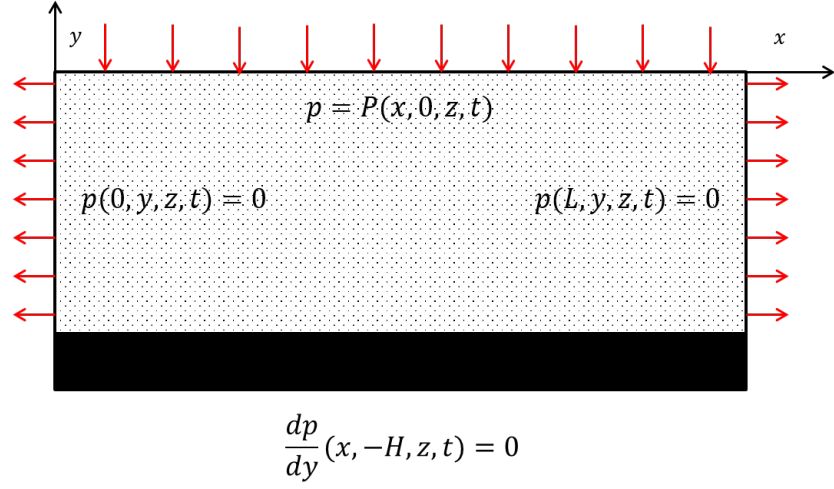
$$p = P(x, 0, z, t)$$

$$p(0, y, z, t) = 0 \qquad p(L, y, z, t) = 0$$

$$\frac{dp}{dy}(x, -H, z, t) = 0$$

(a) Fluid pressure boundary conditions on the PVE pad

$$\sigma_y(x, 0, z, t) = -P(x, 0, z, t)$$

$$\sigma_x(x, 0, z, t) = 0$$

$$\epsilon_x(0, y, z, t) = 0 \qquad \epsilon_x(L, y, z, t) = 0$$
$$\epsilon_y(0, y, z, t) = 0 \qquad \epsilon_y(L, y, z, t) = 0$$

$$\epsilon_x(x, -H, z, t) = 0$$
$$\epsilon_y(x, -H, z, t) = 0$$
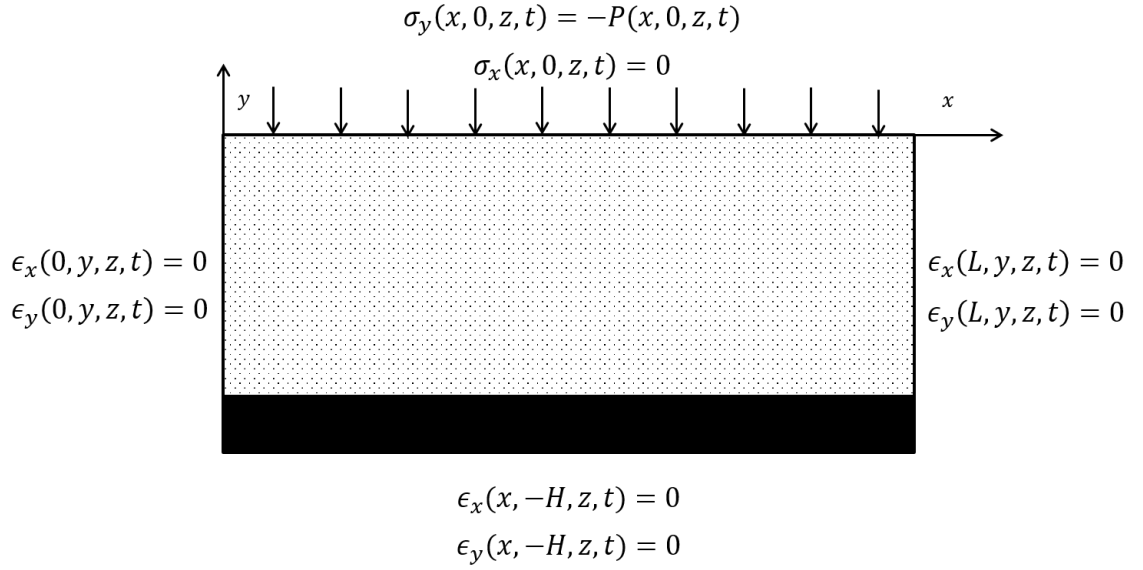
(b) Solid boundary conditions on the PVE pad

Figure 51: Fluid and solid boundary conditions on porous pad (Case I)

$$p(0, y, t) = p(L, y, t) = 0 \tag{176}$$

$$\frac{\partial p}{\partial y}(x, -H, t) = 0 \tag{177}$$

$$p(x, 0, t) = P(x, 0, t) \tag{178}$$

$$p(x, y, 0) = 0 \tag{179}$$

$$\epsilon_x(0, y, t) = \epsilon_x(L, y, t) = 0 \tag{180}$$

$$\epsilon_x(x, -H, t) = \epsilon_y(x, -H, t) = 0 \tag{181}$$

$$\sigma_x(x, 0, t) = 0 \tag{182}$$

$$\sigma_y(x, 0, t) = -P(x, 0, t) \tag{183}$$

$$\sigma_x(x, y, 0) = \sigma_y(x, y, 0) = 0 \tag{184}$$

Both cases are solved with "Method I" developed in Chapter 6. The 2D (x,y) case is used as test bed and to explore the physics of this coupled system. Additional simplifications are made to the solution routine: shear loads on the porous pad (from the fluid film) are neglected, and the nodal points of the HDL problem remain evenly spaced. Testing indicates that shear stresses (tractions on the porous body) are small compared to the normal stresses (approximately 1-2%). Shear stresses also do not create volumetric changes, so the pore pressure in the PVE body does not change due to shearing action. Therefore, these stresses are neglected for the time being. The cases are solved in time until a steady-state is obtained.

7.2 Results at Steady-State

The paths to steady state for Case I and Case II are shown in Figs. 53 and 54, respectively. Both cases have equivalent loads and starting configurations; however, the steady-state is for each case is qualitatively and quantitatively different. Table
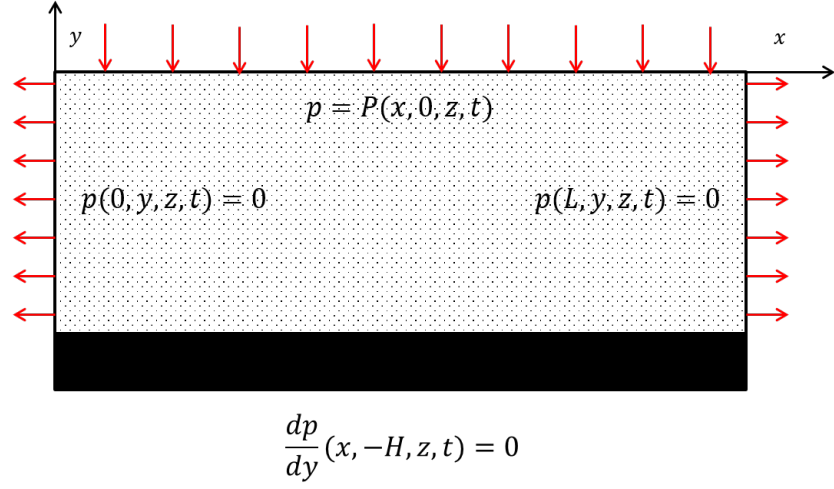
$$p = P(x, 0, z, t)$$

$$p(0, y, z, t) = 0 \qquad p(L, y, z, t) = 0$$

$$\frac{dp}{dy}(x, -H, z, t) = 0$$

(a) Fluid pressure boundary conditions on the PVE pad

$$\sigma_y(x, 0, z, t) = -P(x, 0, z, t)$$

$$\sigma_x(x, 0, z, t) = 0$$

$$\epsilon_x(0, y, z, t) = 0 \qquad \epsilon_x(L, y, z, t) = 0$$

$$\epsilon_x(x, -H, z, t) = 0$$

$$\epsilon_y(x, -H, z, t) = 0$$
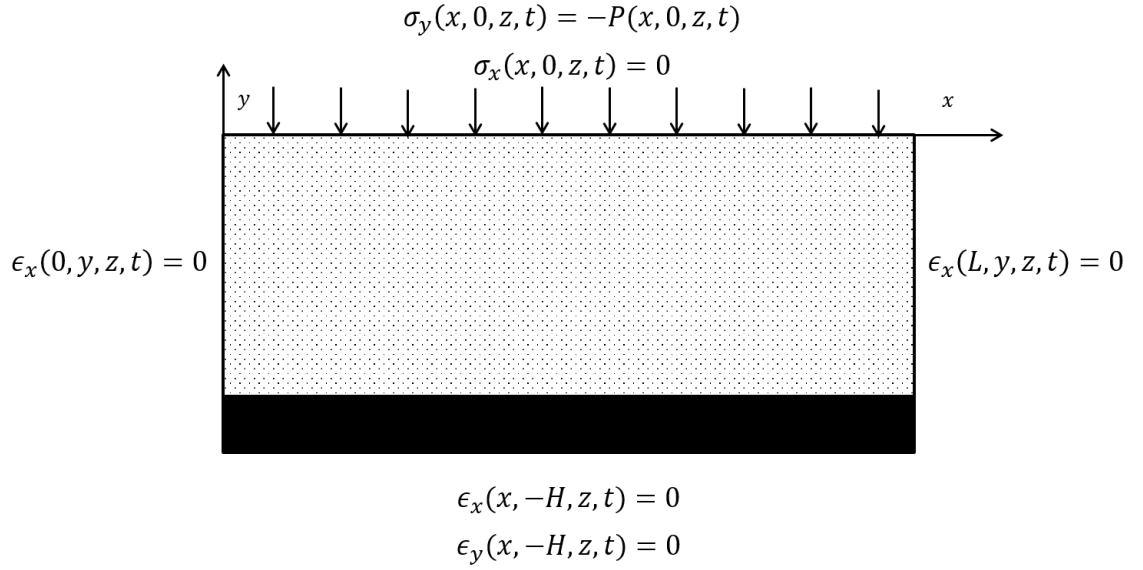
(b) Solid boundary conditions on the PVE pad

Figure 52: Fluid and solid boundary conditions on porous pad (Case II)

Table 14: Results from the simulations in Fig. 55

Case	Parameter	Value
Rigid	h_i	40.2 μm
	h_o	18.3 μm
	P_{max}	38.3 kPa
	U_y	0
Case I	h_i	36.3 μm
	h_o	14.5 μm
	P_{max}	36.6 kPa
	U_y	0.0068 mm^2/s
Case II	h_i	33.3 μm
	h_o	15.5 μm
	P_{max}	36.5 kPa
	U_y	0.0062 mm^2/s

14 contains information about the steady-state pressure profiles and film thicknesses for each case.

At steady-state, the system transients have been expended; therefore, no additional consolidation and viscoelastic dissipation is occurring. During the simulation to steady-state, the film profile and corresponding pressure profile in the bearing are tracked in time. Initially, the porous pad is undeformed. As the porous and viscoelastic mechanisms respond to a HDL load, deformation occurs. In a viscoelastic sense, this relates to the transition from the glassy ($t = 0_+$) to rubbery modulus ($t = \infty$). The pressure profiles also evolve in time, as the maximum pressure increases and changes lateral location in the bearing. The time-dependent action of the bearing gives storage and loss character in the frequency domain as well [2, 69].

The flexible/porous cases are compared to the rigid case as performance benchmarks. The flexible/porous film thickness is smaller than its rigid counterpart. Considering the porous Reynolds equation (Eq. 159), the V_0 term acts in opposition to the "wedge" term; therefore, the film thickness must be reduced to sustain an equivalent load in the porous case. The permeability of the porous pad strongly influences this effect, and must be carefully designed with the desired application.
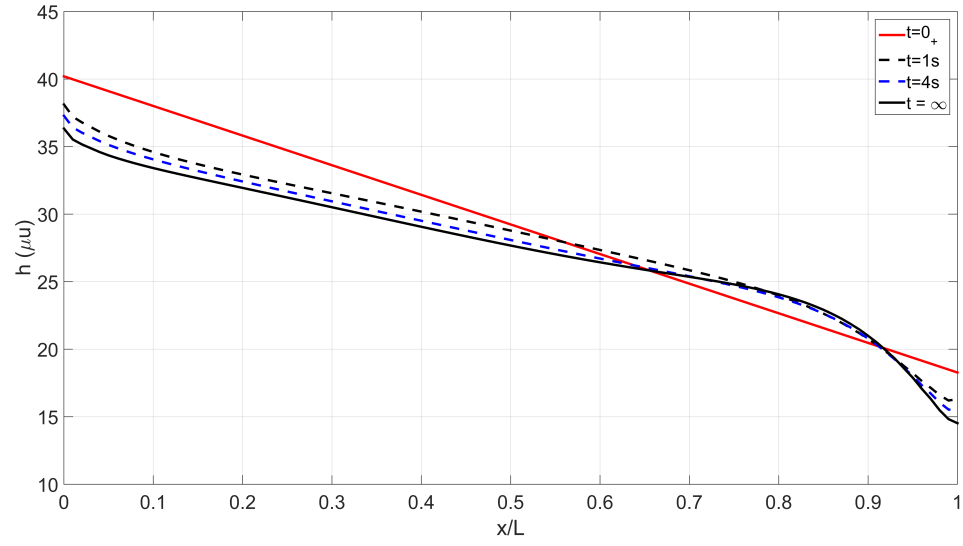
(a) Film thickness over time
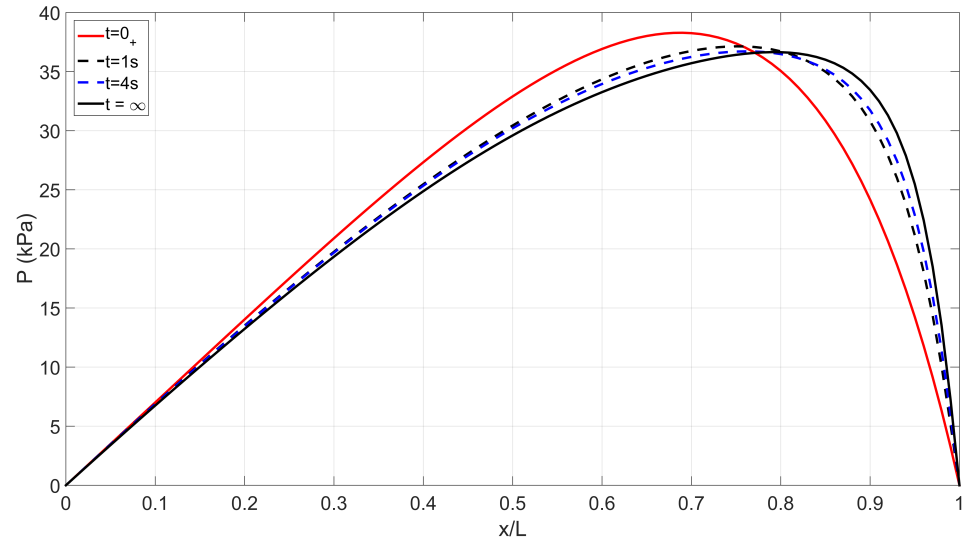
(b) Pressure profile over time

Figure 53: Film thickness and pressure profile evolution with time (Case I)
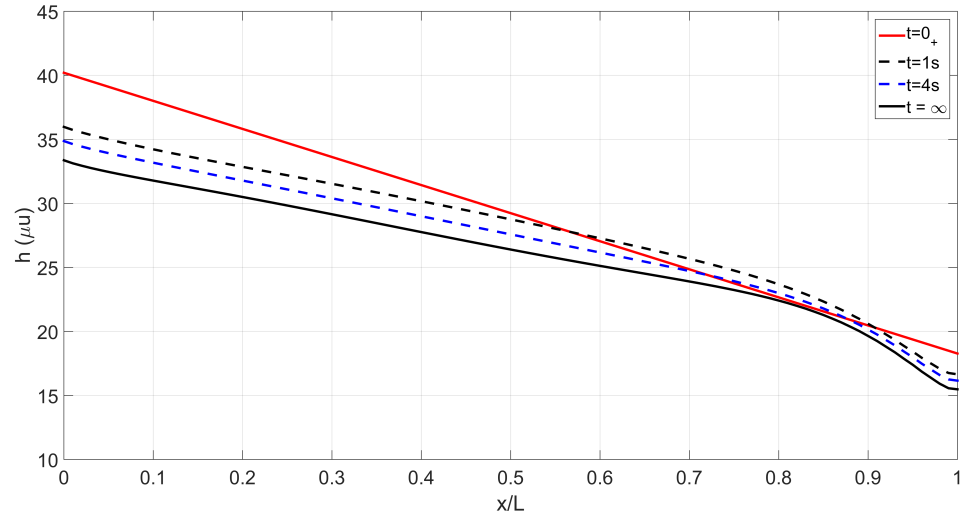
(a) Film thickness over time
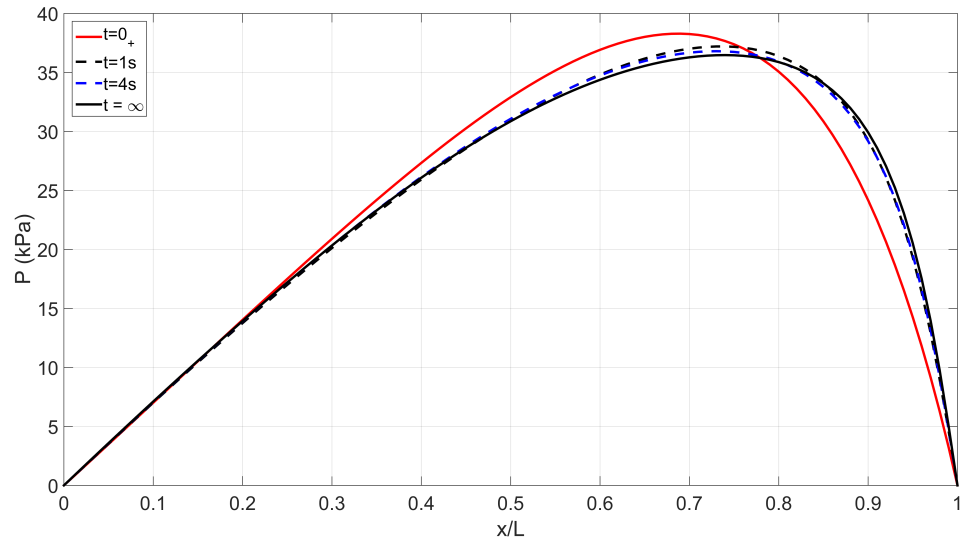
(b) Pressure profile over time

Figure 54: Film thickness and pressure profile evolution with time (Case II)

The comparisons shown in Fig. 55 as $t \to \infty$ indicate that the flexible/porous cases are different than the rigid case in a realizable way. The flexible/porous interface influences the location of the center of pressure, and the amount of fluid flow that crosses the porous interface. At the same time, the flexible/porous case is still capable of supporting loads in the vicinity of what the completely rigid case can support. Therefore, the additional capacities of the flexible/porous bearing design will be considered in relation to the rigid case. In particular, the dynamic storage and loss properties are sought for the flexible/porous configurations.

7.2.1 Pressure in the Porous Pad

Within the PVE pad, the pressure is highest at the film interface, and decays throughout the body to the zero pressure boundaries. The lower, rigid interface also experiences a pressure load from the fluid in the body. Figure 57 shows the pressure in the body for Case I and Case II.

7.3 Determination of Storage and Loss

The steady-state solution of the coupled PVE/HDL problem gives insight into the operational configuration of a flexible/porous bearing. These solutions indicate that the PVE/HDL combination is possible in a tribological application; however, the benefit of such a configuration is unproven. A hypothesized advantage of the flexible/porous case is its dynamic response to a change in operating conditions. In particular, the properties of storage and loss are of interest. Therefore, a model that yields these properties is developed.
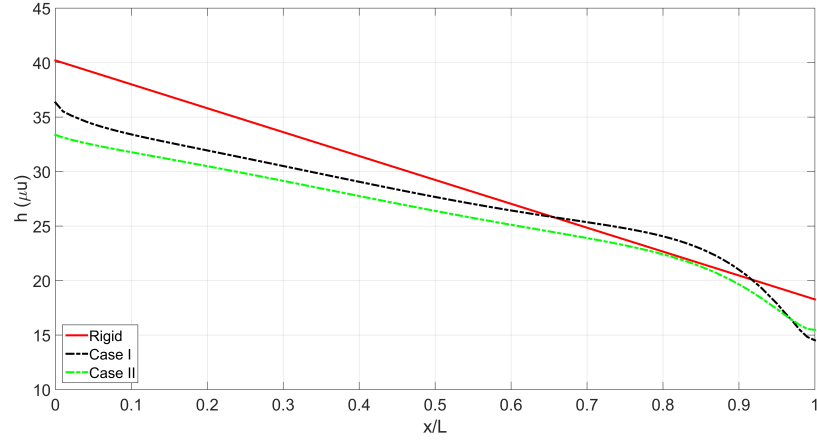
(a) Comparison of film thickness required to sustain load ($t \to \infty$)
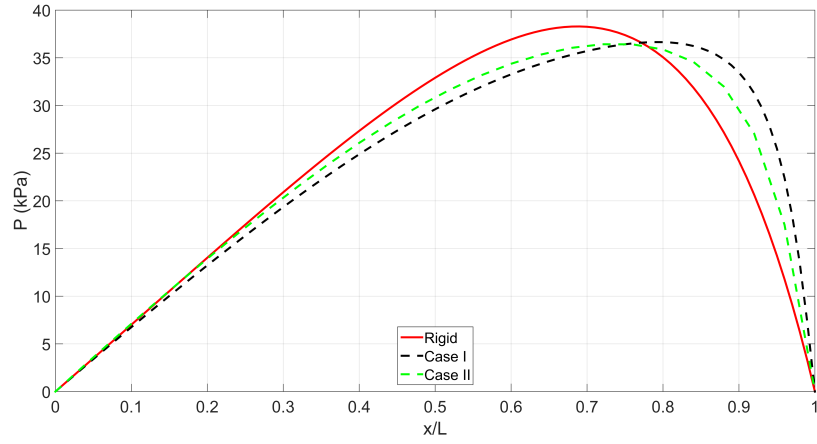
(b) Pressure profile obtained from above film profile
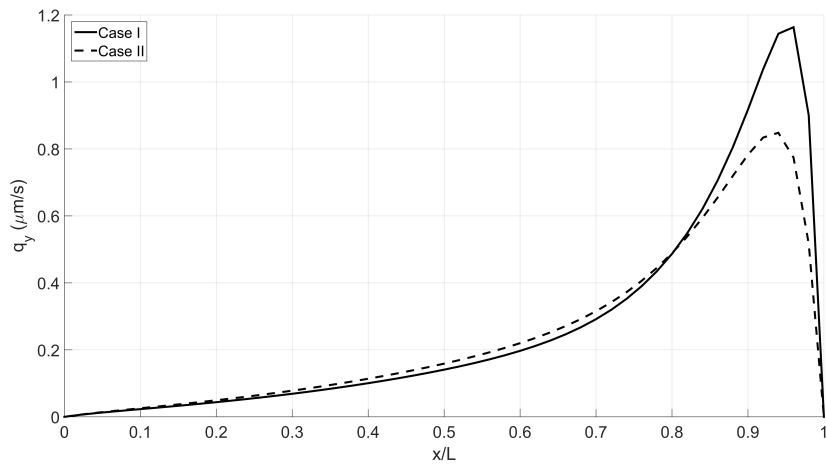
(c) Normalized flow in the rigid/porous and flexible porous cases

Figure 55: Comparison of rigid, rigid/porous, and flexible pad designs at $t \to \infty$
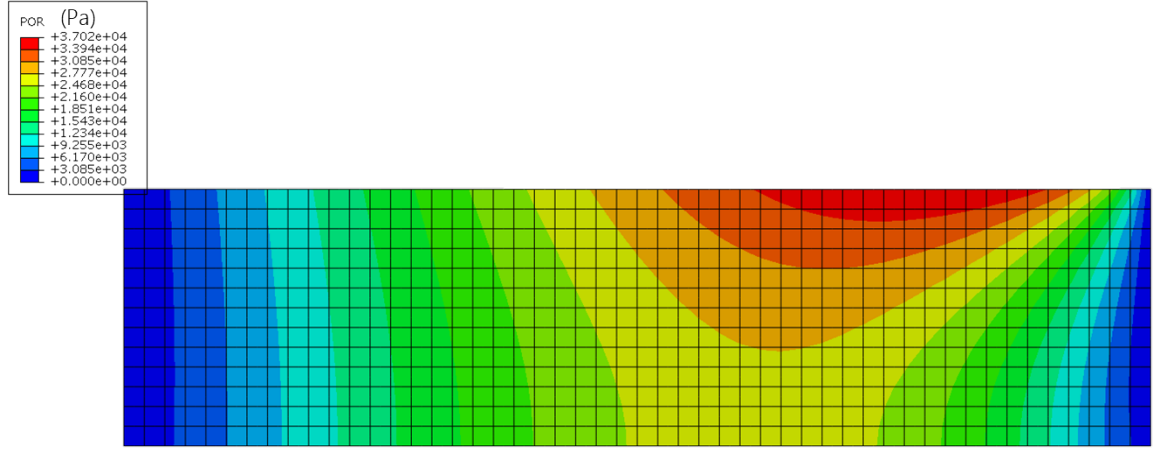
(a) Pore pressure in the porous pad for Case I
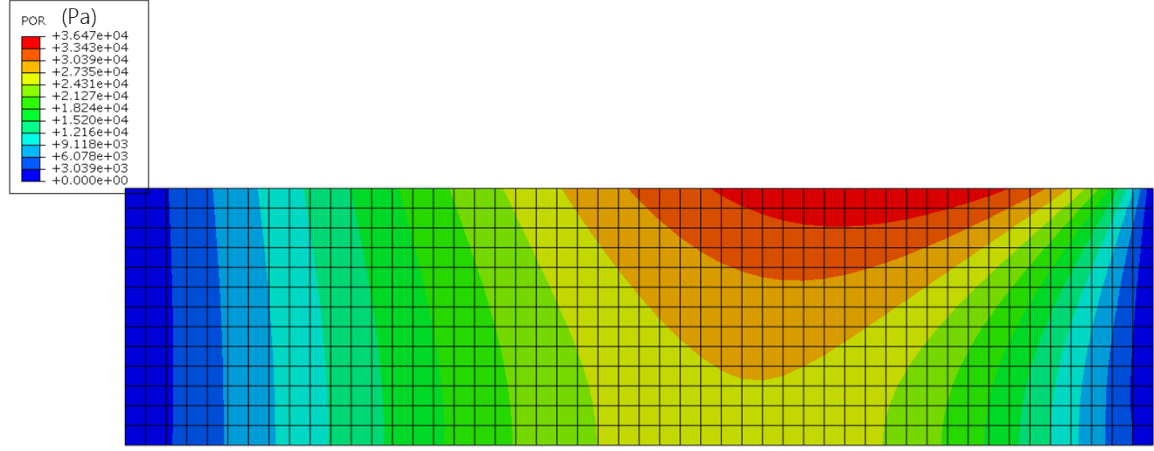
(b) Pore pressure in the porous pad for Case II

Figure 56: Comparison of pore pressure in PVE pad for Cases I and II at steady-state $(t \to \infty)$
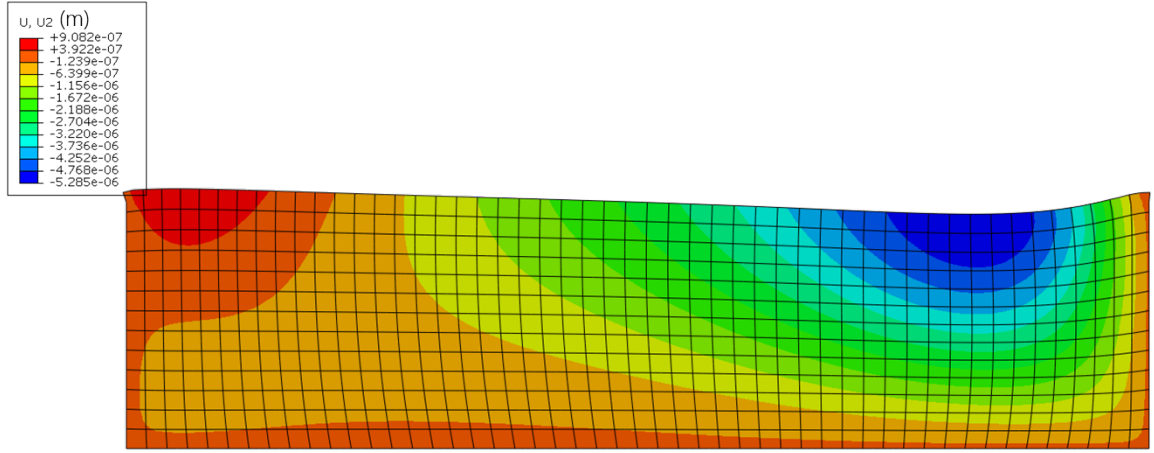
(a) Deformation in the porous pad for Case I
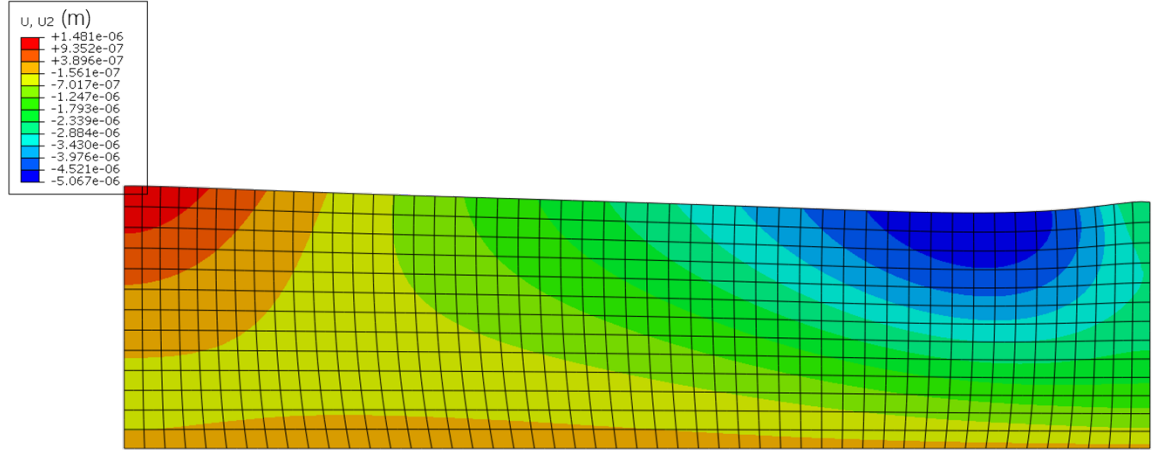
(b) Deformation in the porous pad for Case II

Figure 57: Comparison of PVE pad deformation (magnified) Cases I and II at steady-state ($t \to \infty$)

7.3.1 Correspondence Principle

Following the techniques of Miller and Green [101, 102] for gas film bearings, a correspondence principle is introduced for coupled PVE/HDL problems. The correspondence principle follows the techniques highlighted in Chapter 3 for a viscoelastic material. Retaining the convolution integral from linear viscoelasticity, a force/displacement relationship is proposed:

$$F\left(t\right) = D\left(0\right) K\left(t\right) + \int_0^t \dot{D}\left(\tau\right) K\left(t - \tau\right) \, \mathrm{d}\tau, \tag{185}$$

and

$$D\left(t\right) = F\left(0\right) C\left(t\right) + \int_0^t \dot{F}\left(\tau\right) C\left(t - \tau\right) \, \mathrm{d}\tau. \tag{186}$$

In Eqs. 185 and 186, $F(t)$ is force, $D(t)$ is displacement, $K(t)$ is the stiffness modulus, and $C(t)$ is the compliance modulus. The stiffness and compliance moduli are analogous to the relaxation and creep moduli, respectively. Equations 185 and 186 are analogous to the stress/strain relationships given for linear viscoelasticity (Eqs. 1-2), where stress is translated to force, and strain to displacement.

The physical significance of Eqs. 185 and 186 is that the storage and loss characteristics of a system are obtained with a single experiment, either by controlling load support or film thickness. This is done by imposing an instantaneous displacement in the film thickness and tracking the corresponding load support over time, or imposing an instantaneous change in load support and tracking the change in film thickness. The correspondence principle gives a mechanical impedance, from which storage and loss are found.

In the current study, the fluid and solid are considered incompressible; therefore, an instantaneous displacement is impossible for the proposed cases (that are laterally constrained). This dictates that a relaxation experiment is not ideally suited to determine the storage and loss of the coupled PVE/HDL simulation. Realistically, a

sufficiently fast displacement may be imposed on the body in order to simulate relaxation. However, the alternative to relaxation is creep, which is physically possible in the model. Here, a change in the load support is imposed, and the corresponding film thickness required to sustain this load is determined. Utilizing creep is a departure from the work of Miller and Green [101, 102], who studied gas film lubrication. Miller and Green imposed an instantaneous displacement on the gas film because the gas is compressible, and the equation of state for the ideal gas law allows for pressure calculations at $t = t_0$. This is not possible in the HDL/PVE case.

7.3.2 Mechanical Impedance

Equation 185 relates force $(F(t))$, displacement $(D(t))$, and stiffness $(K(t))$ in the time-domain. Using the same method as the elastic-viscoelastic correspondence principle, a simple expression is generated in the Laplace domain:

$$F(s) = sK(s)D(s). \tag{187}$$

Analogous to the complex modulus from viscoelasticity, $sK(s)$ is effectively a spring in the Laplace domain. Transferring from the Laplace domain to the frequency domain, $sK(s)$ has real and imaginary components:

$$K^*(\omega) = (i\omega)K(\omega) = K'(\omega) + iK''(\omega) \tag{188}$$

The real part (K') is defined as the storage and the imaginary part (K'') as the loss. These properties are used to compare the PVE/HDL and rigid cases. For the current work, storage and loss are the critical metrics used to assess performance. In future work, other performance characteristics are considered.

7.3.3 Mechanical Impedance Models

To determine the mechanical impedance of the coupled PVE/HDL problem, a creep-like experiment is performed. First, the bearing is simulated to steady-state. Then,

from steady-state, the load support is perturbed and held, and the bearing's resulting travel is tracked. This creates a time-dependent force/displacement relationship. The force/displacement relationship is either translated into the frequency domain to determine storage and loss, or fit in the time-domain with a constitutive model. Using a known constitutive model is advantageous because it provides fit parameters that can be easily compared between configurations and simulations, and there are often direct correlations between the time-domain fit and the frequency domain storage and loss moduli.

There is an analogous relationship between mechanical impedance and the complex modulus from viscoelasticity. Therefore, the spring-dashpot and fractional models used in viscoelasticity can also model the force/displacement relationship. While the relaxation modulus is primary considered in the definition of viscoelasticity, the mechanical impedance is determined from a creep-like test. An integer-order and fractional model are proposed as suitable models. The integer-order model is the well known Kelvin-Voigt model, shown in Fig. 58a. The fractional model emulates the Kelvin-Voigt model, replacing the dashpot with a fractional spring-pot of order α (Fig. 58b). The compliance of the Kelvin-Voigt model is [52]:

$$C(t) = \frac{1}{K} \left[1 - e^{-t/\tau} \right], \tag{189}$$

where the time constant, τ, relates the model parameters K and η:

$$\tau = \frac{\eta}{K}. \tag{190}$$

The compliance of the fractional Kelvin-Voigt model is [52]:

$$C(t) = \frac{1}{K} \left\{ 1 - E_\alpha \left[- \left(\frac{t}{\nu} \right)^\alpha \right] \right\}, \tag{191}$$

where ν relates the model parameters K and β:

$$\nu = \frac{\beta}{K}, \tag{192}$$

130

(a) Kelvin-Voigt viscoelastic model

(b) Fractional representation of the Kelvin-Voigt viscoelastic model
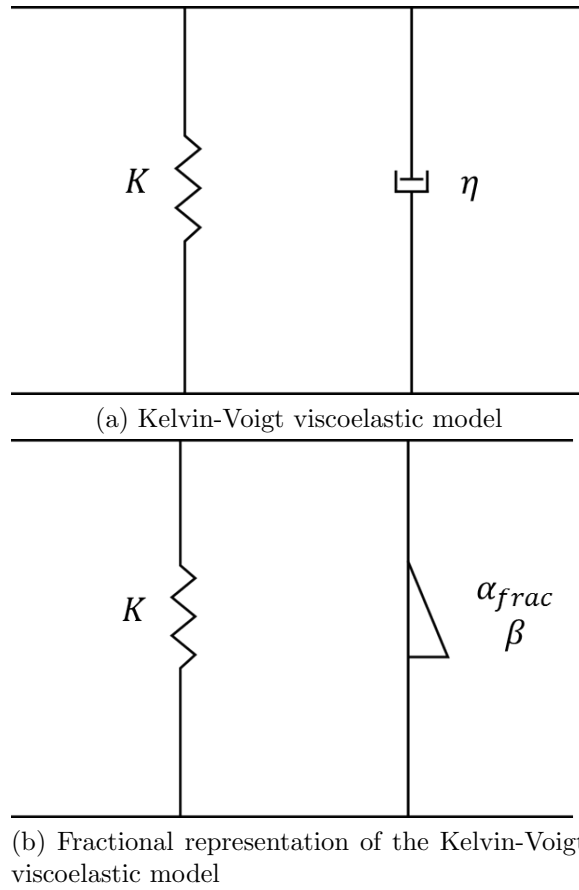
Figure 58: Mechanical analogy for the compliance models used to determine force/ displacement relationship

and takes the units of seconds (s). When $\alpha = 1$, the fractional calculus model reverts to the Kelvin-Voigt model, and when $\alpha = 1/2$, the complementary error function reappears. The integer-order and fractional models are capable of a creep-like behavior (fixed load with changing displacement), while incapable of stress-relaxation like behavior (instantaneous displacement is not possible). This mimics the physics of the coupled simulation with incompressible constituents. The models can be generalized by stacking additional elements in series [52]:

$$C(t) = \sum_{n=0}^{\infty} \frac{1}{K_n} \left\{ 1 - E_{\alpha_n} \left[- \left(\frac{t}{\nu_n} \right)^{\alpha_n} \right] \right\}. \tag{193}$$

The constitutive model for compliance is related to $sK(s)$ as follows:

$$sK(s) = \frac{1}{sC(s)}, \tag{194}$$

which leads to storage and loss in the frequency domain:

$$i\omega K(\omega) = K^*(\omega) = \frac{1}{i\omega C(\omega)}. \tag{195}$$

Equation 193 is converted from the time domain to the Laplace domain:

$$C(s) = \sum_{n=0}^{\infty} \frac{1}{K_n} \left[\frac{1}{s} - \left(\frac{1}{s(1 + a_n s^{\alpha_n})} \right) \right], \tag{196}$$

with

$$a_n = \left(\frac{1}{\nu_n} \right)^{\alpha_n}. \tag{197}$$

$sC(s)$ is then:

$$sC(s) = \sum_{n=0}^{\infty} \frac{1}{K_n} \left[1 - \frac{1}{(1 + a_n s^{\alpha_n})} \right]. \tag{198}$$

From Eq. 194 and Eq. 198, the storage and loss properties of the coupled PVE/HDL system are expediently obtained from the compliance data. The physics of the integer and fractional Kelvin-Voigt models suggests that the storage and loss values trend to infinity at high frequencies. This is consistent with the coupled HDL/PVE problem, in that an instantaneous displacement ($\omega \to \infty$) is not possible in the system. If

compressibility is allowed, or the solid is not confined as described above, the storage and loss values will not approach infinity as $\omega \to \infty$.

Compared to the rigid case, the flexible interface of the poroviscoelastic pad poses a unique challenge in the description of the film profile because of deformation. In the rigid case, the film profile can be determined by knowing the initial geometry and one point along the bearing's interface. For the flexible case, it is not sufficient to know the coordinates of a single point in the film, as the deformation of the porous pad dictates the film thickness. Therefore, some ambiguity exists in describing the time-history of the film thickness. For the purposes of the current work, the bearing's location at steady-state serves as "zero" (see Fig. 59). A point on the bearing is chosen as the tracking point, and all displacements are measured relative to this position. The displacement, $D(t)$, is the magnitude of the bearing's response from steady-state:

$$D(t) = |d(t) - d(t_0)|, \tag{199}$$

and recalling that steady-steady is defined as $d(t_0) = 0$:

$$D(t) = |d(t)|. \tag{200}$$

This definition of displacement is a "triboelement centric" view of the system dynamics, and it serves as a platform for comparing the different cases. The aforementioned models are fit to the displacement time history when subjected to a set load perturbation. From the fit, analytical expressions exist to determine the mechanical impedance in the Laplace domain, leading to the properties of storage and loss in the frequency domain.

7.4   Dynamic Storage and Loss

In order to obtain a transient response in the coupled PVE/HDL problem, a perturbation in the load support is introduced. This occurs from steady state, and is equivalent to a weight being added to the bearing at time $t = t_0$. The magnitude of
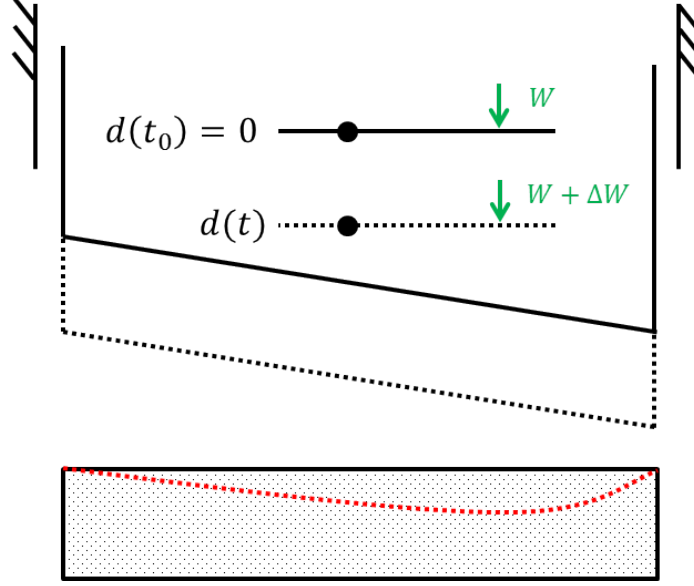
Figure 59: Tracking bearing's path after added load

the fluid film's response is tracked in time, as shown in Fig. 60. The information in Fig. 60 gives displacement of the bearing versus time for a known incremental load. The compliance modulus is fit to this data. With the compliance modulus, the dynamic properties of storage and loss are obtained. A number of cases are explored herein to understand the dynamic effects of the porous and viscoelastic contributions.

7.4.1   Rigid and Impermeable Case

The rigid and impermeable case is a benchmark example, and is given for comparison purposes. The displacement path is shown in Fig. 61a is fit with the fractional calculus Kelvin-Voigt model. The fit parameters are given in Table 15, and the frequency dependent storage and loss properties are shown in Fig. 61b. For the rigid case, the fractional derivative is nearly one ($\alpha \approx 1$), which indicates that the fractional element is essentially a damper and the model is nearly the traditional Kelvin-Voigt model. In this case, the storage is virtually constant, and the loss is virtually linear. Defining the dynamic property damping as the loss modulus divided by frequency:

$$B(\omega) = \frac{K''(\omega)}{\omega}, \tag{201}$$
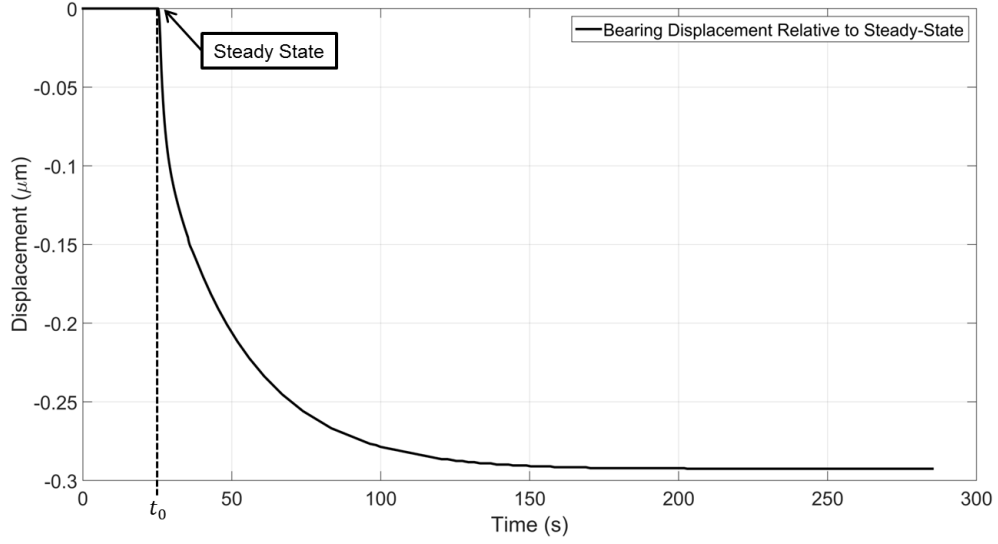
Figure 60: Change in bearing height due to a 2% (12 N/m) load perturbation

the damping in the rigid/impermeable case is practically linear. This translates to constant stiffness and damping, exactly like a spring and dashpot in parallel. These results are consistent with a viscous response.

7.4.2 Rigid and Permeable Case

The effect of permeability on storage and loss is studied in the rigid case (no material deformation). The permeability is varied from the rigid case to a value of $k = 10^{-13}$. Increasing the permeability beyond this point is not suitable for the example parameters given (the bearing cannot support the load requirements). The compliance results are shown in Fig. 62 for various permeabilities. The results given in Table 15 show that the K term decreases with an increase in permeability, while ν increases with permeability. The trade-off in storage and loss follows trends and the discussion presented in Chapter 5 on the "effective film thickness." However, the character of the storage and loss is relatively unchanged by the permeability. This is indicated by the fractional derivative value not changing significantly from the rigid to the most permeable cases ($\alpha \approx 1$). Therefore, the storage properties of the system stay nearly
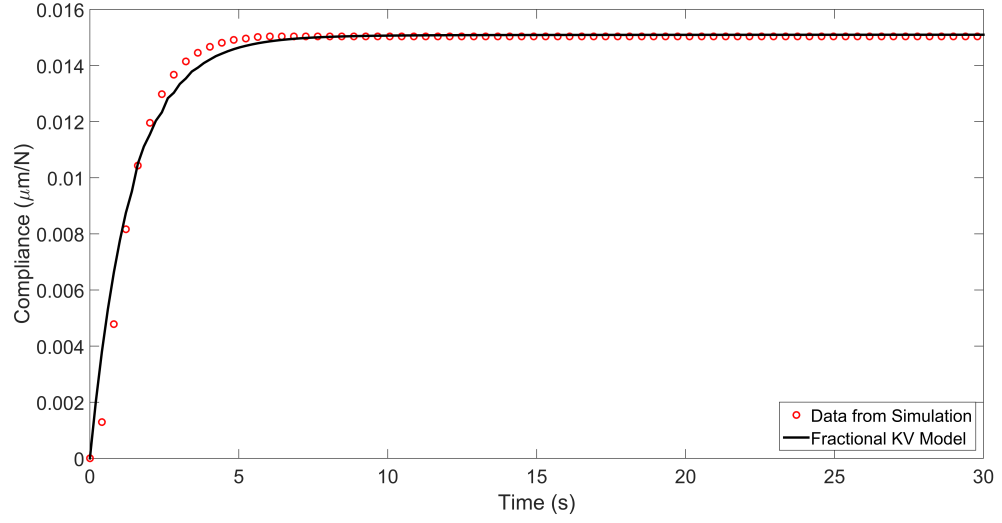
(a) Compliance in the rigid/non-porous case, with fit given in Table 15
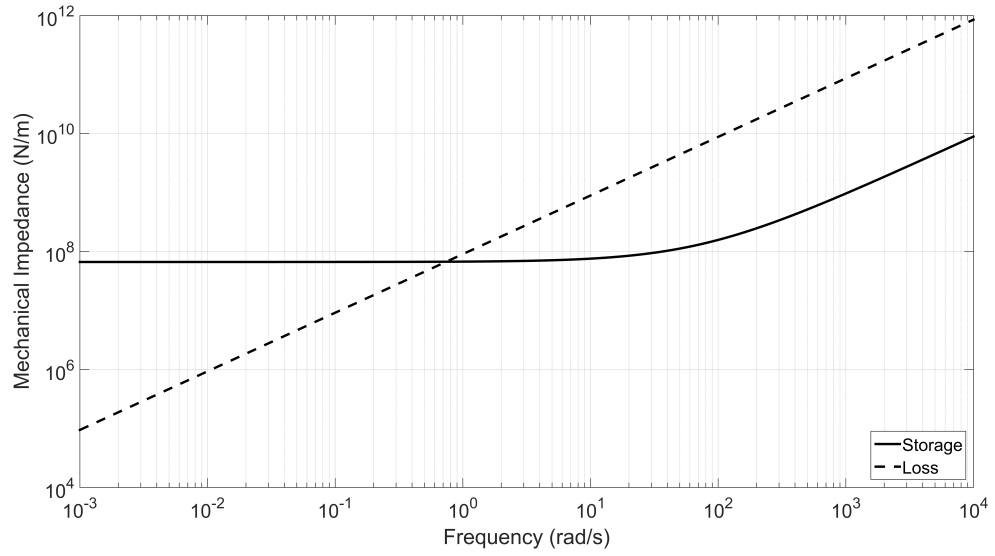
(b) Storage and loss in the rigid/non-porous case

Figure 61: Compliance and storage and loss in the rigid/non-porous case
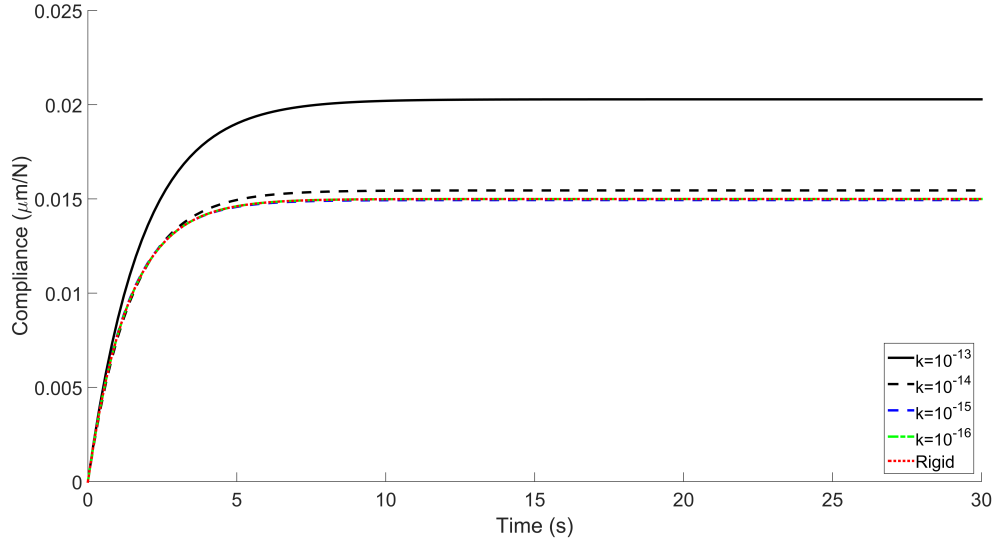
Figure 62: Compliance in the rigid/porous cases

constant with frequency, and the loss properties are practically linear with frequency, as shown in Fig. 61b.

In the permeable region where triboelement operation is possible ($k \lesssim 10^{-13} \ (m^2)$), the effect of permeability alone is not significant enough to change the storage and loss character (α remains approximately 1). This is indicated in Table 15 and Figs. 61b and 62, where the response is shown to effectively be a spring and damper in parallel. However, the mechanism of permeability is still influential in the bearing's performance, as the storage decreases with an increase in permeability, and the loss increases with increasing permeability. Discussed herein, the combination of permeability and flexibility gives rich frequency dependent behavior. This is because permeability changes the action of deformation in the porous pad. In likelihood, the permeability does change the storage and loss characteristics significantly, but this occurs outside of the operational region for the considered case.

Table 15: Storage and loss fit to simulation data (rigid configuration)

k (m^2)	K (N/m)	ν (s)	α	h_o (μm)
Non-porous	6.64×10^7	1.363	0.991	18.1
10^{-16}	6.67×10^7	1.363	0.993	18.0
10^{-15}	6.67×10^7	1.363	0.993	17.8
10^{-14}	6.49×10^7	1.365	0.993	16.9
10^{-13}	4.93×10^7	1.888	0.988	12.1

7.4.3 Flexible Cases

The boundary conditions of Case I are used to compare the rigid/non-porous case to the flexible cases. This fixes the PVE pad at the lateral edges, but still allows for deformation in the PVE body due to fluid exodus. The Case I boundary conditions provide the best platform for comparison purposes with the rigid cases. The flexible/porous case has two additional material mechanisms compared to the rigid case- permeability and viscoelasticity. A representative set of viscoelastic parameters is used in ABAQUS (Table 16).

Figure 65a shows the compliance of the flexible/non-porous and rigid/non-porous cases. Two important differences exist between the flexible/non-porous and rigid/non-porous cases: 1) the flexible/non-porous case has significantly more compliance than the rigid/non-porous case, and 2) the flexible/non-porous case cannot be fit with a single fractional order model. Rather, a two element chain of fractional Kelvin-Voigt elements is required (Fig. 63). The implications of this are significant because it shows the impact of the viscoelastic/permeable component.

Figure 65b shows the dynamic storage and loss of the rigid/non-porous and
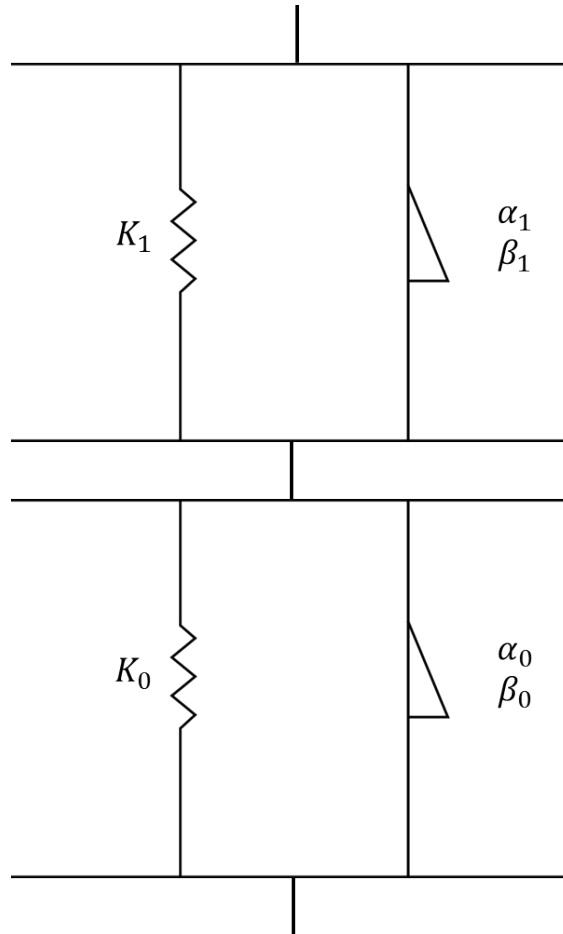
Figure 63: Two element chain of fractional Kelvin-Voigt elements

Table 16: ABAQUS inputs for viscoelastic component

Parameter	Symbol	Value (units)
Poisson's ratio (instantaneous)	ν	0.3
Elastic modulus (instantaneous)	E	15.0 (MPa)
PVE pad length	L	25.00 (mm)
PVE pad height	H	6.25 (mm)
Perturbation	ΔW	$(0.02)W$
Prony constant (bulk)	k_1	0.152
	k_2	0.135
	k_3	0.310
	k_4	0.217
Prony constant (shear)	g_1	0.152
	g_2	0.135
	g_3	0.310
	g_4	0.217
Prony time constant	τ_1	7.682 (s)
	τ_2	0.238 (s)
	τ_3	2.229 (s)
	τ_4	5.617 (s)

flexible/non-porous cases. The flexible/non-porous case shows that the viscoelastic action manifests in the storage and loss results. The flexible/non-porous case has a higher loss across the frequency spectrum versus the rigid/non-porous case. At low frequencies, the flexible/non-porous case has lower storage than its rigid/non-porous counterpart. However, as the frequency increases, the storage in the flexible/non-porous case increases beyond the rigid/non-porous case. This is due to the frequency dependent portions of the fractional spring-pots that are associated with the storage modulus. The viscoelastic case has a larger component attributed to the frequency-dependent storage modulus (i.e. $\alpha_n < 1$) than the rigid case. Physically, this increase in storage is attributed to the reduced film thickness in the flexible cases (Fig. 64a). Tables 15 and 17 indicate that the flexible cases generally have smaller film thicknesses than their rigid counterparts. The smaller film thickness generates higher storage values, but viscoelasticity also influences the storage properties. Therefore, the total response is a combination of these effects. Viscoelasticity also changes the

character of the response. This differentiates the rigid and flexible cases, and means that there is a region of the frequency response that may be tunable by controlling the viscoelastic and/or permeable action. The impact of permeability when the viscoelastic mechanism is included is explored next.

An example of the flexible and porous case is shown in Fig. 66. Here, the viscoelastic and porous actions occur simultaneously. The fit parameters in Table 17 indicate what is happening in Fig. 66. In the flexible/porous cases, the fractional derivatives, α_n, deviate dramatically from the rigid/non-porous and flexible/non-porous cases, where $\alpha \approx 1$. As α approaches $1/2$, the viscoelastic response is clearly seen. Figure 66 shows this clear viscoelastic response at low frequencies, followed by a viscously dominated response at higher frequencies. Combining permeability and viscoelasticity changes the character of the response appreciably from the rigid/non-porous case and flexible/non-porous cases. The combined permeability and viscoelasticity play a governing role in the storage and loss characteristics. Essentially, the time-scale of the path that the triboelement takes after a perturbation is changed, and the resulting storage and loss character is altered. Without the viscoelastic action, the permeability has a relatively small effect on the triboelement's dynamic performance; however, with the coupled viscoelasticity, the dynamic performance is significantly altered. This is apparent in the fit parameters given in Table 17, where the K, ν, and α values are tangibly different for the flexible/porous and flexible/non-porous cases.

7.5   Tunable Dynamic Performance

It has been shown that the dynamic performance of a triboelement is changed with the introduction of a porous substrate. From a design standpoint, a number of degrees of freedom exist in the triboelement characteristics. These include geometric changes in the bearing (inclination, etc.) and in the porous pad (pad length, depth, etc.), as well as material changes (permeability, viscoelastic properties, etc.).

141
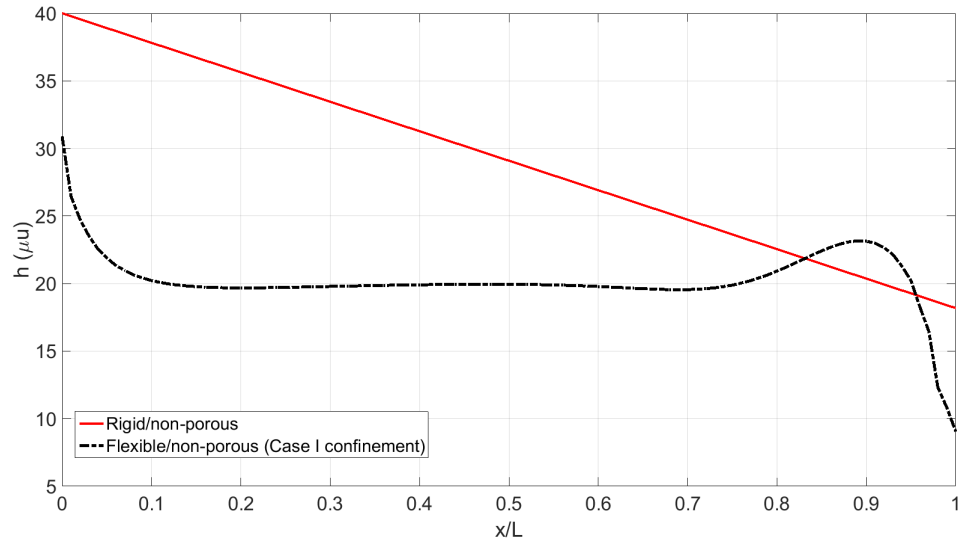
(a) Film thicknesses of the rigid/non-porous and flexible/non-porous cases
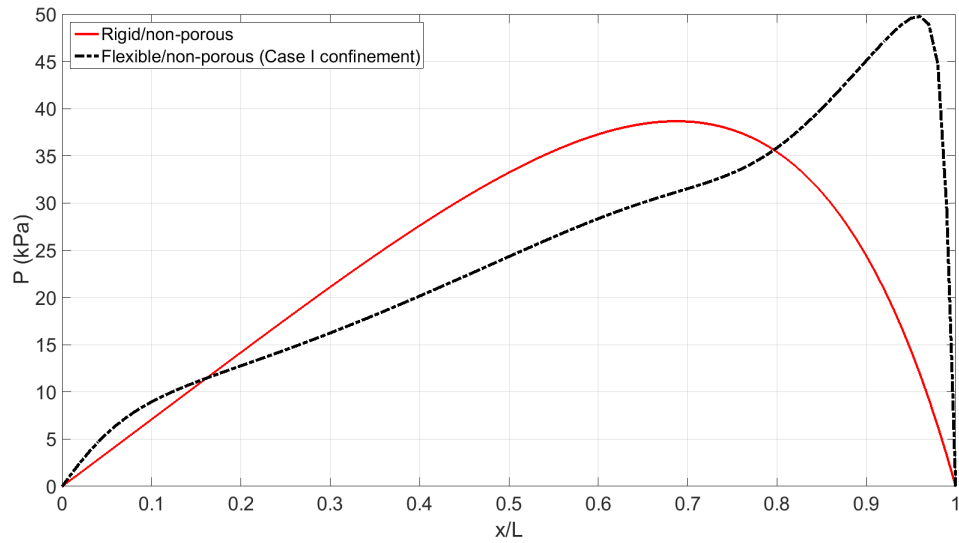
(b) Pressure profiles of the rigid/non-porous and flexible/non-porous cases

Figure 64: Final steady-state results of rigid/non-porous and flexible/non-porous solutions
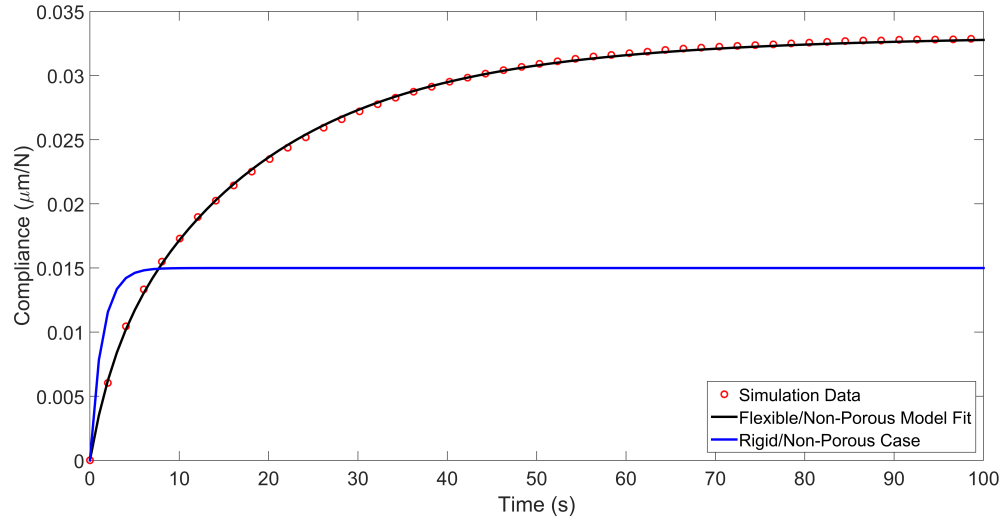
(a) Compliance in the rigid/non-porous case vs. the flexible/non-porous case
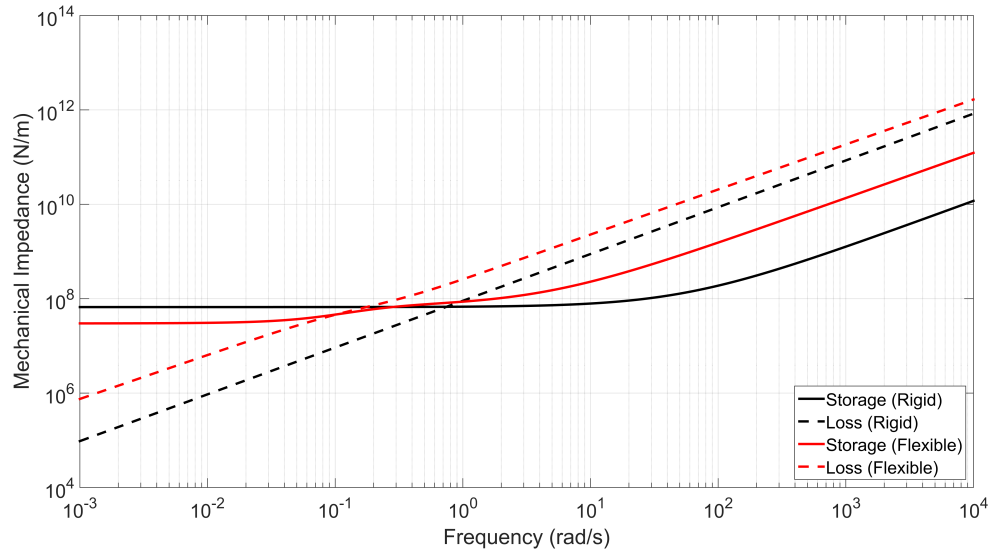
(b) Storage and loss in the rigid/non-porous case vs. the flexible/non-porous case

Figure 65: Compliance and storage and loss in the rigid/non-porous case
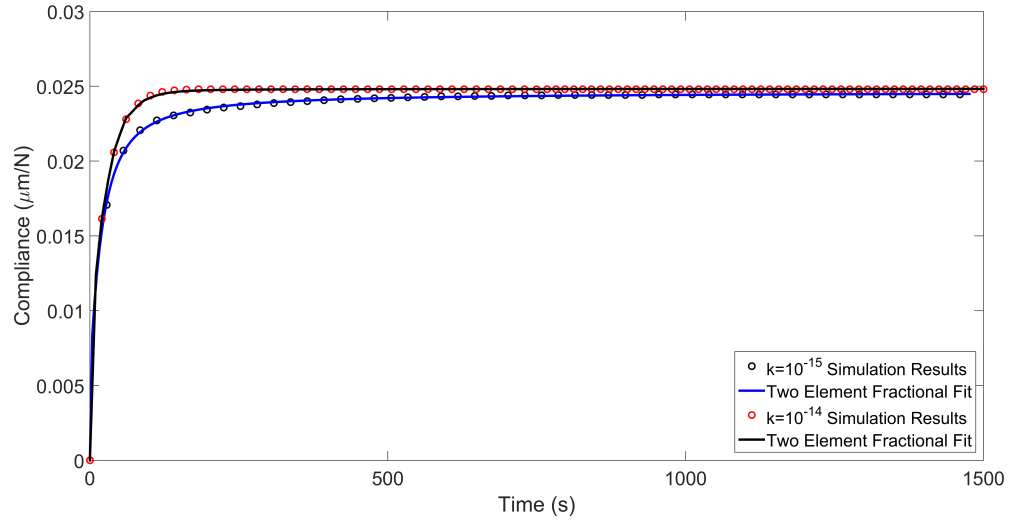
(a) Compliance in the flexible/porous cases
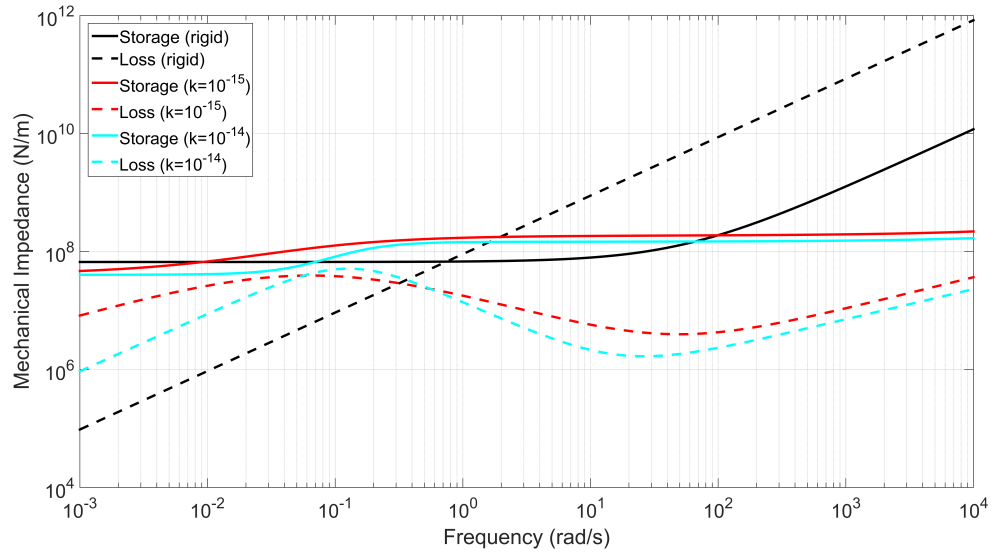
(b) Storage and loss in the flexible/porous cases

Figure 66: Compliance and storage and loss in the flexible/porous cases

Table 17: Storage and loss fit to simulation data

k (m^2)	K (N/m)	ν (s)	α	h_o (μm)
Flexible/non-porous	1.59×10^8	2.568	0.968	9.06
	3.68×10^8	23.764	0.934	
10^{-15}	1.86×10^8	8.32×10^{-6}	0.5367	6.01
	5.19×10^7	176.93	0.6278	
10^{-14}	1.46×10^8	5.17×10^{-6}	0.5125	5.08
	5.56×10^7	29.60	0.9779	

The HDL/PVE system has two important mechanisms that influence the storage and loss: the permeability and the viscoelastic action. In particular, as the permeability drops in the coupled HDL/PVE system, the viscoelastic flexibility in the porous pad still acts to change the dynamic properties of the triboelement. Having two mechanisms that influence the dynamic storage and loss gives a great deal of flexibility in triboelement design.

The takeaway of this analysis is that there exists a trade-off between the storage and loss properties of a flexible/porous bearing. The porous cases presented are able to sustain loads comparable to the rigid case. Therefore, the penalty of using a flexible/porous bearing is likely not prohibitive. Loss is increased in the flexible/porous triboelements. In certain applications, this is a preferable operating condition. Some additional benefits are hypothesized too. These include: lubricant availability in the porous pad if a loss of lubricant occurs, increased ability to mitigate shock events, and potential operation in a full film regime for longer compared to the rigid case.

7.6   Region of Applicability

The storage and loss results given herein are determined from a 2% load perturbation. In the small region around the operating load, the results are assumed linear with the load perturbation. Therefore, the perturbation magnitude does not influence the storage and loss results. In limited testing, this assumption has proven to be correct, and the load perturbation has been tested up to approximately 5% before the simulation fails to converge.

CHAPTER VIII

CLOSURE

The stated goals of this work were to develop a fractional calculus representation of poroviscoelasticity and simulate it in the time domain. This was accomplished with the CERF model of viscoelasticity, and a number of numerical routines were provided for simulation purposes. Ultimately, the poroviscoelastic formulation was desired for application in tribological applications. A test case was proposed to determine the feasibility of poroviscoelastic materials as bearing substrates in HDL problems. Finally, analysis tools were developed to quantify the impact of this proposed configuration.

Chapters 3-4 provide the basis for a fractional calculus PVE material. Fractional calculus is desirable in viscoelasticity because of its modeling simplicity (number of elements required). The trade-off is that the computational burden is large with fractional calculus, as the fractional elements are strongly historic. Efficient simulation algorithms are lacking. In this work, a method of bypassing the strong historic nature of fractional elements is utilized. The results are promising for the applications tested. An efficient algorithm allows for the analysis of PVE materials in novel applications.

The Reynolds equation is modified from the rigid case to describe the fluid mechanics of a thin film interacting with a porous substrate. Permeability is shown to have a strong coupling effect on the porous Reynolds equation. In order to simulate the transient behavior of the PVE/HDL system, continuously updating numerical schemes are required. This is discussed in Chapters 5 and 6.

The results presented in Chapter 7 are promising in a number of ways. First, the simulations prove that a coupled PVE/HDL problem is feasible in a tribological sense. Specifically, a porous/flexible pad can sustain a load that is comparable to

its rigid counterpart (see Figs. 55a-55b). However, the load support of the triboelement is strongly influenced by the permeability of the porous pad [63, 64]. Ideally, a trade-off exists between permeability and the dynamic properties of interest. In the rigid/porous cases, Fig. 62 indicates that the compliance changes with respect to permeability. This has the effect of changing the storage and loss values for the triboelement. However, the character of the storage and loss (i.e. the frequency dependent shape) is relatively unchanged by the permeability. This is noted by the fit value α remaining nearly 1, meaning that the fractional spring-pot is a simple viscous damper. This indicates that permeability alone will not give the user a great deal of control over the dynamic properties of the triboelement. A flexible interface is considered for this purpose.

Figure 65 compares the compliance of a rigid/non-porous and flexible/non-porous design. The viscoelastic action changes the compliance relative to the viscous action of the rigid case. In the flexible case, there exists a coupled response that is partially viscous (from the fluid) and partially viscoelastic (from the pad). A second modeling element (fractional Kelvin-Voigt) is required to adequately capture this response. The flexible case displays additional loss in the frequency domain compared to the rigid/non-porous case. This is due to the secondary dissipation mechanism of the porous pad. However, the character of the loss modulus is essentially unchanged, while the storage modulus picks up a frequency dependent component from the complex stiffness modulus. The real component of the fractional spring-pot element contributes to the storage modulus and is multiplied by ω, which explains its trend as ω grows.

When the flexible and permeable cases are combined, the dynamic properties take a new shape relative to the previously discussed cases. Figure 66b shows the effect of the coupled dissipation mechanisms, particularly when those mechanisms have different time-scales. Here, there appears to be an element of user control,

or tunability, in the dynamic properties. This can be seen between the permeability cases k^{-14} and k^{-15}. The application of the loss modulus, which is related to damping, could be tuned to mitigate vibrations in a particular band of frequencies. This is one goal of the current study, and the results indicate that there is promise in the unique coupling of PVE/HDL.

The "big-picture" view of this work is that it proves the feasibility of a coupled flexible/porous material with a hydrodynamic fluid load. Not only can bearing designs of this nature support tribological loads, the material properties can be manipulated to change the dynamic storage and loss characteristics. The importance of this should not be understated. The current work provides both insight into how certain natural systems work, and also a toolbox for exploring tribological applications.

The genesis of coupled PVE/HDL comes from biomimetics, where biological solutions exist for many tribological problems. With biological materials, the engineer cannot control the material properties; however, the physics can be described. The proposed PVE/HDL model describes the physics of a flexible/porous material interacting with a fluid film load. Potentially, the model has use in the study of biological mechanisms, as well as biomimetic tribological applications. Articular cartilage is of particular interest in biomimetics because of its adaptability and longevity. Coupling mechanisms like a fluid film and porous pad helps to translate from biomechanical to tribological applications.

New demands in triboelement performance require innovative technology. A coupled HDL/PVE bearing is a feasible configuration for certain applications. These include biomechanics, flexible bearing technology, and sealing elements. In addition, PVE materials have strong dissipation characteristics, making them suitable for shock absorption and damping elements. The results of the coupled HDL/PVE simulation indicate that flexible, porous substrates can promote tunable triboelement

149

performance. While the current work shows improved loss at low frequencies, different material combinations could give more dissipation at other frequency spectrums (e.g. frequencies experienced in an internal combustion engine). This can potentially improve tribological considerations, especially wear and damping. Additional study is required to quantify this performance.

8.1 Future Work

The current work addresses the mathematics of coupling unique mechanisms, and merging solid and fluid mechanics of triboelements. What is accomplished in this work is the foundation for study of these coupled solid/fluid mechanisms. The framework presented herein is portable across many applications, and could be used as a starting point for additional tribological study. This includes flexible/porous journal bearings, squeeze film dampers, seismic and abutment dampers, and many other applications.

Specific recommendations for the future path of this work include: exploring non-uniform permeability patterns in the PVE pad, geometric tailoring of the PVE pad, flexibly mounting the porous pad, and new confining boundary conditions on the PVE pad, among others. Unique geometries or configurations (e.g. porous region followed by an impermeable region) could be employed to create effective converging gaps. Etsion and Michael [64] propose a similar concept for the rigid/porous case, with special consideration for sealing applications.

Although the work herein exclusively deals with incompressible solids and fluids, a similar analysis could be performed with compressible fluids. It is hypothesized that the stiffness and damping characteristics would be drastically changed in the compressible case. Based on Miller and Green's work [70, 101, 102], the compressible component would likely act in series with the porous and/or viscoelastic mechanisms. The correspondence principle could be used to assemble a network of viscoelastic elements, creating rich dynamic characteristics.

Extending the analysis to three dimensions is another goal for future work. The extension will add significant computational time; therefore, optimization techniques, like those discussed in Chapter 6, will almost certainly be needed.

Additional performance metrics are readily obtained from the completed work. These include: determination of fluid shear, friction, and leakage (both in the fluid channel and the porous pad). Other metrics will require additional consideration and experimentation. These include: wear, frictional heating, and longevity studies. Non-dimensional groupings of parameters should also be sought to describe the physics of the studied system. For example, a permeable Sommerfeld-type number might have use in the description of a PVE/HDL system in a journal bearing.

Numerical improvements to the current simulations are also proposed. These include: changing the unit system (bringing deformation and pressure to the same order of magnitude), addressing the sensitivity to initial conditions, developing an adaptive code that terminates upon completion of certain goals, and seeding the steady-state with the elastic solution. The proposed improvements fall under the category of "optimization." In a design situation, a robust (less sensitive) and optimized code will aid the user in expediently obtaining results. These concepts are left for future developments.

APPENDIX A

NUMERICAL SCHEME FOR SOLVING POROUS

REYNOLDS EQUATION

The numerical routine used to solve the porous Reynolds equation is presented herein. Recalling the discretized Reynolds equation:

$$
\left[\frac{\partial}{\partial x} \left(H_1^3 \frac{\partial P}{\partial x} \right) \right]_{i,j} + \left[\frac{\partial}{\partial z} \left(H_1^3 \frac{\partial P}{\partial z} \right) \right]_{i,j} =
$$
$$
12\mu \left\{ \frac{\partial}{\partial x} \left[\frac{-U_1 h \left(\xi_0 + 1 \right)}{2} \right] + U_1 \frac{\partial h}{\partial x} + \left(V + V_0 + V' \right) \right\}_{i,j}.
$$

(202)

The partial derivatives are distributed in Eq. 163, and the product rule is analytically evaluated:

$$
3 \left(H_1^2 \right)_{i,j} \left(\frac{\partial H_1}{\partial x} \right)_{i,j} \left(\frac{\partial P}{\partial x} \right)_{i,j} + \left(H_1^3 \right)_{i,j} \left(\frac{\partial^2 P}{\partial x^2} \right)_{i,j} +
$$
$$
3 \left(H_1^2 \right)_{i,j} \left(\frac{\partial H_1}{\partial z} \right)_{i,j} \left(\frac{\partial P}{\partial z} \right)_{i,j} + \left(H_1^3 \right)_{i,j} \left(\frac{\partial^2 P}{\partial z^2} \right)_{i,j} =
$$
$$
-6\mu \left\{ \frac{\partial U_1}{\partial x} \left[h \left(\xi_0 + 1 \right) \right] + U_1 \left(\frac{\partial h}{\partial x} \right) \left(\xi_0 + 1 \right) + U_1(h) \left(\frac{\partial \xi}{\partial x} \right) \right\}_{i,j} +
$$
$$
\left[(12\mu) U_1 \left(\frac{\partial h}{\partial x} \right) \right]_{i,j} + 12\mu \left(V + V_0 + V' \right)_{i,j}.
$$

(203)

Enforcing a uniform grid in the x and z directions, respectively, allows the central difference method to be utilized. The first and second derivative terms involving

pressure are evaluated:

$$\left(\frac{\partial P}{\partial x}\right)_{i,j} = \frac{P_{i,j+1} - P_{i,j-1}}{2\Delta x_j} + O\left(\Delta x_j^2\right)$$

$$\left(\frac{\partial P}{\partial z}\right)_{i,j} = \frac{P_{i+1,j} - P_{i-1,j}}{2\Delta z_i} + O\left(\Delta z_i^2\right)$$

$$\left(\frac{\partial^2 P}{\partial x^2}\right)_{i,j} = \frac{P_{i,j+1} - 2P_{i,j} + P_{i,j-1}}{\Delta x_j^2} + O\left(\Delta x_j^2\right)$$

$$\left(\frac{\partial^2 P}{\partial z^2}\right)_{i,j} = \frac{P_{i+1,j} - 2P_{i,j} + P_{i-1,j}}{\Delta z_i^2} + O\left(\Delta z_i^2\right),$$

(204)

and the terms involving film thickness (or effective film thickness) are likewise evaluated:

$$\left(\frac{\partial H_1}{\partial x}\right)_{i,j} = \frac{(H_1)_{i,j+1} - (H_1)_{i,j-1}}{2\Delta x_j} + O\left(\Delta x_j^2\right)$$

$$\left(\frac{\partial H_1}{\partial z}\right)_{i,j} = \frac{(H_1)_{i+1,j} - (H_1)_{i-1,j}}{2\Delta z_i} + O\left(\Delta z_i^2\right)$$

$$\left(\frac{\partial h}{\partial x}\right)_{i,j} = \frac{h_{i,j+1} - h_{i,j-1}}{2\Delta x_j}$$

(205)

$$\left(\frac{\partial \xi_0}{\partial x}\right)_{i,j} = -\left(\frac{\partial h}{\partial x}\right)_{i,j}\left(\frac{\xi_0}{h + \sqrt{k}/\alpha_B}\right)_{i,j}.$$

The squeeze terms are calculated from the triboelement-dependent kinematic quantities. Therefore, the rate of change of the flexible interface (V'), the traditional squeeze term (V), and the fluid flow across the porous boundary (V_0) must be tracked at each instance in time.

Groupings of values from the right hand side of Eq. 203 are solved for as well:

$$(R_1)_{i,j} = -6\mu h \frac{\partial U_1}{\partial x}(\xi_0 + 1)$$

$$(R_2)_{i,j} = -6\mu \left\{ U_1 \frac{\partial h}{\partial x}(\xi_0 - 1) + U_1(h) \left(\frac{\partial \xi}{\partial x} \right) \right\}_{i,j} \tag{206}$$

$$(R_3)_{i,j} = 12\mu(V + V_0 + V')_{i,j}$$

The following substitutions are made to simplify the analysis:

$$A_{i,j} = \frac{\left[3\left(H_1^2\right)\left(\frac{\partial H_1}{\partial x}\right)\right]_{i,j}}{2\Delta x}$$

$$B_{i,j} = \frac{\left(H_1^3\right)_{i,j}}{\Delta x^2}$$

$$\tag{207}$$

$$C_{i,j} = \frac{\left[3\left(H_1^2\right)\left(\frac{\partial H_1}{\partial z}\right)\right]_{i,j}}{2\Delta z}$$

$$D_{i,j} = \frac{\left(H_1^3\right)_{i,j}}{2\Delta z^2}.$$

The discrete porous Reynolds equation then takes the following form:

$$A_{i,j}\left(P_{i,j+1} - P_{i,j-1}\right) + B_{i,j}\left(P_{i,j+1} - 2P_{i,j} + P_{i,j-1}\right) +$$

$$C_{i,j}\left(P_{i+1,j} - P_{i-1,j}\right) + D_{i,j}\left(P_{i+1,j} - 2P_{i,j} + P_{i-1,j}\right) = \tag{208}$$

$$(R_1)_{i,j} + (R_2)_{i,j} + (R_3)_{i,j}.$$

154

One more set of constants leaves a simple expression for the pressure at location (i, j):

$$(a_0)_{i,j} = -\frac{1}{2}\left[\frac{R_1 + R_2 + R_3}{B + D}\right]_{i,j}$$

$$(a_1)_{i,j} = \frac{1}{2}\left(\frac{A + B}{B + D}\right)_{i,j}$$

$$(a_2)_{i,j} = \frac{1}{2}\left(\frac{B - A}{B + D}\right)_{i,j} \tag{209}$$

$$(a_3)_{i,j} = \frac{1}{2}\left(\frac{C + D}{B + D}\right)_{i,j}$$

$$(a_4)_{i,j} = \frac{1}{2}\left(\frac{D - C}{B + D}\right)_{i,j},$$

$$P_{i,j} = (a_1 P_{i,j+1} + a_2 P_{i,j-1} + a_3 P_{i+1,j} + a_4 P_{i-1,j} + a_0). \tag{210}$$

APPENDIX B

EXAMPLE CODE SEGMENTS

Skeleton codes for Methods I and II are presented here to show the critical coding aspects that must be employed to interface with ABAQUS.

B.1   Python Code Listing- Method I

```
# Import ABAQUS Packages
from part import *
from material import *
from section import *
from assembly import *
from step import *
from interaction import *
from load import *
from mesh import *
from optimization import *
from job import *
from sketch import *
from visualization import *
from connectorBehavior import *
import os
import visualization

# Import ''numpy'' to solve the Reynolds Equation
import numpy
import numpy.matlib
from fractions import Fraction

# Create function to solve porous Reynolds equation

def P_finder(x,z,hi,ho,U,mu,k,alpha):

### Solve Reynolds equation within function

return (W,P)
```

```
#############
# Define constants

hi, ho, W, etc.


session.journalOptions.setValues(replayGeometry=COORDINATE,
 recoverGeometry=COORDINATE)

# Create the Model
mdb.models.changeKey(fromName='Model-1', toName='Model')
mdb.models['Model'].ConstrainedSketch(name='__profile__', sheetSize=1.0)
mdb.models['Model'].sketches['__profile__'].rectangle(point1=(x1, y1),
    point2=(x2, y2))
mdb.models['Model'].ConstrainedSketch(name='Rectangle Sketch',
    objectToCopy=mdb.models['Model'].sketches['__profile__'])
mdb.models['Model'].Part(dimensionality=TWO_D_PLANAR, name=
    'Example Part', type=DEFORMABLE_BODY)
mdb.models['Model'].parts['Example Part'].BaseShell(sketch=
    mdb.models['Model'].sketches['__profile__'])
del mdb.models['Model'].sketches['__profile__']


# Assign the Material
mdb.models['Model'].Material(name='Material Model')

mdb.models['Model'].materials['Material Model'].
Elastic(moduli=INSTANTANEOUS, table=((E0, nu), ))
mdb.models['Model'].materials['Material Model'].
Viscoelastic(domain=TIME, time=PRONY, table=((k1, g1, tau1), ))
mdb.models['Model'].materials['Material Model'].
Permeability(inertialDragCoefficient=0.142887,
specificWeight=, table=((k, void ratio), ))

# Create a Section
mdb.models['Model'].HomogeneousSolidSection
(material='Material Model', name='Section', thickness=1.0,)

# Create a part instance
mdb.models['Model'].rootAssembly.Instance
(dependent=ON, name= 'Instance', part=mdb.models
['Model'].parts['Example Part'])

# Assign Element Type
mdb.models['Model'].parts['Example Part'].
```

```
setElementType(elemTypes=(ElemType(elemCode=
element type, elemLibrary=STANDARD), ElemType
(elemCode=element type,elemLibrary=STANDARD)),
 regions=(mdb.models['Model'].parts['Example Part'].faces.findAt(((
    x, y, z), )), ))

# Mesh
mdb.models['Model'].parts['Example Part'].seedPart(deviationFactor=
    value, minSizeFactor=value, size=value)

mdb.models['Model'].parts['Example Part'].generateMesh()

p = mdb.models['Model'].parts['Example Part']
s = p.edges
side1Edges = s.findAt(((x, y, z), ))
p.Surface(side1Edges=side1Edges, name='Pressure Surface')


# Assign Sets
p = mdb.models['Model'].parts['Example Part']
n = p.nodes
nodes =
p.Set(nodes=nodes, name='TOPNODES')

p = mdb.models['Model'].parts['Example Part']
n = p.nodes
nodes =
p.Set(nodes=nodes, name='BOTTOMNODES')

mdb.models['Model'].parts['Example Part'].Set(name='ALLNODES', nodes=
    mdb.models['Model'].parts['Example Part'].nodes[0:10000000])

p = mdb.models['Model'].parts['Example Part']
n = p.nodes
nodes =
p.Set(nodes=nodes, name='LEFTNODES')

p = mdb.models['Model'].parts['Example Part']
n = p.nodes
nodes =
p.Set(nodes=nodes, name='RIGHTNODES')

p = mdb.models['Model'].parts['Example Part']
f = p.faces
faces = f.findAt(((x, y, z), ))
```

```
region =  p.Set(faces=faces, name='Face Set')
p.SectionAssignment(region=region, sectionName='Section', offset=0.0,
    offsetType=MIDDLE_SURFACE, offsetField='',
    thicknessAssignment=FROM_SECTION)



# Assign Steps

mdb.models['Model'].GeostaticStep(name='Pore Loading',
previous='Initial',timeIncrementationMethod=AUTOMATIC,
minInc=, maxInc=, utol=utol, description=
'Initialize Pore Pressure', nlgeom=ON)

mdb.models['Model'].SoilsStep(cetol=None, description='Iteration',
    end=None, initialInc=, maxInc=, maxNumInc=, minInc=, name=
    'Iteration_0', previous='Pore Loading', timePeriod=t, utol=utol)

mdb.models['Model'].steps['Iteration_0'].Restart
(frequency=1, overlay=ON)

# Initial Void Ratio
mdb.models['Model'].VoidsRatio(distributionType=UNIFORM, name=
    'Initial Void Ratio', region=
    mdb.models['Model'].rootAssembly.instances['Instance'].
    sets['ALLNODES'], variation=CONSTANT_RATIO, voidsRatio1=)

a = mdb.models['Model'].rootAssembly
region = a.instances['Instance'].sets['BOTTOMNODES']
mdb.models['Model'].DisplacementBC(name='Fixed Bottom',
    createStepName='Pore Loading', region=region, u1=0.0, u2=0.0,
     ur3=UNSET, amplitude=UNSET, fixed=OFF,
     distributionType=UNIFORM, fieldName='',localCsys=None)

# Left and Right Edge BC
mdb.models['Model'].PorePressureBC(amplitude=UNSET,
 createStepName='Pore Loading', distributionType=UNIFORM,
 fieldName='', fixed=OFF, magnitude=0.0, name=
 'Zero Pore Pressure Right', region=mdb.models['Model'].
 rootAssembly.instances['Instance'].sets['RIGHTNODES'])

mdb.models['Model'].PorePressureBC(amplitude=UNSET,
 createStepName='Pore Loading', distributionType=UNIFORM,
  fieldName='', fixed=OFF, magnitude=0.0, name=
  'Zero Pore Pressure Left', region=mdb.models['Model'].
  rootAssembly.instances['Instance'].sets['LEFTNODES'])
```

```
# Apply Loads

a = mdb.models['Model'].rootAssembly
region = a.instances['Instance'].sets['TOPNODES']
mdb.models['Model'].PorePressureBC(name='Pore_Pressure_Load',
    createStepName='Pore Loading', region=region, fixed=OFF,
    distributionType=USER_DEFINED, fieldName='', magnitude=1.0,
    amplitude=UNSET)

# Repeat for solid load (sigma)

mdb.models['Model'].fieldOutputRequests['F-Output-1'].setValues(
    variables=('S', 'E', 'U', 'POR', 'PFL','RVF','SAT'))

# History Output
mdb.models['Model'].HistoryOutputRequest(createStepName=
    'Iteration_0', name='H-Output-2', rebar=EXCLUDE, region=
    mdb.models['Model'].rootAssembly.allInstances['Instance'].
    sets['TOPNODES']
    , sectionPoints=DEFAULT, variables=('U1', 'U2'))


# Create and Execute Job
jobName = 'Soil_Example_0'
myJob = mdb.Job(name=jobName, model='Model',
userSubroutine='Path\User_subroutine.for',
description='Model Example Run')

myJob.submit()
myJob.waitForCompletion()


myOdb = visualization.openOdb(path=jobName + '.odb')
session.viewports['Viewport: 1'].
setValues(displayedObject=myOdb)
session.viewports['Viewport: 1'].
odbDisplay.display.setValues(plotState=CONTOURS_ON_DEF)
session.viewports['Viewport: 1'].
odbDisplay.commonOptions.setValues(renderStyle=FILLED)

#Create Path for Top edge and create XYData of that path
topPath = session.Path(name='Top Edge', type=EDGE_LIST, expression=
```

```
u=(('U',NODAL,((COMPONENT, 'U2' ),)),)
session.XYDataFromPath(path=topPath,includeIntersections=False,
shape=DEFORMED,labelType=TRUE_DISTANCE,
name='Deformation',variable=u)

# Strip necessary data from the .odb file (e.g. deformation,
  pressure gradient, etc.)
#Write XY Report to file (get deformation)
xyObjects = session.xyDataObjects['Deformation']
session.writeXYReport(fileName='ScriptXYReport.txt',
xyData=xyObjects,appendMode=OFF)
xyData = numpy.genfromtxt('Path\file.txt',
dtype=float, skip_header=2, autostrip=True)
arr1d = numpy.array(xyData)
reversed_xyData = numpy.fliplr([arr1d])[0]
z1 = -reversed_xyData[:,1]

f1 = open("z1.txt", "a")
z1text = str(z1)
f1.write(z1text)
f1.close()

#########
count = 0
it_count = 0
iteration = 'Iteration_0'
jobName = 'Example_0'

while count < :
it_p1 = str(it_count)
it_p2 = str(it_count+1)

jcount = str(count)
jcount_1 = str(count+1)

iteration = iteration.replace(it_p1,it_p2)
iteration_m = iteration.replace(it_p2,it_p1)

jobName = jobName.replace(jcount,jcount_1)
jobName_m = jobName.replace(jcount_1,jcount)


mdb.models['Model'].setValues(restartJob=jobName_m,
restartStep=iteration_m)
```

```
mdb.models['Model'].SoilsStep(cetol=None, description='Iteration',
end=None, initialInc=, maxInc=, maxNumInc=, minInc=, name=
iteration, previous=iteration_m, timePeriod=, utol=, amplitude=RAMP/INST)
mdb.models['Model'].steps[iteration].Restart(frequency=1, overlay=ON)

#  Call Reynolds equation and process the data as needed

# Create and Execute New Job
myJob = mdb.Job(name=jobName, model='Model', type=RESTART,
userSubroutine='Path\fortran.for',
description='Model Example Run')

myJob.submit()
myJob.waitForCompletion()
count += 1
it_count += 1
# Repeat stripping of data from .odb file (deformation, pore pressure,
 pressure gradients, etc.)

myOdb.close()


import os
os.system('abaqus restartjoin originalodb=Example_0.odb
restartodb=Example_1.odb history')
# Repeat as needed to combine all jobs
```

B.2   Fortran Subroutines- Method II

```
      SUBROUTINE URDFIL(LSTOP,LOVRWRT,KSTEP,KINC,DTIME,TIME)
C
      INCLUDE 'ABA_PARAM.INC'
C
      INTEGER N, K1, K2, K3, M
      PARAMETER(M=101)
      DIMENSION
      EQUIVALENCE (ARRAY(1),JRRAY(1,1))
      REAL*8
C
C    Allocate variable space
C
      COMMON B, C
C
C    Assign the original height of the porous pad for reference
```

```fortran
      Y_orig = height of PVE pad
C     Assign the Nodes to the Node Sets (TN- Top Nodes,
C     STN- Sub Top Nodes)
C
C     Values are compatible with data that is read from .fil file.
C     These values will change if the mesh changes!
C
C     End of node set definition
C
C     This block calls the .fil file to read the x,y coordinates,
C     node numbers, and pore pressure.
C     Data is stored in array A (x-coord,y-cord,node number)
C     and array A2 (node number, pore pressure)
      CALL POSFIL(KSTEP,KINC,ARRAY,JRCD)
      K2 = 1
      K3 = 1
      DO K1=1,M*2
          A(1,K1) = 0
          A(2,K1) = 0
          A(3,K1) = 0
      END DO
      DO K1=1,999999
          CALL DBFILE(0,ARRAY,JRCD)
          IF (JRCD .NE. 0) GO TO 110
          KEY=JRRAY(1,2)
C
C         KEY 107 gives the nodal coordinate data,
C  ARRAY(4) is the x-coord, ARRAY(5) is the
C  y-coord, and JRRAY(1,3) is the node number
C
C         KEY 108 gives the pore pressure data,
C         ARRAY(4) is the pore pressure, and
C         JRRAY(1,3) is the node number
C
          IF (KEY.EQ.107) THEN
A(1,K2) = ARRAY(4)
A(2,K2) = ARRAY(5)
A(3,K2) = JRRAY(1,3)
K2 = K2 + 1
          ELSEIF (KEY.EQ.108) THEN
              A2(1,K3) = JRRAY(1,3)
              A2(2,K3) = ARRAY(4)
              K3 = K3 + 1
          END IF
      END DO
```

```
110   CONTINUE
C     All of the information is stripped from the .fil file
C     at this point
C
C     Now, the arrays A, A2 are separated and
C     combined by Node Set
C     The following loop takes the top node information
C     from array 'A' and places it in array 'B'
C
      K4 = 1
      DO K1=1,M*2
          DO K2=1,M
              IF (A(3,K1).EQ.TN(K2)) THEN
                  B(1,K4) = A(1,K1)
                  B(2,K4) = A(2,K1)
                  B(3,K4) = A(3,K1)
                  K4 = K4 + 1
              END IF
          END DO
      END DO
C
C   The following loop takes the "sub" top node information
C   from array 'A' and places it in array 'C'
C
      K5 = 1
      DO K1=1,M*2
          DO K2=1,M
              IF (A(3,K1).EQ.STN(K2)) THEN
                  C(1,K5) = A(1,K1)
                  C(2,K5) = A(2,K1)
                  C(3,K5) = A(3,K1)
                  K5 = K5 + 1
              END IF
          END DO
      END DO
C
C     The following loop takes the top node information from
C   array 'A2' (pore pressure) and places it in array 'B' (4th row)
C
      DO K1=1,M*2
          DO K2=1,M
              IF (A2(1,K1).EQ.B(3,K2)) THEN
                  B(4,K2) = A2(2,K1)
              END IF
          END DO
```

```
      END DO
C
C     The following loop takes the "sub" top node information from
C     array 'A2' (pore pressure) and places it in array 'C' (4th row)
C
      DO K1=1,M*2
          DO K2=1,M
              IF (A2(1,K1).EQ.C(3,K2)) THEN
                  C(4,K2) = A2(2,K1)
              END IF
          END DO
      END DO
C
C     Reorganize the information in array 'B' from smallest
C     to largest x-coordinate (row1 - x coord, row2 - y coord,
C     row3 - node #, row4 - pore pressure)
C
      DO K3=1,M-1
          DO L = K3+1,M
              IF (B(1,K3).GT.B(1,L)) THEN
                  TEMP1 = B(1,K3)
                  TEMP2 = B(2,K3)
                  TEMP3 = B(3,K3)
                  TEMP4 = B(4,K3)
                  B(1,K3) = B(1,L)
                  B(2,K3) = B(2,L)
                  B(3,K3) = B(3,L)
                  B(4,K3) = B(4,L)
                  B(1,L) = TEMP1
                  B(2,L) = TEMP2
                  B(3,L) = TEMP3
                  B(4,L) = TEMP4
              END IF
          END DO
      END DO
C     Reorganize the information in array 'C' from smallest
C     to largest x-coordinate
C     (row1 - x coord, row2 - y coord,
C     row3 - node #, row4 - pore pressure)
C
      DO K3=1,M-1
          DO L = K3+1,M
              IF (C(1,K3).GT.C(1,L)) THEN
                  TEMP1 = C(1,K3)
                  TEMP2 = C(2,K3)
```

```
                  TEMP3 = C(3,K3)
                  TEMP4 = C(4,K3)
                  C(1,K3) = C(1,L)
                  C(2,K3) = C(2,L)
                  C(3,K3) = C(3,L)
                  C(4,K3) = C(4,L)
                  C(1,L) = TEMP1
                  C(2,L) = TEMP2
                  C(3,L) = TEMP3
                  C(4,L) = TEMP4
              END IF
            END DO
        END DO
C
C     Evaluate Darcy flow into substrate (dp/dy).
C     More exact evaluation would be to interpolate x,y,P,
C     data first to account for lateral movement of the nodes
C
        DO K1=1,M
            dp_dy(K1) = (B(4,K1)-C(4,K1))/(B(2,K1)-C(2,K1))
        END DO
C
C     YOU MUST BE CLOSE TO EQUILIBRIUM TO SOLVE
C     THIS CORRECTLY!!!! B_PRE MUST BE SET
C
        N = 1
        IF (KINC.EQ.N .AND. KSTEP.EQ.2) THEN
            HI = 40D-6
C   Enforces same profile regardless of starting point
            HO = HI - (40D-6 - 40D-6/2.2D0)
            HI_old(1) = HI
            DO K1=1,M
                dh_PVE_dt(K1) = 0D0
            END DO
            H_t1(M+1) = 1D0
            H_t2(M+1) = 0D0
            dh_dt = 1D-10
        ELSE
C
C   Read historic data from previous iteration
C
            OPEN(105,FILE='Path\dh_dt_test.txt')
            READ(105,*) dh_dt
            CLOSE(105)
            OPEN(105,FILE='Path\HI.txt')
```

```
            READ(105,*) HI_old(1)
            CLOSE(105)
            OPEN(105,FILE='Path\H_t1.txt')
            READ(105,*) H_t1
            CLOSE(105)
            OPEN(105,FILE='Path\H_t2.txt')
            READ(105,*) H_t2
            CLOSE(105)
        END IF


        Z(M+1) = TIME(2)
        dt = Z(M+1) - H_t1(M+1)
C
        DO K1=1,M
            Z(K1) = Y_orig-B(2,K1)
            X(K1) = 0.00025D0*(K1-1.0D0)
            P(K1) = 1.0D0
            dh_PVE_dt(K1) = (Z(K1)-H_t2(K1))/(Z(M+1)-H_t2(M+1))
        END DO

C    Assign parameters for the Reynolds Equation
        W_load, U_velo, AMU, AK, ALPHA, HD, W
C
C    This is where the perturbation is introduced (t_0)
C     Depending on the step, a fast ramp may be required
C     for ABAQUS to converge
C
        IF (TIME(2).GT.t_0) THEN
            W = value
        END IF
C
        HI = HI_old(1) + dh_dt*DTIME
        HO = HI-HD
        dh_dt_old = dh_dt
C
        dh_dt_0 = -1D-5
        dh_dt_1 = 1D-5
C
C     The following loop iterates the Reynolds equation
C      to find the rate of change of the film thickness
C      that matches the load.  A bisection method is used
C      to find the appropriate film thickness rate (dh_dt).
        DO K1=1,999999
C          The solution tolerance is governed by the
C    term on the right of the "greater
```

```
C           than" symbol (.GT.). The value is determined
C           relative to the actual load (e.g. stop the loop when
C           W_load is within 0.01\% of W).
C
            IF (ABS(W_load-W) .GT. 0.0001D0*W) THEN
                dh_dt = (dh_dt_1+dh_dt_0)/2.0D0
                CALL REYNOLDS(X,HO,HI,Z,U_velo,AMU,AK,ALPHA,P,
     1          H,W_load,dp_dy,dh_dt,dh_PVE_dt,du_dy)
C    An algorithm must be developed to change the film thickness
C    Can be done instantaneously on h, or smoothly (e.g. on dh_dt)
      END DO
C
      DO K1=1,M
          H_text(K1) = H(K1)
          P_text(K1) = P(K1)
      END DO
      H_text(M+1) = TIME(2)
      P_text(M+1) = TIME(2)
C
C    Output all relevant data to the text files
C    (excluded for brevity)
C
      RETURN
      END
C
      SUBROUTINE REYNOLDS(X,HO,HI,Z,U_velo,AMU,AK,ALPHA,
     1 P,H,W_load,dp_dy,dh_dt,dh_PVE_dt,du_dy)
      INTEGER M
      PARAMETER(M=101)
      REAL*8 Allocate variables
C
C     INITIALIZE ARRAYS
C     DEFINE PARAMETERS AND CREATE
C     DOUBLE PRECISION CONSTANTS
C     DEFINE CONVERGENCE METRICS
C
C  Define big H (effective film thickness)
C  Evaluate derivatives dh_dx, dH1_dx, dU1_dx
C   Create all of the constants for grid point values A,B,
C   stretch term, wedge term, squeeze term.

C  Iterate for nodal pressure until global and local
C   convergence is obtained
C   Evaluate load support (integrate pressure profile)
C
```

```
C   Evaluate performance metrics, side leakage, shear, etc.

      END SUBROUTINE REYNOLDS
C
      SUBROUTINE DISP(U,KSTEP,KINC,TIME,NODE,NOEL,JDOF,COORDS)
C
      INCLUDE 'ABA_PARAM.INC'
C
      INTEGER M
      PARAMETER(M=101)
      DIMENSION U(3),TIME(2),COORDS(3)
      REAL*8 C(4,M), B(4,M), B_0(M), B_pre(4,M)
      COMMON B, C
      INTEGER N KINC
C
C   Initialize values for first iteration (pull values from file,
C   must be close to equilibrium to work).

C   Load the pore pressure nodes with the fluid pressure from
C   the Reynolds equation
C
      DO K1=1,M
          IF (NODE.EQ.B(3,K1)) THEN
              U(1) = B(4,K1)
          END IF
      END DO
C
      END

      SUBROUTINE DLOAD(F,KSTEP,KINC,TIME,NOEL,NPT,LAYER,KSPT,
     1 COORDS,JLTYP,SNAME)
C
C   This subroutine provides the load on the solid grains
C   of the PVE pad
C
      INCLUDE 'ABA_PARAM.INC'
C
      DIMENSION TIME(2), COORDS (3), ELE_SET(50)
      CHARACTER*80 SNAME
C
      INTEGER M N KINC NPT
      PARAMETER(M=101)
      REAL*8 B(4,M)
      COMMON B
C
```

```
C    Put zero load on the two corner nodes (x = 0, x= L)
C
C    Place the solid load on the integration points of interest
C
     END
```

B.3   Input File- Method II

```
*Heading
 Coupled Example Run
** Job name: Example_0 Model name: Substrate Model
** Generated by: Abaqus/CAE 6.14-1
*Preprint, echo=NO, model=NO, history=NO, contact=NO
**
** PARTS
**
*Part, name="Substrate Example Part"
*Node
*Element, type=elements
*Nset, nset="Face Set", generate
*Elset, elset="Face Set", generate
*Nset, nset=TOPNODES
*Nset, nset=BOTTOMNODES
*Nset, nset=ALLNODES, generate
*Nset, nset=LEFTNODES
*Nset, nset=RIGHTNODES
 *Nset, nset=LEFTNODES_CORNER
*Nset, nset=RIGHTNODES_CORNER
 *Nset, nset=STN
*Elset, elset=_Pressure_Surface_S3, internal, generate
*Surface, type=ELEMENT, name=Pressure_Surface
_Pressure_Surface_S3, S3
** Section: Substrate Section
*Solid Section, elset="Face Set", material="Substrate Material Model"
1.,
*End Part
**
**
** ASSEMBLY
**
*Assembly, name=Assembly
**
*Instance, name="Substrate Instance", part="Substrate Example Part"
*Nset, nset=TOPNODES_PP_, internal
```

```
*Nset, nset=LEFTNODES_PP_, internal
*Nset, nset=RIGHTNODES_PP_, internal
 *Nset, nset=LEFTNODES_EXTRA_PP_, internal
*Nset, nset=RIGHTNODES_EXTRA_PP_, internal
*Nset, nset=Sub_Bottom_Nodes
*End Instance
**
*End Assembly
**
** MATERIALS
**
*Material, name="Substrate Material Model"
*Elastic, moduli=INSTANTANEOUS
*Permeability, specific=.
**** ABAQUS uses hydraulic conductivity
**** Make sure to convert
*Viscoelastic, time=PRONY
**
** PREDEFINED FIELDS
**
** Name: Initial Void Ratio   Type: Void ratio
*Initial Conditions, TYPE=RATIO
"Substrate Instance".ALLNODES, value
** ---------------------------------------------
**
** STEP: Pore Loading
**
*Step, name="Pore Loading", nlgeom=YES
Initialize Pore Pressure
*Geostatic, utol=
**
** LOADS
**
** Name: Pressure_Load   Type: Pressure
*Dsload
"Substrate Instance".Pressure_Surface, PNU, 1.
**
** BOUNDARY CONDITIONS
**
** Name: Fixed Left Type: Displacement/Rotation
*Boundary
"Substrate Instance".LEFTNODES_PP_, 1, 1
"Substrate Instance".LEFTNODES_EXTRA_PP_, 2, 2
** Name: Fixed Right Type: Displacement/Rotation
*Boundary
```

```
"Substrate Instance".RIGHTNODES_PP_, 1, 1
"Substrate Instance".RIGHTNODES_EXTRA_PP_, 2, 2
** Name: Fixed Bottom Type: Displacement/Rotation
*Boundary
"Substrate Instance".BOTTOMNODES, 1, 1
"Substrate Instance".BOTTOMNODES, 2, 2
** Name: Pore_Pressure_Load Type: Pore pressure
*Boundary, user
"Substrate Instance".TOPNODES_PP_, 8, 8, 1.
** Name: Zero Pore Pressure Left Type: Pore pressure
*Boundary
"Substrate Instance".LEFTNODES_PP_, 8, 8
** Name: Zero Pore Pressure Right Type: Pore pressure
*Boundary
"Substrate Instance".RIGHTNODES_PP_, 8, 8
**
** OUTPUT REQUESTS
**
*Restart, write, frequency=0
**
** FIELD OUTPUT: F-Output-1
**
*Output, field
*Node Output
POR, RVF, U, V
*Element Output, directions=YES
E, S, SAT
*Contact Output
PFL,
**
** HISTORY OUTPUT: H-Output-1
**
*Output, history, variable=PRESELECT
*End Step
** ----------------------------------------------------------------
**
** STEP: Iteration_0
**
*Step, name=Iteration_0, nlgeom=YES, inc=100000
Iteration
*Soils, consolidation, end=PERIOD, utol=.
*CONTROLS, PARAMETERS=TIME INCREMENTATION
,,,,,,,,100
**
** BOUNDARY CONDITIONS
```

172

```
**
** OUTPUT REQUESTS
**
**
** FIELD OUTPUT: F-Output-1
**
*Output, field
** Critical output required for URDFIL to work
** (have to specify that the FIL file is created)
*Node Output
COORD, POR, RVF, U, V
*Element Output, directions=YES
E, S, SAT
*Contact Output
PFL,
**
** HISTORY OUTPUT: H-Output-2
**
*Output, history
*Node Output, nset="Substrate Instance".TOPNODES
U1, U2, U3, UR, UR1, UR2, UR3, UT,
V1, V2, V3, VR, VR1, VR2, VR3, VT,
WARP
*NODE FILE, FREQUENCY = 1, nset ="Substrate Instance".TOPNODES
U,
V,
COORD,
POR,
*NODE FILE, FREQUENCY = 1, nset ="Substrate Instance".Sub_Bottom_Nodes
U,
V,
COORD,
POR,
**
** HISTORY OUTPUT: H-Output-1
**
*Output, history, variable=PRESELECT
*End Step

**** Add Steps as needed
```

REFERENCES

[1] Smyth, P. A., Green, I., Jackson, R. L., and Hanson, R. R., 2014. "Biomimetic Model of Articular Cartilage Based on In Vitro Experiments". *Journal of Biomimetics, Biomaterials and Biomedical Engineering,* **21**, pp. 75–91.

[2] Smyth, P. A., and Green, I., 2015. "A Fractional Calculus Model of Articular Cartilage based on Experimental Stress-Relaxation". *Mechanics of Time-Dependent Materials.*

[3] Lawrence, R. C., Felson, D. T., Helmick, C. G., Arnold, L. M., Choi, H., Deyo, R. A., Gabriel, S., Hirsch, R., Hochberg, M. C., Hunder, G. G., Jordan, J. M., Katz, J. N., Kremers, H. M., Wolfe, F., and Workgroup, N. A. D., 2008. "Estimates of the prevalence of arthritis and other rheumatic conditions in the United States: Part II". *Arthritis & Rheumatism,* **58**(1), pp. 26–35.

[4] Barbour, K. E., Helmick, C. G., Theis, K. A., Murphy, L. B., Hootman, J. M., Brady, T. J., and Cheng, Y. J., 2013. "Prevalence of Doctor-Diagnosed Arthritis and Arthritis-Attributable Activity Limitation - United States, 2010-2012". *Morbidity and Mortality Weekly Report (CDC),* **62**(44), November, pp. 869–873.

[5] Zhang, R., and Soong, T., 1992. "Seismic Design of Viscoelastic Dampers for Structural Applications". *Journal of Structural Engineering,* **118**(5), pp. 1375–1392.

[6] Wilson, W., van Donkelaar, C. C., van Rietbergen, B., Ito, K., and Huiskes, R., 2004. "Stresses in the local collagen network of articular cartilage: a poroviscoelastic fibril-reinforced finite element study". *Journal of Biomechanics,* **37**(3), pp. 357–366.

[7] Wilson, W., van Donkelaar, C. C., van Rietbergen, B., and Huiskes, R., 2005. "A fibril-reinforced poroviscoelastic swelling model for articular cartilage". *Journal of Biomechanics,* **38**(6), pp. 1195–1204.

[8] Biezma, M. V., and Schanack, F., 2007. "Collapse of steel bridges". *Journal of Performance of Constructed Facilities,* **21**(5), pp. 398–405.

[9] Office, C. B., 2015. Public Spending on Transportation and Water Infrastructure, 1956 to 2014. Tech. rep., U.S. Congress.

[10] Grybos, G. R., 1991. "The dynamics of a viscoelastic rotor in flexible bearings". *Archive of Applied Mechanics,* **61**(1), pp. 479–487.

[11] Friswell, M., 2007. "The Response of Rotating Machines on Viscoelastic Supports". *International Review of Mechanical Engineering,* ***1***(1), pp. 32–40.

[12] Elsharkawy, A. A., and Nassar, M. M., 1996. "Hydrodynamic lubrication of squeeze-film porous bearings". *Acta Mechanica,* ***118***, pp. 121–134.

[13] Varney, P., and Green, I., 2014. "Rotordynamic Analysis Using the Complex Transfer Matrix: An Application to Elastomer Supports Using the Viscoelastic Correspondence Principle". *Journal of Sound and Vibration,* ***333***(23), pp. 6258 – 6272.

[14] Biot, M. A., 1954. "Theory of Stress-Strain Relations in Anisotropic Viscoelasticity and Relaxation Phenomena". *Journal of Applied Physics,* ***25***(11), November, pp. 1385–1391.

[15] Biot, M. A., 1955. "Dynamics Of Viscoelastic Anisotropic Media". In Fourth Midwestern Conference on Solid Mechanics, Purdue University.

[16] Biot, M. A., 1955. "Variational and Lagrangian Methods in Viscoelasticity". In Deformation and Flow of Solids, R. Grammel, ed., Springer-Verlag.

[17] Biot, M. A., 1956. "Theory of Deformation of a Porous Viscoelastic Anisotropic Solid". *Journal of Applied Physics,* ***27***(5), May, pp. 459–467.

[18] Rutqvist, J., Rinaldi, A. P., Cappa, F., and Moridis, G. J., 2013. "Modeling of fault reactivation and induced seismicity during hydraulic fracturing of shale-gas reservoirs". *Journal of Petroleum Science and Engineering,* ***107***(0), pp. 31 – 44.

[19] Kim, J., and Moridis, G. J., 2015. "Numerical analysis of fracture propagation during hydraulic fracturing operations in shale gas systems". *International Journal of Rock Mechanics and Mining Sciences,* ***76***(0), pp. 127 – 137.

[20] Reagan, M. T., Moridis, G. J., Keen, N. D., and Johnson, J. N., 2015. "Numerical simulation of the environmental impact of hydraulic fracturing of tight/shale gas reservoirs on near-surface groundwater: Background, base cases, shallow reservoirs, short-term gas, and water transport". *Water Resources Research,* ***51***, pp. 2543 – 2573.

[21] Detournay, E., and Cheng, A. H.-D., 1993. "Fundamentals of Poroelasticity". In *Comprehensive Rock Engineering: Principles, Practice and Projects, Vol. II, Analysis and Design Method*, C. Fairhurst, ed. Pergamon Press.

[22] Terzaghi, K., 1923. "Die berechnung der durchlassigkeitsziffer des tones aus dem verlauf der hydrodynamischen spannungserscheinungen". *Sitz. Akad. Wissen., Wien Math. Naturwiss. Kl., Abt. IIa,* ***132***, pp. 105–124.

[23] Rendulic, L., 1936. "Porenziffer und Porenwasserdrunk in Tonen". *Der Bauingenieur,* ***17***, pp. 559–564.

[24] Biot, M. A., 1935. "Le probleme de la consolidation des matieres argileuses sous une charge". In Ann. Soc. Sci. Bruxelles, Vol. B55.

[25] Biot, M. A., 1941. "General theory of three-dimensional consolidation". *Journal of Applied Physics,* **12**, pp. 155–164.

[26] Simon, B. R., Wu, J. S., Carlton, M. W., Kazarian, L. E., France, E. P., Evans, J. H., and Zienkiewicz, O. C., 1985. "Poroelastic dynamic structural models of rhesus spinal motion segments". *Spine,* **10**(6), pp. 494–507.

[27] Simon, B. R., 1992. "Multiphase Poroelastic Finite Element Models for Soft Tissue Structures". *ASME Applied Mechanics Reviews,* **45**(6), pp. 191–218.

[28] Cowin, S. C., 1999. "Bone poroelasticity". *Journal of Biomechanics,* **32**(3), pp. 217 – 238.

[29] Bujurke, N., and Kudenatti, R. B., 2006. "An analysis of rough poroelastic bearings with reference to lubrication mechanism of synovial joints". *Applied Mathematics and Computation,* **178**(2), pp. 309 – 320.

[30] Bujurke, N., Kudenatti, R. B., and Awati, V., 2007. "Effect of surface roughness on squeeze film poroelastic bearings with special reference to synovial joints". *Mathematical Biosciences,* **209**(1), pp. 76 – 89.

[31] Wang, H., 2000. *Theory of Linear Poroelasticity with Applications to Geomechanics and Hydrogeology.* Princeton series in geophysics. Princeton University Press.

[32] Roose, T., Netti, P. A., Munn, L. L., Boucher, Y., and Jain, R. K., 2003. "Solid stress generated by spheroid growth estimated using a linear poroelasticity model". *Microvascular Research,* **66**(3), pp. 204 – 212.

[33] Biot, M. A., 1955. "Theory of elasticity and consolidation for a porous anisotropic solid". *Journal of Applied Physics,* **26**, pp. 182–185.

[34] Biot, M. A., 1956. "General solutions of the equations of elasticity and consolidation for a porous material". *Journal of Applied Mechanics,* **78**, pp. 91–96.

[35] Biot, M. A., 1956. "Thermoelasticity and irreversible thermodynamics". *Journal of Applied Physics,* **27**, pp. 240–253.

[36] Biot, M. A., 1956. "Theory of propagation of elastic waves in a fluid-saturated porous solid, part I: low frequency range". *Journal of Acoustic Society of America,* **28**, pp. 168–178.

[37] Biot, M. A., and Willis, D., 1957. "The elastic coefficients of the theory of consolidation". *Journal of Applied Mechanics,* **24**, pp. 594–601.

[38] Biot, M. A., 1962. "Mechanics of deformation and acoustic propagation in porous media". *Journal of Applied Physics,* **33**, pp. 1482–1498.

[39] Biot, M. A., 1964. *Mechanics of Incremental Deformation: Theory of Elasticity and Viscoelasticity of Initially Stressed Solid and Fluids, Including Thermodynamic Foundations and Applications to Finite Strain.* John Wiley & Sons, Inc.

[40] Biot, M. A., 1972. "Theory of Finite Deformations of Porous Solids". *Indiana University Mathematics Journal,* **21**(7), pp. 597–620.

[41] Biot, M. A., 1977. "Variational Lagrangian-thermodynamics Of Nonisothermal Finite Strain Mechanics Of Porous Solids And Thermomolecular Diffusion". *International Journal of Solids and Structures,* **13**, pp. 579–597.

[42] Coussy, O., 2004. *Poromechanics.* Wiley.

[43] Fung, Y., 1993. *Biomechanics: Mechanical Properties of Living Tissues.* Biomechanics. Springer New York.

[44] Mow, V., and Huiskes, R., 2005. *Basic Orthopaedic Biomechanics & Mechanobiology.* Lippincott Williams & Wilkins.

[45] Woo, S. L. Y., Simon, B. R., Kuei, S. C., and Akeson, W. H., 1980. "Quasi-Linear Viscoelastic Properties of Normal Articular Cartilage". *Journal of Biomechanical Engineering,* **102**(2), pp. 85–90.

[46] Vena, P., Gastaldi, D., and Contro, R., 2006. "A Constituent-Based Model for the Nonlinear Viscoelastic Behavior of Ligaments". *Journal of Biomechanical Engineering,* **128**(3), pp. 449–457.

[47] Smyth, P., 2013. "Viscoelastic Behavior of Articular Cartilage In Unconfined Compression". Master's thesis, Georgia Institute of Technology.

[48] Smyth, P. A., Varney, P. A., and Green, I., 2016. "A Fractional Calculus Model of Viscoelastic Stator Supports Coupled With Elastic Rotor-Stator Rub". *Journal of Tribology,* **138**(4).

[49] Caputo, M., and Mainardi, F., 1971. "A new dissipation model based on memory mechanism". *Pure and Applied Geophysics,* **91**(1), pp. 134–147.

[50] Bagley, R. L., and Torvik, P. J., 1983. "A Theoretical Basis for the Application of Fractional Calculus to Viscoelasticity". *Journal of Rheology (1978-present),* **27**(3), pp. 201–210.

[51] Torvik, P. J., and Bagley, R. L., 1984. "On the Appearance of the Fractional Derivative in the Behavior of Real Materials". *Journal of Applied Mechanics,* **51**(2), pp. 294–298.

[52] Koeller, R., 1984. "Applications of fractional calculus to the theory of viscoelasticity". *ASME Journal of Applied Mechanics,* **51**, pp. 299–307.

[53] Bagley, R. L., and Torvik, P. J., 1985. "Fractional calculus in the transient analysis of viscoelastically damped structures". *Aiaa Journal,* **23**(6), pp. 918–925.

[54] Bagley, R. L., and Torvik, P. J., 1986. "On the Fractional Calculus Model of Viscoelastic Behavior". *Journal of Rheology (1978-present),* **30**(1), pp. 133–155.

[55] Bagley, R. L., 1989. "Power law and fractional calculus model of viscoelasticity". *American Institute of Aeronautics and Astronautics,* **27**(10), p. 6.

[56] Podlubny, I., 1998. *Fractional Differential Equations: An Introduction to Fractional Derivatives, Fractional Differential Equations, to Methods of Their Solution and Some of Their Applications.* Mathematics in Science and Engineering. Elsevier Science.

[57] Mainardi, F., and Spada, G., 2011. "Creep, relaxation and viscosity properties for basic fractional models in rheology". *The European Physical Journal Special Topics,* **193**(1), pp. 133–160.

[58] Setton, L. A., Zhu, W., and Mow, V. C., 1993. "The biphasic poroviscoelastic behavior of articular cartilage: Role of the surface zone in governing the compressive behavior". *Journal of Biomechanics,* **26**(45), pp. 581 – 592.

[59] Liu, K., and Ovaert, T. C., 2011. "Poro-viscoelastic constitutive modeling of unconfined creep of hydrogels using finite element analysis with integrated optimization method". *Journal of the Mechanical Behavior of Biomedical Materials,* **4**(3), pp. 440 – 450.

[60] Abousleiman, Y., Cheng, A.-D., Jiang, C., and Roegiers, J.-C., 1996. "Poroviscoelastic analysis of borehole and cylinder problems". *Acta Mechanica,* **119**(1-4), pp. 199–219.

[61] Reynolds, O., 1886. "On the Theory of Lubrication and Its Application to Mr. Beauchamp Tower's Experiments, Including an Experimental Determination of the Viscosity of Olive Oil". *Philosophical Transactions of the Royal Society of London.*

[62] Wu, H., 1970. "Squeeze-Film Behavior for Porous Annular Disks". *Journal of Tribology,* **92**(4), October, pp. 593–596.

[63] Prakash, J., and Vij, S., 1974. "Analysis of Narrow Porous Journal Bearing Using Beavers-Joseph Criterion of Velocity Slip". *Journal of Applied Mechanics,* **41**(2), June, pp. 348–354.

[64] Etsion, I., and Michael, O., 1994. "Enhancing Sealing and Dynamic Performance with Partially Porous Mechanical Face Seals". *Tribology Transactions,* **37**(4), pp. 701–710.

[65] Bujurke, N. M., Bhavi, S. G., and Naduvinamani, N. B., 1990. "The Effect of Couple Stresses in Squeeze Film Poro-elastic Bearings with Special Reference to Synovial Joints". *IMA Journal,* **7**, May, pp. 231–243.

[66] Bujurke, N., Naduvinamani, N., and Basti, D., 2007. "Effect of surface roughness on the squeeze film lubrication between curved annular plates". *Industrial Lubrication and Tribology,* **59**(4), pp. 178–185.

[67] Elsharkawy, A. A., and Guedouar, L. H., 2001. "Hydrodynamic lubrication of porous journal bearings using a modified Brinkman-extended Darcy model". *Tribology International,* **34**(11), pp. 767 – 777.

[68] Gurtin, M. E., and Sternberg, E., 1962. "On the linear theory of viscoelasticity". *Archive for Rational Mechanics and Analysis,* **11**(1), pp. 291–356.

[69] Szumski, R. G., and Green, I., 1991. "Constitutive Laws in Time and Frequency Domains for Linear Viscoelastic Materials". *J. Acoustical Soc. of America,* **90**(40), p. 2292.

[70] Miller, B., and Green, I., 1997. "On the stability of gas lubricated triboelements using the step jump method". *Journal of Tribology-Transactions of the Asme,* **119**(1), pp. 193–199.

[71] Bagley, R. L., and Torvik, P. J., 1979. "A generalized derivative model for an elastomer damper". *Shock and Vibration Inform. Center The Shock and Vibration Bull, Pt. 2 p 135-143(SEE N 80-16211 07-31).*

[72] Rogers, L., 1983. "Operators and Fractional Derivatives for Viscoelastic Constitutive Equations". *Journal of Rheology,* **27**(4), pp. 351–372.

[73] Koeller, R. C., 1986. "Polynomial operators, stieltjes convolution, and fractional calculus in hereditary mechanics". *Acta Mechanica,* **58**(3-4), pp. 251–264.

[74] Schiessel, H., and Blumen, A., 1993. "Hierarchical analogues to fractional relaxation equations". *Journal of Physics A: Mathematical and General,* **26**(19), p. 5057.

[75] Schiessel, H., Metzler, R., Blumen, A., and Nonnenmacher, T. F., 1995. "Generalized viscoelastic models: their fractional equations with solutions". *Journal of Physics A: Mathematical and General,* **28**(23), p. 6567.

[76] Schiessel, H., and Blumen, A., 1995. "Mesoscopic Pictures of the Sol-Gel Transition: Ladder Models and Fractal Networks". *Macromolecules,* **28**(11), pp. 4013–4019.

[77] West, B., Bologna, M., and Grigolini, P., 2003. *Physics of Fractal Operators.* Institute for Nonlinear Science. Springer.

[78] Carpinteri, A., and Mainardi, F., 1997. *Fractals and fractional calculus in continuum mechanics*. Courses and lectures / International Centre for Mechanical Sciences / International Centre for Mechanical Sciences Udine: Courses and lectures. Springer London, Limited.

[79] Magin, R., 2006. *Fractional Calculus in Bioengineering*. Begell House Publishers.

[80] A. Erdelyi, W. Magnus, F. O., and Tricomi, F., eds., 1955. *Higher Transcendental Functions*, Vol. III. McGraw-Hill, New York.

[81] Szumski, R. G., 1993. "A Finite Element Formulation for the Time Domain Vibration Analysis of an Elastic-Viscoelastic Structure". PhD thesis, Georgia Institute of Technology.

[82] Abramowitz, M., and Stegun, I. A., eds., 1972. *Handbook of Mathematical Functions*. Dover Publications.

[83] Helwany, S., 2007. *Applied Soil Mechanics: with ABAQUS Applications*. John Wiley & Sons.

[84] Means, W. D., 1976. *Stress and Strain- Basic Concepts of Continuum Mechanics for Geologists*. Springer.

[85] Mak, A. F., 1986. "The Apparent Viscoelastic Behavior of Articular Cartilage— The Contributions From the Intrinsic Matrix Viscoelasticity and Interstitial Fluid Flows". *Journal of Biomechanical Engineering,* **108**(2), pp. 123–130.

[86] Suh, J. K., and DiSilvestro, M. R., 1999. "Biphasic Poroviscoelastic Behavior of Hydrated Biological Soft Tissue". *Journal of Applied Mechanics,* **66**(2), pp. 528–535.

[87] ABAQUS, 2014. *Abaqus Documentation 6.14*. Dassault Systems.

[88] DiSilvestro, M. R., and Suh, J.-K. F., 2001. "A cross-validation of the biphasic poroviscoelastic model of articular cartilage in unconfined compression, indentation, and confined compression". *Journal of Biomechanics,* **34**(4), pp. 519–525.

[89] DiSilvestro, M. R., Zhu, Q., and Suh, J.-K. F., 2001. "Biphasic Poroviscoelastic Simulation of the Unconfined Compression of Articular Cartilage: II—Effect of Variable Strain Rates". *Journal of Biomechanical Engineering,* **123**(2), pp. 198–200.

[90] Jurvelin, J. S., Buschmann, M. D., and Hunziker, E. B., 1997. "Optical and mechanical determination of Poisson's ratio of adult bovine humeral articular cartilage". *Journal of Biomechanics,* **30**(3), March, pp. 235–241.

[91] Renaudeaux, J. P., 1985. *Biomechanics of Normal and Pathological Human Articulating Joints*, 1 ed. Springer, New York City, NY, ch. Lubrication of Joints, pp. 215–237.

[92] Musto, M., and Alfano, G., 2015. "A fractional rate-dependent cohesive-zone model". *International Journal for Numerical Methods in Engineering,* **103**, pp. 313–341.

[93] Schmidt, A., and Gaul, L., 2002. "Finite element formulation of viscoelastic constitutive equations using fractional time derivatives". *Nonlinear Dynamics,* **29**, pp. 37–55.

[94] Sorvari, J., and Malinen, M., 2007. "Numerical interconversion between linear viscoelastic material functions with regularization". *International Journal of Solids and Structures,* **44**, pp. 1291–1303.

[95] Tschoegl, N. W., 1989. *The Phenomenological Theory of Linear Viscoelastic Behavior.* Springer-Verlag.

[96] Beavers, G., and Joseph, D., 1967. "Boundary conditions at a naturally permeable wall". *Journal of Fluid Mechanics,* **30**, pp. 197–207.

[97] Hamrock, B., Schmid, S., and Jacobson, B., 2004. *Fundamentals of Fluid Film Lubrication.* Mechanical engineering. CRC Press.

[98] Green, I., 2015. ME6243 Lubrication Class Notes.

[99] Pinkus, O., and Sternlicht, B., 1961. *Theory of Hydrodynamic Lubrication.* McGraw-Hill.

[100] Ruggiero, L., Zimmerman, B. K., Park, M., Han, L., Wang, L., Burris, D. L., and Lu, X. L., 2015. "Roles of the Fibrous Superficial Zone in the Mechanical Behavior of TMJ Condylar Cartilage". *Annals of Biomedical Engineering,* **43**(11), pp. 2652–2662.

[101] Miller, B., and Green, I., 1998. "Constitutive Equations and the Correspondence Principle for the Dynamics of Gas Lubricated Triboelements". *Journal of Tribology,* **120**(2), pp. 345–352.

[102] Miller, B., and Green, I., 2001. "Numerical Formulation for the Dynamic Analysis of Spiral-Grooved Gas Face Seals". *Journal of Tribology,* **123**, April, pp. 395–403.